THÈSE

Présentée et soutenue le *19/03/2018* **par :**
Nicola LUMINARI

Modeling and simulation of flows over and through fibrous porous media

JURY

Mme. Azita Ahmadi-Sénichault	TREFLE, Bordeaux	Présidente du Jury
M. Christophe Airiau	IMFT, Toulouse	Directeur de thèse
M. Alessandro Bottaro	UNIGE, Gênes	Directeur de thèse
M. Mouaouia Firdaouss	LIMSI, Orsay	Rapporteur
M. Didier Lasseux	TREFLE, Bordeaux	Rapporteur
M. Michel Quintard	IMFT, Toulouse	Membre du Jury

Abstract

Any natural surface is in essence non-smooth, consisting of more or less regular roughness and/or mobile structures of different scales. From a fluid mechanics point of view, these natural surfaces offer better aerodynamic performances when they cover moving bodies, in terms of drag reduction, lift enhancement or control of boundary layer separation; this has been shown for boundary layer or wake flows around thick bodies. The numerical simulation of microscopic flows around "natural" surfaces is still out of reach today. Therefore, the goal of this thesis is to study the modeling of the apparent flow slip occurring on this kind of surfaces, modeled as a porous medium, applying Whitaker's volume averaging theory. This mathematical model makes it possible to capture details of the microstructure while preserving a satisfactory description of the physical phenomena which occur.

The first chapter of this manuscript provides an overview of previous efforts to model these surfaces, detailing the most important results from the literature. The second chapter presents the mathematical derivation of the volume-averaged Navier-Stokes equations (VANS) in a porous medium. In the third chapter the flow stability at the interface between a free fluid and a porous medium, formed by a series of rigid cylinders, is studied. The presence of this porous layer is treated by including a drag term in the fluid equations. It is shown that the presence of this term reduces the rates of amplification of the Kelvin-Helmholtz instability over the whole range of wavenumbers, thus leading to an increase of the wavelength of the most amplified mode. In this same context, the difference between the isotropic model and a tensorial approach for the drag term has been evaluated, to determine the most consistent approach to study these flow instabilities. This has led to the conclusion that the model that uses the apparent permeability tensor is the most relevant one. In the following chapter, based on this last result, the apparent permeability tensor, based on over one hundred direct numerical simulations carried out over microscopic unit cells, has been identified for a three-dimensional porous medium consisting of rigid cylinders. In these configurations the tensor varies according to four parameters: the Reynolds number, the porosity and the direction of the average pressure gradient, defined by two Euler angles. This parameterization makes it possible to capture local three-dimensional effects. This database has been set up to create, based on a kriging-type approach, a behavioral meta-model for estimating all the components of the apparent permeability tensor.

In the fifth chapter, simulations of the VANS equations are carried out on a macroscopic scale after the implementation of the metamodel, to get reasonable computing times. The validation of the macroscopic approach is performed on a closed cavity flow covered with a porous layer and a comparison with the results of a very accurate DNS, homogenized a posteriori, has shown a very good agreement and has demonstrated the relevance of the approach. The next step has been the study of the passive control of the separation of the flow past a hump which is placed on a porous wall, by the same macroscopic VANS approach. Finally, general conclusions and possible directions of research in the field are presented in the last chapter.

Résumé

Toute surface naturelle est par essence non lisse, elle est constituée de rugosités plus ou moins régulières et / ou de structures mobiles d'échelles variées. D'un point de vue mécanique des fluides, ces surfaces naturelles proposent des meilleures performances aérodynamiques en termes de réduction de traînée, d'augmentation de la portance ou de contrôle du décollement lorsqu'elles couvrent des corps en mouvement. Cela a été notament prouvé pour des écoulements de couches limites ou de sillage, autour de corps épais. La simulation numérique d'écoulements aux échelles microscopiques autour des surfaces « naturelles » demeure de nos jours encore hors de portée. En conséquence, la thèse a pour objet d'étudier la modélisation du glissement apparent de l'écoulement sur ce genre de surface, modélisée comme un milieu poreux, appliquant la théorie de la moyenne-volumique de Whitaker. Ce modèle mathématique permet globalement de représenter en moyenne les détails de la micro-structure de ses surfaces, tout en conservant une description satisfaisante des phénomènes physiques induits par l'écoulement. Le premier chapitre de ce manuscrit dresse un panorama des efforts antérieurs portant sur la modélisation de ces surfaces en précisant les résultats les plus importants issus de la littérature. Le deuxième chapitre présente la dérivation mathématique des équations de Navier-Stokes en moyenne volumique (VANS en anglais) dans un milieu poreux. Dans le troisième chapitre est étudiée la stabilité de l'écoulement à l'interface entre un fluide libre et un milieu poreux, constitué d'une série de cylindres rigides. La présence de cette couche poreuse est traitée par un terme de traînée dans les équations du fluide. On montre que l'ajout de ce terme réduit les taux d'amplification de l'instabilité de Kelvin-Helmholtz sur toute la gamme des nombre d'onde et ainsi augmente la longueur d'onde du mode le plus amplifié. Dans ce même contexte a été calculée la différence entre un modèle isotrope et une approche tensorielle pour le terme de traînée, afin de déterminer l'approche la plus consistante pour une étude de stabilité de ce type d'écoulement. Cela a mené à la conclusion que le modèle le plus pertinent est celui utilisant le tenseur de perméabilité apparent. Dans le chapitre suivant le tenseur de perméabilité apparent est identifié sur la base d'une centaine de simulations numériques directes, pour un milieu poreux tridimensionnel constitué de cylindres rigides, où le problème de fermeture est abordé par la méthode VANS. Dans ces configurations ce tenseur varie en fonction de quatre paramètres : le nombre de Reynolds, la porosité et l'orientation du gradient moyen de pression définie par deux angles d'Euler. Cette paramétrisation per-

met de capturer les effets tridimensionnels locaux. Cette base de données ainsi constituée a permis de créer, une approche de type kriging, un métamodèle comportemental pour estimer toutes les composantes du tenseur de perméabilité apparente.

Dans le cinquième chapitre sont menées des simulations des équations VANS à l'échelle macroscopique après implémentation du méta-modèle qui autorise des temps de calcul raisonnables. La validation de l'approche à l'échelle macroscopique est effectuée sur un écoulement dans une cavité fermé couverte d'une couche poreuse et une comparaison avec les résultats d'un DNS très précise, homogénéisés a posteriori montre un très bon accord et démontre la pertinence de la démarche. L'étape suivante a consisté en l'étude du contrôle du décollement pour un écoulement autour d'une bosse poreuse par cette même approche VANS macroscopique. Enfin des conclusions générales et des directions de recherche possibles sont présentées dans le dernier chapitre.

Contents

Chapter 1

Poroelastic natural coatings

Nature is the source of all true knowledge. She has her own logic, her own laws, she has no effect without cause nor invention without necessity

- , Leonardo Da Vinci

1.1 Introduction to *biomimetics*

Usually when we are asked to imagine some fast-moving object as an airplane, a boat or a car, common sense leads us to think that its surface should be as smooth as possible. However, if we look around, Nature seems not to agree with the previous statement. In fact most of the surfaces in Nature are not at all smooth, they almost always present more or less regular arrangements of discontinuities at various length scales. Since Nature had a very long time-span to optimize this kind of surfaces we can suppose that they are the best possible options. One should pinpoint that the non-smoothness of these surfaces can be connected to some other biological functions rather than to pure fluid dynamics performance, and of course this can be the case.

An example of natural surface is the shark skin, in figure 1.1 where a segment of the skin is depicted, as it appears under the microscope.

The enlargement shows that the surface is made up by a series of overlapped denticles, and experiments show that they can move and interact with the flow. This interaction is supposed to reduce the shark drag when swimming.

The shark "technology" has somehow been applied by Speedo®. This company has designed famous swimming suits with a surface that mimics the shark skin. Numerous swimmers have broken several world records wearing this swimming suits. This controversial swimmers' performance was due to the fact that the swimsuit compressed the body giving the swimmer a more streamlined shape. Even thought the company has publicized their product as if it were a synthetic shark skin, Oeffner and Lauder [120] have shown that the texture of such swimming suits is somehow different from the shark dermal structure.
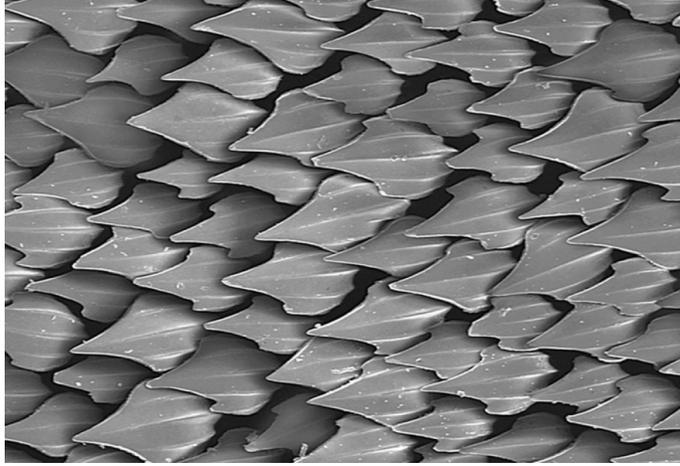
Figure 1.1: Microscope enlarged picture of the shark skin.

In their work the authors have performed swimming experiment of a flat plate with different coatings and they did not found significant speed enhancement with a swimsuit-like surface, but the measurements with real shark skin on the contrary have demonstrated an appreciable improvement of performances.

Poroelastic surfaces find also applications in aeroacoustics; owls are well known for their particularly silent flight, especially in the high frequency spectrum. This characteristic is crucial for the owl in order to capture its preys. Obviously it has inspired the scientific community to study their feathers' configuration and shape.

Figure 1.2: Feathers on owl's wing. Left: trailing edge. Right: leading edge. The differences in shape and mechanical properties, such as rigidity, between the leading and the trailing edges, is a consequence of the different flow regimes in the wing.

Several authors have shown promising results in characterizing the acoustic properties of the owl's skin and their physical mechanisms. In particular Lilley [95] presented three main characteristics of the owl, which can suppress its airborne noise: i) the comb shaped feathers in the leading edge, ii) the fringe at the trailing edge, iii) the presence of numerous

"filaments" in the bottom surface of wings and legs.

Another example is described in the work by Jaworski and Peake [82] who studied the acoustic scattering problem of a poroelastic half-plane encountering an incident plane wave. This configuration, a simplified owl's wing, explains how the properties of this surface can suppress the noise. They concluded that the combined effects of elasticity and porosity can produce a weaker noise amplification.

Recent computational simulations performed by Chen et al. [38] confirm that the leading edge shape of the feathers truly suppresses noise and enhances the lift generation.

Another example of bioinspired aerodynamic surfaces is the butterflies' wing. In figure 1.3 the surface of a "Peacock butterfly" is enlarged in order to show the multiple scales involved. The wing structure present firstly a series of overlapped scales similar to the shark, but if we look closely it can be observed that each scale has a complicate permeable structure.

(a) Magnification 50x   (b) Magnification 1000x   (c) Magnification 5000x
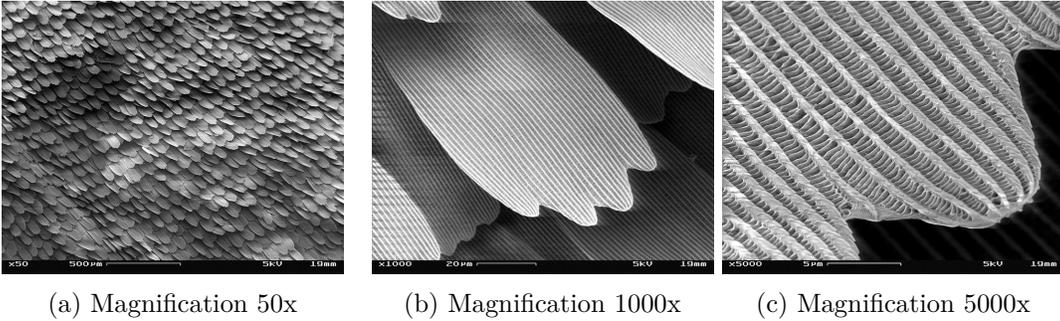
Figure 1.3: Particular of a Peacock butterfly wing, taken with a Scanning Electron Microscope. Images from wikimedia.org

Slegers et al. [146] have studied the effect of such porous structure on the flight performance of butterflies. Using cameras to measure the kinematics of their flight, they can measure their efficiency to "climb" (i.e. generate lift) and the stroke amplitude and frequency. The authors conclude that the porous structure of their wing gives a boost in climbing efficiency of 30%. This result clearly stresses out the importance of the poroelastic coating of the wings. Even though the butterfly flight aerodynamic is extremely complex, it is clear that the peculiar structure of the wing's surface is critical for their aerodynamic performances, as also Srygley and Thomas [148] had confirmed.

The last example concerns super-hydrophobic surfaces. These surfaces, such as that of the lotus leaf, are water repellent, i.e. water can slide over them with less resistance, because of the surface's low wettability. This behavior is caused by the microscopic structure which forms the surface (see figure 1.4). In reality the roughness elements are arranged in a quasi-regular way, in order to be able to capture air pockets that rest within the "valleys". These air inclusions provoke an effective slip at the air-liquid interface that causes skin friction
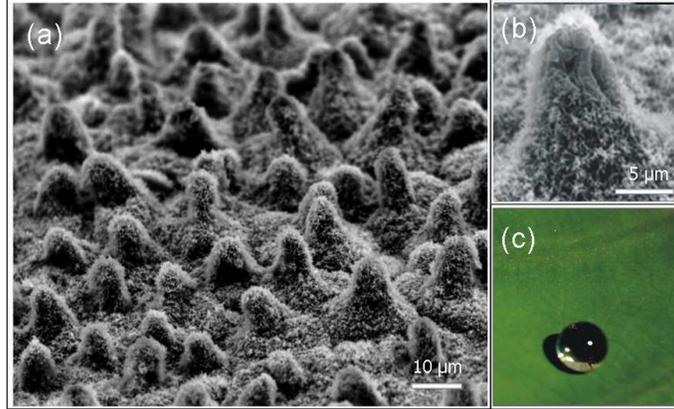
Figure 1.4: (a) Scanning electron microscopy (SEM) image showing the structure of a lotus leaf, (b) higher order of magnification on the single protuberance forming the surface and (c) water drop with high contact angle, attaining an almost spherical shape. Images from Stratakis et al. [149].

reduction. They also change the contact angle of the droplets. The work of Bottaro et al. [21] summarizes some of the above super-hydrofobicity aspect and their applications.

Interested readers can find more examples of biomimetics and broaden the above key aspect in Bhushan [19] and Tropea and Bleckmann [152].

1.2 Riblets and shark-skin surfaces

We have shown that natural surfaces can be an inspiration to find strategies in solving many problems concerning aerodynamics. In the following we especially focus on drag reduction.

It is known that the total drag contribution can be separated into different components and the classical decomposition is between viscous drag (sometimes referred to as skin friction) and pressure drag.

$$\int_{A_\sigma} [\underbrace{(p\mathbf{I} \cdot \mathbf{n}_\sigma) \cdot \mathbf{n}_\parallel}_{\text{pressure drag}} + \underbrace{\boldsymbol{\tau} \cdot \mathbf{n}_\parallel}_{\text{viscous drag}}]\, dA, \tag{1.1}$$

where the shear stress τ, for incompressible and newtornian fluid flow, is defined as:

$$\boldsymbol{\tau} = \mu \left(\nabla \mathbf{v} + \nabla^T \mathbf{v} \right) \cdot \mathbf{n}_\sigma$$

In (1.1) A_σ is the solid interface of some body where a no-slip condition is usually applied and $\mathbf{n}_\sigma$ is its outward normal unit vector to the solid interface A_σ, and $\mathbf{n}_\parallel$ is the unit vector parallel to the fluid direction.

12

The shear stress for incompressible and newtonian fluid flow in the turbulent case is often defined as:

$$\boldsymbol{\tau_t} = (\mu + \mu_t) \left[\nabla \overline{\mathbf{v}} + \nabla^T \overline{\mathbf{v}} \right] \cdot \mathbf{n}_\sigma \tag{1.2}$$

where μ_t is the turbulent viscosity and $\overline{\mathbf{v}}$ is the temporal average velocity. This section is about the existing ways to reduce the viscous part of the drag working only on the surface texture.

1.2.1 Riblets

Most of the industrial applications involve turbulent flows, and as a results there is a lot of research that aims to reduce skin friction in this regime. Table 6.3.1 in the book of McLean [106] includes a wide list of techniques already been proposed on the problem. As the same author pinpoints, the most effective and, probably the most practicable solution, is the surface texture known as riblets. Riblets are alternating ridges aligned in the streamwise flow direction and regularly arranged, as figure 1.5 shows. These surfaces are capable to align the turbulent flow along the mean flow direction, smoothing the fluctuations of the crossflow in the viscous sublayer. The turbulent momentum transfer is reduced as a consequence of reducing these fluctuations close to the surface. In the same manner the surface experiences a lower skin friction.

The viscous drag reduction correlates well with the spacing between the ridges expressed in wall units, s^+. The typical shape of the $\Delta\tau/\tau_0 - s^+$ relation is depicted in figure 1.6, where the vertical axis shows the drag reduction against s^+. This general shape of the curve, in which the skin friction decreases in a certain range of spacing and then increases as the ridge spacing increases, is caused by a competition between the capacity of riblets to obstruct lateral fluid flow and the increase of penetration of high speed vortices inside this manufactured wall irregularity.

This last physical explanation of the riblets' performances is presented in the schematics 1.7, where the gray areas show high skin-friction regions caused by the downwash motion generated by the near-wall vortices. It is clear that, when the riblets are too large, the vortices can penetrate inside the groove and increase the skin friction, due to a larger area exposed to the local velocity. On the contrary, when the riblets are smaller, the high speed vortex only hits the tip of the ridges, so that, only a small local area of the surface experiences high-shear stresses.

The slope m_s of the curve in figure 1.6 can be predicted by linear stability theory (either in laminar and turbulent cases changing the definition of base flow) or by means of empirical correlations(see, e.g., García-Mayoral and Jiménez [62]).

Computing the performance of such surfaces can be expensive, since the most reliable quantitative theory for such problems consist of direct numerical simulations (DNS) or experiments. However there is one theory, besides the already cited expensive ones, that uses the concept of *protrusion height*, shown in figure 1.5, to correlate the shape of these protrusions to the drag reduction (cf. Luchini et al. [96]). In this way the *protrusion*
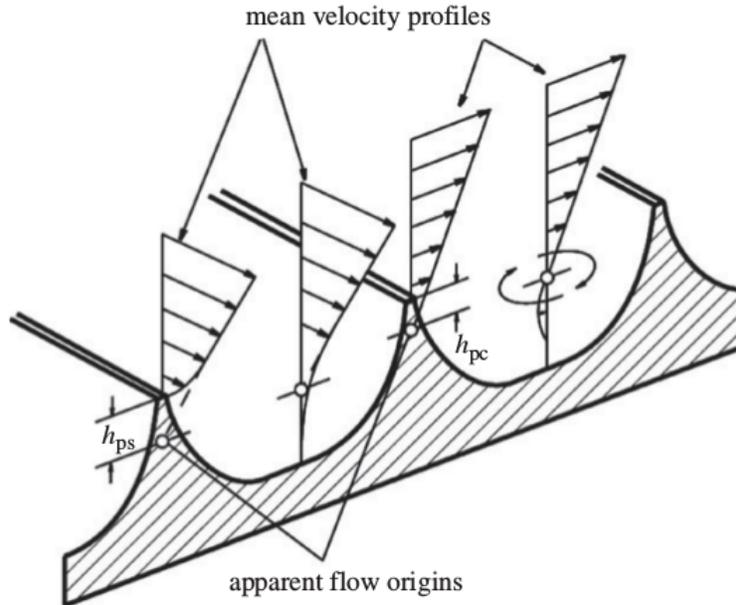
Figure 1.5: Schematics of the *protrusion height* concept. The mean velocity profiles for the stream-wise and crossflow velocities are shown. In presence of a ridge it is possible to extrapolate the point of zero velocity from the velocity gradient outside the riblet; finding respectively, the *streamwise protrusion height* h_{ps} and the *cross-flow protrusion height* h_{pc}. Image from Bechert et al. [16].

height is defined as the vertical distance between the riblet top ridge and the point of zero velocity, extrapolated from the constant velocity gradient outside above the protrusions. It appears that the difference of protrusion heights $(h_{ps} - h_{pc})$ correlates very well with the drag reduction. The two quantities can be computed with a simple Stokes problem over the local geometry of the grooves.

Another important characteristic of riblets is that they are robust in off-design conditions, such as in presence of yaw (misalignment between flow and riblets ridges) and tip ridges erosion (García-Mayoral and Jiménez [61]).

Besides some very specific application such as sailing competitions (the hulls of the USA challengers in the America's Cup 1987 and 2010), the massive use of this technology is still in question. Producing such surfaces in a larger area, like the roof of a car or the wing of an airplane, can be an issue for a routine use, because riblets size needs to be very small to be effective. The riblets need also to be cleaned after each use otherwise some residue (like insect or vegetation) can modify the roughness of the surface and reduce their effectiveness.

Anyhow, riblets-like surfaces have been observed in Nature for many years, for example

14
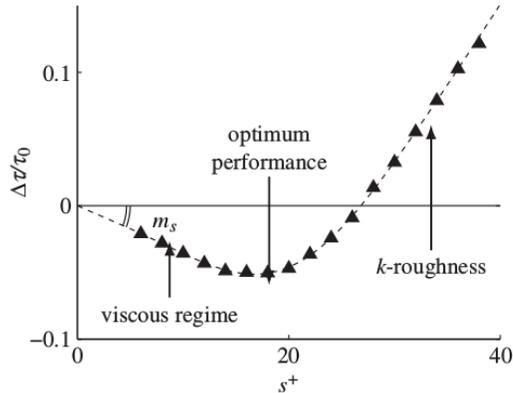
Figure 1.6: Example of drag reduction relation to the ridge spacing. The maximum performance is normally around $s^+ = 15$, the picture shows also that when the riblet are really tightly spaced the laminar case is retrieved. On the contrary when the riblets are far away from one another their performance is comparable to the rough plate case. τ_0 is the wall stress in the case of a smooth flat plate. Image from Jimenez et al. [83].

Martin and Bhushan [103] found that skimmer birds (Rynchops) have riblets like grooves in their beak, since they fly with it under the water surface to catch fishes. However, as already introduced, the most clear example of such natural surfaces is represented by the shark skin.

1.2.2 Shark skin

In their review, Dean and Bhushan [46] present the status of the shape optimization that has been done on the riblets trying to mimic the typical sawtooth shape seen on shark skin, showing that improvements of such geometries over the classical ones has yet to be achieved. Shape optimization on riblets geometry has been studied by Bechert et al. [16], showing that just few percents can be gained compared to the base line geometry.

There are, actually, some controversial results in the literature stating that surfaces, with actual shark skin replica, can indeed increase drag. Boomsma and Sotiropoulos [20] performed some simulations on actual shark skin denticles using the immersed boundary method. These authors simulated various arrangements of the denticles and they found that, in some configurations, the actual drag increases up to 40%. This can be a clue that the shark skin does not work with the same mechanism as riblets do.

Experiments on such geometries are available in the literature (Bechert et al. [15]). The authors built a synthetic surface, made by artificial shark denticles fixed on top of springs. They have shown that, even with the introduction of surface elasticity, the actual drag was increased. However, they pinpointed that the actual shark flow regime was not steady in
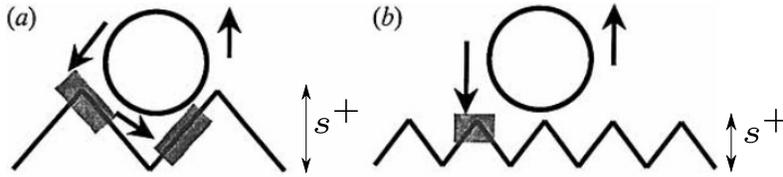
Figure 1.7: Two different sizes of riblets are shown when interacting with a sublayer vortex. In gray it is represented the area where friction is important. Clearly when both sizes are comparable the surface experience a larger friction and the performance is lowered. Image from Choi et al. [39].

the experiments performed, and they speculated that the excellent swimming performance of the shark comes from the separation control that flexible denticles can operate during the periodic oscillating flow that the swimming generates.

In addition an experiment using DPIV on a NACA profile covered with actual skin samples of "Isurus oxyrinchus" mako shark, has been performed by Lang et al. [92], confirming that the flexibility of sharks denticles provides the passive flow control needed to avoid early separation. In fact, the experiments have proven that for angles of attack larger than 15° the flow reversal was almost completely avoided. The same authors noted that different geometries of the denticles can be found in various parts of the shark body, and these differences can be important since flow conditions can change from the head to the tail. Motta et al. [113] performed a detailed collection of flexibility and scale measurement of different shark species that can be valuable for future studies.

Again, swimming experiments from Oeffner and Lauder [120], who used a flat plate covered with real shark skin, confirmed the previous flow control mechanism. They had also made some conjectures about possible thrust enhancing, controlled by the same denticles, that can move away the leading edge vortex.

Also Itoh et al. [80] showed that movable rugosities can outperform riblets. They measured the drag reduction of a seal fur (that present fibrous movable surface) against a riblet surface in an experimental channel. Their results are show in figure 1.8 in which it is visible that seal fur can outperform rigid riblet performance by 5% in a certain span of Reynolds numbers.

Compliant surfaces can, in reality, move accordingly to the surface pressure gradients along the boundary layer and so respond to the pressure fluctuations over the surface itself. This mechanism is already known to be beneficial in delaying the transition to turbulence and many authors have presented theoretical and experimental evidence on the effectiveness of this solution (Carpenter [35], Bushnell et al. [30]).

In conclusion, we have seen that, in order to reduce turbulent skin-friction drag, riblets and natural surfaces use various mechanisms such as: sublayer vortices interaction, compliance and separation control. Such solutions have proven to be effective in various cases
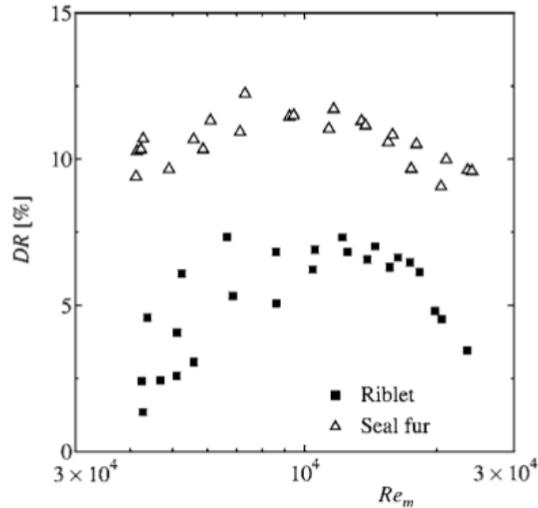
Figure 1.8: Performance comparison between a riblet surface against a seal fur. The drag reduction has been computed as: $DR\% = \dfrac{\Delta\tau}{\tau_0}\%$. Image from Itoh et al. [80].

mostly related to the viscous component of the drag. In the next section we introduce another class of solutions that try to act mostly on the pressure component.

1.3 Permeable surfaces

As permeable surfaces we indicate permeable coatings that usually have a significant thickness; in contrast to riblets, in which the vertical extension outside the wall is limited. In this case the flow can penetrate deep into the porous surface and generate complex interaction mechanisms. The next sections presents an overview of the most notable applications of such permeable surfaces.

1.3.1 Bluff bodies

There is some experimental evidence that, in the laminar regime, generation of some *slip velocity* at the interface between the permeable surface and a fluid, can decrease the skin friction (Beavers and Joseph [14]). However, in the turbulent case it seems that the instabilities developing at the interface can cause a drag increase up to 40% (Jimenez et al. [83]; Breugem et al. [24]); this instability mechanism is further explained in section 1.5. It is important to observe that the permeable surfaces cited in the above references are all rigid.

17

The pressure contribution to the drag is usually the most significant one in bluff bodies applications, and even in highly streamlined body it is around 10% of the total drag. Researchers have tried to find a way to modify the pressure distribution around a bluff body to reduce the associated resistance, and also to damp the force oscillations on the body (drag and/or lift).

The pressure drag on a bluff body depends mostly on the difference between the low pressure on the rear part of the body, where there is usually a separated flow region, and the high pressure in the forward part. This idea is sketched in figure 1.9 where two different pressure distributions are shown; the black one represents the classical solid body, and the green one is the one with a porous layer at the back of the body.
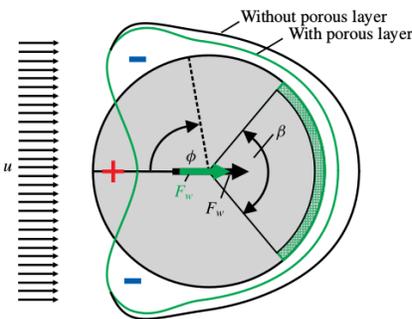
Figure 1.9: Diagram showing an example of angular pressure distribution around a cylinder for viscous flow. The black line is the case of a solid body, the green one is the modified pressure when a porous layer is present on the rear. Image from Klausmann and Ruck [85].

The favorable increase of pressure in the rear point is due to the low speed laminar flow in the porous media that is ejected in the back region where separation takes place. Even in very high speed turbulent flows, the fluid inside the permeable surface exhibits a very high energy loss due to the strong dissipation that the medium provides, resulting in a low speed flow ejected downstream of the body.

The permeable interface, producing a slip velocity, can modify the boundary layer that develops above it producing less shear and vorticity, modifying also the stability characteristics of the flow. The instability around a cylinder is due to the shear layer that forms in the top part of the body, when the flow starts to decelerate. This shear layer exhibits a Kelvin-Helmholtz-type instability that develops in the classical Von-Karman wake.

These two hypothetical mechanisms has been tested using numerical simulations by several authors: Bruneau and Mortazavi [27] [28], Bhattacharyya and Singh [18], Naito and Fukagata [115] and Mimeau et al. [110]. These works studied the flow around some classical two dimensional bluff bodies (cylinder, square cylinder, Ahmed body section, 3D hemisphere) with the addition of a porous layer.

These works show some very promising results, like: decrease of enstropy, lower oscillations in lift, drag reduction, regularization of the wake and lower pressure gradients, even if the porous medium was rigid in the case treated. An example of turbulent flow field downstream to a square cylinder is shown in figure 1.10; the picture demonstrated how the porous layer strongly regularizes the wake.
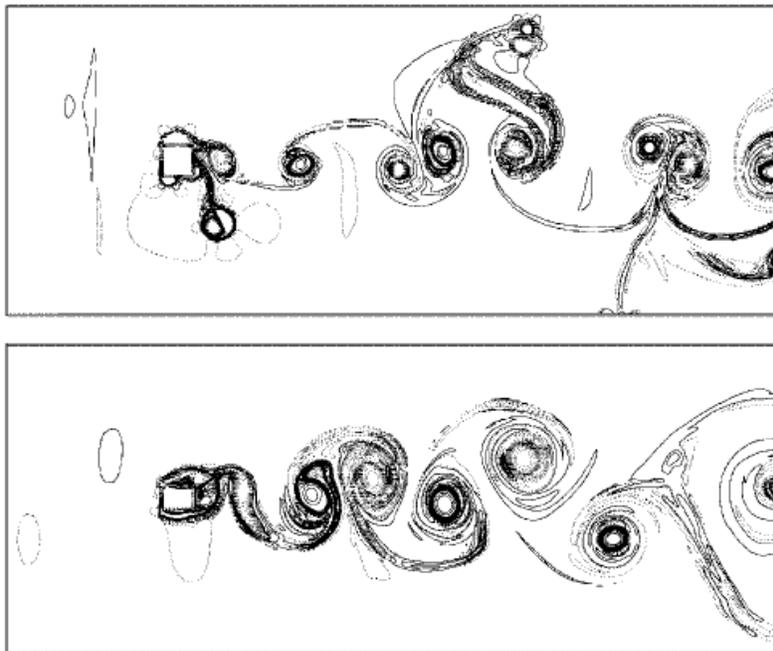
Figure 1.10: Square cylinder vorticity contour for $Re = 30000$. Top: solid case. Bottom: porous case with layer extension $h/D = 10\%$.

The simulations performed by the authors above indicate that porous medium parameters, like the medium porosity or its vertical extension above the solid wall, have important effects on the quantities listed above. The variety of these results seems to indicate (at least qualitatively) that increasing the porous medium extension beyond a certain limit is not beneficial, and they also show that the porosity of the medium should not be excessive in order to be effective (high/medium porosities are the best).

However the above cited works should be taken with some care; only few cases are three-dimensional, they all use a modeling approach for the porous medium based on a simplified version of the VANS (Volume Average Navier-Stokes equations, see section 1.4.2), without performing any validation of the method. Sometimes they also use the equations outside their field of validity (there are discussions in the scientific community about using the previous version of the VANS equations for highly turbulent flows).

The lack of validation reflects the fact that reliable experiments of such porous coatings

19

are almost non existent in the literature. There is also some confusion in the community on how to compute forces on such bodies surrounded by a porous coating. These differences led some authors (Naito and Fukagata [115]) to over-estimate the forces and their predictions are not aligned with the literature. Caltagirone [31] argued on theoretical bases that the approach used by Bruneau and Mortazavi [27] is the correct one for that specific version of the VANS used by all the previous authors.

The approach of Favier et al. [53] differentiates itself from the previous approaches that use the VANS equations. In fact the authors used a numerical method that includes the dynamics of a moving porous medium made of fibers at the back of a cylinder. Their results in a laminar flow case agree with the prediction of a wake stabilization and show some more realistic values of drag reduction, about 15%. However the difficulties in this approach lie in the medium dynamics, it introduce many mechanical parameters that are not easily identifiable for natural surfaces.

A similar model has been used by Venkataraman and Bottaro [155], in which they applied a movable porous coating in the suction side of a NACA airfoil. In this case the synchronization between the oscillations of the structures and the natural frequency of the fluid is responsible for the pressure distribution modification. They have shown the robustness of this solution in a wide range of angles of attack and, in the best case, they have found some lift enhancement and a drag reduction around 10%.

Later on, Rosti et al. [137] worked on a similar configuration with only one movable flap on the low pressure side of the airfoil. Numerical and experimental results qualitatively agree (on the flow mechanism) with the results in the complete porous case.

Zampogna et al. [171] perform some three-dimensional DNS computation over a sphere with cylindrical roughness at Reynolds number equal to 1000, finding a modest drag reduction of 2% compared to a smooth sphere of the same size.

The very few experiments in literature on this porous coatings show less promising results associated to drag reduction.

For example, Heenan and Morrison [75] performed an experiment in which they took a backward facing step with a porous insert in the re-circulation region. Their measurement shows a 13% decrease of the peak of pressure at the wall and a relocation of the detachment point further downstream. A maximum of 9% of drag reduction was measured. The effect of adding a porous surface in this case was to limit the pressure fluctuations that cause the re-circulation bubble unsteadiness.

Later on Klausmann and Ruck [85] studied a 3D cylinder with a porous insert in the back (as in figure 1.9). The authors used a wind tunnel testing with pressure measurements around the body and particle image velocimetry (PIV) flow capture. Their results confirmed that the porous layer on the leeward side increased the pressure in that zone, causing a reduction of drag around 10% over various Reynolds number (in turbulence range). This last measurement was sensitive to the geometrical parameters of the medium as the position and its size. To the best of our knowledge this is the first example of actual measurements of flow quantities using PIV, that can later be used to perform some

validation on different numerical models. The above results are partially confirmed by a similar experimental analysis by Grizzetti et al. [72].

Some other experimental data can be found in the case of flow over aquatic canopies (Zhang and Nepf [172], Segalini et al. [140] and Hamed et al. [74]) even though the published data are limited and the experiments show the presence of a free surface that increases the difficulty of the problem and limits the possible use as a simple validation.

From this section the main physical mechanisms related to permeable surfaces had been introduced. Even thought the different approaches in the literature seem to disagree in the predicted values of some fundamental items such as the forces, a general trend on all data shows that porous coatings can be effectively used in many situations. It is clear that the scientific community needs many more experimental data in order to develop new and improved numerical and theoretical models for such permeable coatings.

1.3.2 Canopy flow

Another important class of flows over poroelastic carpets are the *canopy flows*. These types of problems involve flows over flexible slender structures such as trees and aquatic vegetation. The behavior of wind over plants is very important in a large variety of fields, like: the transport of substances as CO_2 and nutrients or preventing agricultural damage (wind-throw of crop fields); also some similarities with urban canopies can be found (Ghisalberti [63]).

The boundary layer profile over such canopies differs substantially from the rough wall one, as figure 1.11 shows. The vegetation resistance causes the creation of an inflection point in the mean velocity profile that leads to a mixing layer type of instability (Kelvin-Helmholtz instability) near the vegetation top. As a consequence of such instabilities Finnigan [55] indicated that the vegetation can heavily modify the turbulence spectra as a result of the interface instabilities and the coherent structures above it. The two lower pictures in figure 1.11 outline the above statements. The spectrum in case of canopy flow presents a larger peak in the frequency of the mixing layer instability. It presents also a steeper slope in the energy cascade part due to the larger dissipation inside the permeable layer and a high frequency peak associated to the swinging of the plants that can emit or absorb small scales vorticies.

It is clear from the literature that the dynamics of the permeable substrate made by vegetation is extremely important and should always be taken into account to fully generalize the physics in such problems involving moving canopies. Nepf [117] shows how the interface between aquatic plants and the free flow can be largely modified due to the movement of the fibers (most of the plants arms and branches can be viewed as fibers).

In order to discriminate the different behavior of the fibrous structure it is convenient to introduce some non-dimensional parameters typically used in fluid structure interaction problems:
$$m^* = \rho_\beta/\rho_\sigma, \quad C_Y = \rho_\beta U_\infty{}^2 s^3/E, \quad s = H/d,$$
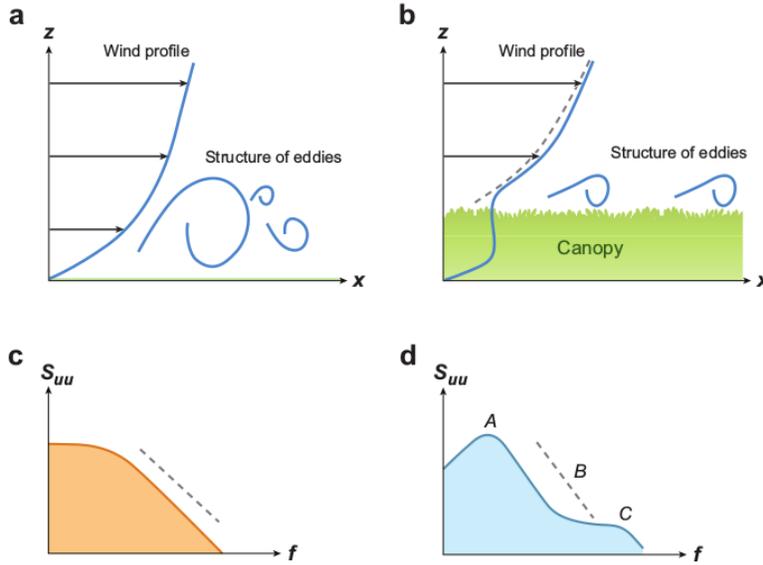
Figure 1.11: Frames **a** and **b** show respectively the schematics of the mean flow over a rough wall and a canopy flow; the difference in the eddy size is clear, also the inflection point in the canopy flow velocity profile is obvious. Frames **c** and **d** show the turbulent spectra for the two different flows above, in the case of rough wall a Kolmogorov type of energy spectrum can be retrieved; in the case of canopy flow it is possible to see a larger peak in the frequency of the mixing layer instability, a steeper slope in the energy cascade part and high frequency peaks at high frequencies. Image from De Langre [45].

where ρ_β is the fluid phase density, ρ_σ is the solid phase density, U_∞ is a free-stream reference velocity, E is the Young modulus of the solid material, H is a reference length for the extension of the solid structure and d is a reference length for the thickness of the material. The first parameter is the *mass ratio* (m^*), the second is called *Cauchy number* (C_Y) and the last one is the *slenderness* (s) of the structure. The mass ratio can be used to quantify the added mass effects caused by solid inertia, however these effects are usually negligible in case of fibrous permeable media. The Cauchy number defines the static deformation of a fiber caused by the fluid flow; when the Cauchy number is greater than unity, important deformations are expected. This last parameter is extremely important since it controls a phenomenon called *reconfiguration* that leads to drag reduction (Gosselin and De Langre [70]; Alvarado et al. [5]). The reconfiguration can be defined as the capability of the structure to adopt a new shape when forced by a flow, usually it become more streamlined to reduce its exposed frontal area with the aim to reduce the total drag. When dealing with this phenomenon one should take into account the frontal area A and the drag coefficient C_D together, in order to avoid misinterpretation of the drag
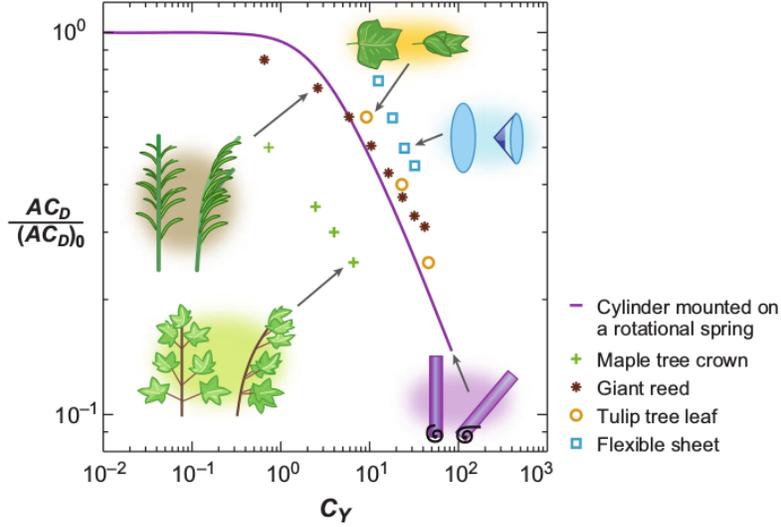
Figure 1.12: Effects of the Cauchy number C_Y on drag reduction. The drag reduction is represented as the ratio between the frontal area A and the drag coefficient C_D in dynamic conditions, divided by the same product wider static conditions (subscript). Image from De Langre [45]

reduction. In figure 1.12 the ratio of the parameter AC_D has been represented for different natural structures against the Cauchy number and it is evident that for a $C_Y > 1$ a drastic drag reduction can be observed.

The overall reconfiguration of the permeable medium can lead to pressure recovery and a wake regularization when applied to a bluff body, as the experiments by Gosselin and De Langre [70] show.

Another important non-dimensional number is the *reduced velocity* (U_R), that can be derived from the previous ones:

$$U_R = \sqrt{C_Y s/m^*}$$

This number is used when dealing with vortex induced vibrations of slender structures. When its value is near one, dynamical coupling between the fluid and the structure is expected, such as resonance or lock-in phenomena[1].

Canopies can also help to prevent separation in the presence of adverse pressure gradients. Belcher et al. [17] have carried out an analysis of the flow over a hill covered with canopies using numerical and experimental data. The authors show how the permeable layer can present a re-circulation region inside the canopy in the decreasing slope side of

---

[1]self-excited vortex-induced vibrations accompanied by the synchronization of the frequency of vortex formation with the frequency of structure vibration.

the hill. This zone move the separation away from the flow over the hill to the internal structure of the canopy.

It is important to point out that the above results are restricted to fibrous or slender structures and they cannot be extrapolated in general for different porous structure and shapes, even though similar mechanisms are expected.

The research on canopy flow embraces a wide range of configurations and this renders any comparison very difficult to make since most of the authors use very different models in various regimes of velocities, using flexible structures with very different shapes. Even if experiments are easier to find, like Segalini et al. [140], Segalini et al. [141], Maza et al. [104], Barsu et al. [11] and Alvarado et al. [5], there is no quantitative mathematical model established for the fluid and structure equations and almost all models available rely on empirical correlations that fit the data in each different application.

1.4 Models for flows through porous surfaces

In this section we want to show some insight of the key characteristics that a model of flows through poroelastic layers should have. In order to be as clear as possible we have taken as example a very simple geometry to sketch the problem: the flow over a wall that includes multiple flexible filaments, in the hypothesis of highly packed fibers the medium can be treated like a porous medium. This simple geometrical configuration still has all the characteristic and difficulties of more interesting applications, such as a bluff body with a poroelastic layer.

Figure 1.13 shows a graphical representation of such a flow. The main fluid direction is aligned with the x_1 axis and the projection of the stream-wise component of the velocity is shown in the plane $x_1 - x_3$. Such flow can bend the filaments that can show a more or less coherent response. The surface that envelops all the filaments lid (Γ) defines the limit between the region of free flow (Ω_f) and that inside the poroelastic medium (Ω_p). Its projection is shown in the $x_1 - x_3$ plane.

In order to computationally solve this problem there are some key points to address:

- Length scales: the flow presents interaction at multiple scales. The flow can develop Kelvin–Helmholtz type instabilities on the interface and they can even penetrate inside the medium and brake up to very small scales eddies. In order to resolve this complex dynamics one should use a very fine numerical mesh (highly computationally expensive) or come up with a model (like in the context of turbulence modeling). Turbulence dynamic can be also problematic; the hypothesis that pore size eddies can exist deep inside the porous medium is still object of some debate in the community. How to deal with such small scale dynamics and/or find a model is not an easy task.

- Compliance or fluid-structure interaction: if the filaments are flexible, they can bend and swing due to the fluid load. We have to take into account a structural model for

24
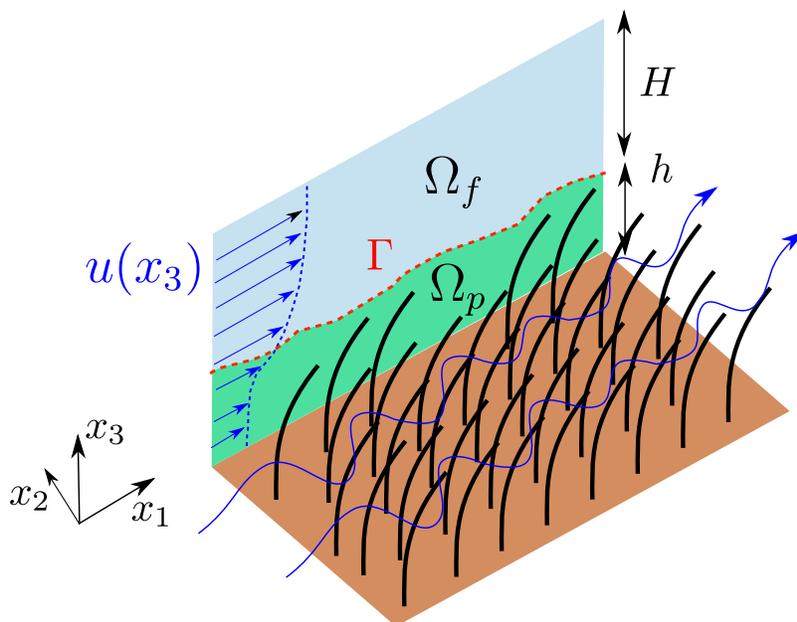
Figure 1.13: Sketch of a fully developed flow over a poroelastic surface made of multiple filaments.

the filaments (by using, for example, the Bernoulli beam equation), including also the computation of energy that the swing motion re-inject inside the fluid. This two-way coupling could also be really computational expensive in the presence of a large number of filaments. If the flexibility is important, one should in principle take into account also the contact and repulsion, elastic coupling, between the fibers. If the porous medium has more complicated shapes, like the scales in the butterfly wing, is even harder to come out with a simplified model for the solid dynamics and the use of a general finite elements discretization is probably a necessity but it increasing also the computational cost of the problem. Another approach consists in deriving a "rheological" model for the medium, in which the average mechanical properties can be found. Such models are applicable only to porous media where the solid inclusions are connected to each other. Such average methods are computationally convenient but their mathematical description can be difficult.

- Anisotropy: the model used should be able to treat permeable surfaces that have different responses when stressed in different directions. For instance, the geometrical arrangement and/or the mechanical properties of the medium can be non-homogeneous, so that the medium can appear more permeable in one direction and show a preferential flow path. The different reaction for a specific direction can be modeled with a tensorial parameter as for the case of the permeability tensor that is

25

basically a generalized drag coefficient.

Dupont et al. [48] performed a LES simulation introducing a two-way coupling for the fluid-structure interaction problem over a carpet of fibers. They validated their simulations with video recording of a similar experiment and the frequency measurements of the Kelvin–Helmholtz instabilities at the interface agrees very well. They have not specified the computational configuration used, but they have mentioned an important high performance computing center in the acknowledgment which made us assume that the computational power involved was substantial. Recently, also Marjoribanks et al. [101] have adopted a similar approach.

Some other examples that solve the fully coupled problem directly are discussed by Monti et al. [112], Pinelli et al. [126], Favier et al. [54] and Revell et al. [135]. However, in their cases the number of filaments is small and so they can be assimilated to isolated filaments rather than to a poroelastic carpet.

Due to the computationally cost of solving the problem directly, the scientific community has came out with other approaches that treat the porous domain with a generalized model that does not resolve the fine scales inside the medium, but instead it expresses them as a function of the length scales present in the fluid domain Ω_f.

These are called homogenization approaches and the key points in such methods are:

- The division of the overall domain in two different parts: the fluid domain Ω_f and the porous domain Ω_p.

- Two different fluid models are used in the two domains. In Ω_f the Navier-Stokes equations for incompressible Newtonian fluids are solved. In the porous part there are a number of different models that add source terms in the former equations to take into account of the presence of the porous medium.

- The two domains should be coupled together with a boundary condition at the interface or a transitional region around the interface is added with its specific treatment.

- A model for the structural mechanics. It can be an averaged model or it can solve the mechanic equations directly.

The key points written above are extensively discussed, in chapter 2, for the homogenization method chosen in this thesis. However, in the next section the two main branches in literature, that take into account the presence of a porous medium layer are summarized in order to give a panoramic on the possible choices.

1.4.1   Isotropic drag models

In the case of flow through vegetation (canopy flows) it is common to use an isotropic drag model[2] to parameterize the drag of the canopy. The drag can be a function of the wall

---

[2]the drag is equal along the three principal directions of the medium.

normal direction, but in most of the applications it is taken as a constant. The isotropic hypothesis can be correct in case of dense vegetation, even if the normal component of the resistance should be smaller. However the resistance in the vertical direction can be approximated in this manner in channel flows where the mean flow is mostly streamwise. On the contrary, in applications where the transpiration at the interface is important (wake control of bluff body) the isotropic drag model is, certainly, not the most adequate.

The drag resistance is included in the Navier-Stokes equations as a source term:

$$\frac{\partial \mathbf{v}_\beta}{\partial t} + \mathbf{v}_\beta \cdot \nabla \mathbf{v}_\beta = -\frac{1}{\rho_\beta}\nabla p_\beta + \nu_\beta \nabla^2 \mathbf{v}_\beta - \frac{1}{2}C_D a |\mathbf{v}_\beta| \mathbf{v}_\beta, \qquad (1.3)$$

where the subscript β indicates variables defined in the fluid phase, and C_D the drag coefficient of the isolated fiber. The parameter a is the frontal area per unit volume of the vegetation, and it is function of the porosity of the medium. The drag term is quadratic in the velocity, but there is some evidence in the literature that the reconfiguration phenomenon can change this relationship (Gosselin and De Langre [70]; Alvarado et al. [5]).

From our point of view this approach lacks of strong mathematical formalism. As a matter of fact the definition of the additional terms of the equations heavily relies on empirical relations. Another issue is that the isotropic hypothesis rules out the possibility to model the anisotropic nature of most surfaces in which we are interested.

In the field of flows through vegetation some authors have successfully used this approach. For example Maza et al. [104] and Maza et al. [105] used it to study wave attenuation and Ghisalberti and Nepf [65], Battiato and Rubol [12] developed simple models for the 2D mean flow over a canopy.

1.4.2 Homogenization models

In this section we want to introduce the most popular approach to derive the equations valid in the porous domain. The fundamental idea is to build a micro-scale model, for both the fluid and the solid, and then derive the macro-scale equations using some averaging operator over the micro-scale.

The two most used homogenization methods are the *Volume Averaging* method (Whitaker [162]) and the *Multiple Scales* method (Mei and Vernescu [108]) which can be broadly classified as perturbations methods. The key differences and the main results retrieved using these approaches are presented in the following.

Volume Averaging

The method of Volume Averaging has been developed to solve transport equations in porous media applications; in this case the presence of two different length scales is obvious, as it can be evinced from figure 1.14.
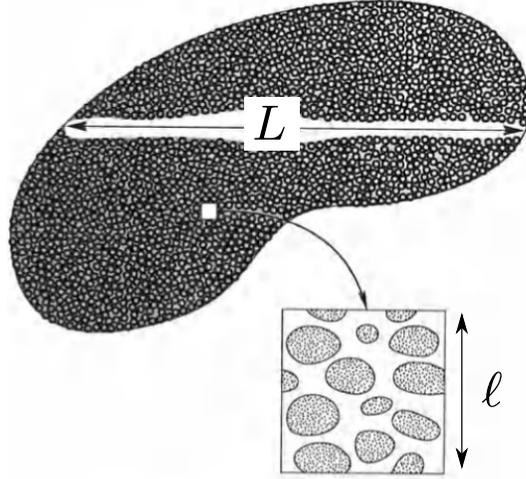
Figure 1.14: Schematics of a porous medium of size L, with a zoom on the microscopic structure and its scale ℓ. Image from Whitaker [162].

The core idea of the methods is to firstly define an average operator as

$$\langle \psi_\beta \rangle^\beta = \frac{1}{V_\beta} \int_V \psi_\beta \, dV,$$

in this case the variable ψ_β represents any vector or scalar variable, associated to the fluid phase (indicated with the sub-script β), that is present in the system of equations that we want to homogenize. For Navier-Stokes equation ψ is the velocity and the pressure. In the above operator V_β is the fluid volume present inside a reference volume V.

The average operator has the purpose to homogenize the equations. The second crucial step of the method is to decompose the variables as proposed by Gray [71]:

$$\psi_\beta = \underbrace{\langle \psi_\beta \rangle^\beta}_{\text{O}(L)} + \underbrace{\tilde{\psi}_\beta}_{\text{O}(\ell)} \tag{1.4}$$

Equation (1.4) shows how each variable can be decomposed into an averaged part which contains only spatial variations at the macro-scale L and a *fluctuation* part that contains only the micro-scale ℓ spatial variations.

Also the decomposition can be substituted in the transport equations, and after some mathematical manipulations it is possible to retrieve the new averaged equations that include only variables of order L. Since this is the method chosen to develop our work, all the technical details are explained in chapter 2.

To introduce briefly some other aspects about this method, we show, as an example, how to derive the homogenized version of the Stokes equation. The described problem is a

steady flow inside a rigid porous medium, like the one in figure 1.14. The Stokes equation valid for the fluid phase, indicated with the β subscript, reads:

$$0 = -\nabla p_\beta + \mu_\beta \nabla^2 \mathbf{v}_\beta, \tag{1.5}$$

It is important to specify that equation (1.5) is valid only in the fluid phase and in order to solve it we have to consider a no-slip boundary condition at the interface with the solid phase, with the difficulties that come to define the complex structure of the solid inclusion. Applying the Averaging Method, we can derive a homogeneous version of (1.5) that is valid in all the domain that includes the two different phases, the solid and the liquid one. The homogenized version of (1.5) is the well known Darcy's equation:

$$\langle \mathbf{v}_\beta \rangle^\beta = -\frac{\mathbf{K}}{\varepsilon \mu_\beta} \nabla \langle p_\beta \rangle^\beta,$$

developed with this approach by Whitaker [159]. It is important to specify that the continuity equation, in his incompressible form, is need to retrieve the averaged equation above.

The Darcy's equation allows to recognize two additional quantities that arise from the averaging procedure. The first one is a scalar called porosity ε that represents the ratio between the volume of the fluid inside a reference volume over the total volume. The second one is the tensor $\mathbf{K}$ called permeability tensor and it expresses the resistance of the porous medium that affects the flow in its motion. The term $\mathbf{K}$ plays the same role as $C_D a$ in the isotropic drag model; the main difference is that the permeability tensor can be computed directly from the geometry of the medium (see chapter 2), i.e. it does not rely on empirical relations. In addition, the tensorial nature of this terms allows to model porous inclusions that are anisotropic.

Applications of the theory include flow where inertial terms are not negligible (Whitaker [161]), porous media with small deformations (Whitaker [160]) and with high deformations (Hussong et al. [77]), turbulent problems (Soulaine and Quintard [147], Breugem et al. [24]), interface between a permeable medium and a free flow (Beavers and Joseph [14]), multi-phase systems (Whitaker [158]), heat transfer (Carbonell and Whitaker [33]) and sound propagation (Firdaouss et al. [57], Lafarge et al. [91]).

It is impossible to go into details in the derivation of the equations for each specific problem, but the key point here has been to show the differences between this method and the isotropic drag model of the previous section.

Multiple Scales

The multiple scales method presents analogies to the previous one and it has also been applied to similar problems in the context of porous media applications.

In this method we start with the assumption of scale separation between ℓ, the microscale, and L, the macro-scale. The scale separation factor can be defined as $\epsilon = \ell/L \ll 1$.

29

Using the same examples as the previous section, we show how to compute the homogenized version of the Stokes equation for fluid flow through porous media. We introduce the micro-scale and the macro-scale coordinates defined respectively as:

$$X_i = \frac{\tilde{x}_i}{L}, \quad x_i = \frac{\tilde{x}_i}{\ell},$$

where $\tilde{x}_i$ are the original eulerian coordinate of the problem. Using the above separation factor it is possible to expand the pressure and velocity as:

$$\psi(X_i, x_i) = \psi^{(0)}(X_i, x_i) + \epsilon\psi^{(1)}(X_i, x_i) + \epsilon^2\psi^{(2)}(X_i, x_i) + O(\epsilon^3),$$

Substituting this decomposition inside the equation (1.5) it is possible to derive a set of hierarchical equations, one for each order of the expansion. It can be shown that analyzing each equation in the set the homogenized equation yields:

$$v_i^{(0)} = -K_{ij}\frac{\partial p^{(0)}}{\partial X_j}, \tag{1.6}$$

in which either the pressure or the velocity fields appears only at the order zero, and the equation depends only on the macro-scale length.

The same permeability tensor $\mathbf{K}$ as before is found, with the same definition and interpretation. It is clear that for this simple problem we end up with the same homogenized equation. The point that has changed is the starting hypotheses of the method and the mathematical development.

A full analysis of the dualism of the two approaches can be found in the work by Davit et al. [44].

The multiple scales method has also been used to study many other problems: inertial effects (Mei and Auriault [107], Skjetne and Auriault [145]), coupling between a free fluid and a porous medium (Mikelic and Jäger [109]), porous media with small deformations (Auriault and Sanchez-Palencia [9]), heat conduction in composites (Auriault [8]), rigid and moving permeable layers (Zampogna and Bottaro [167], Lācis et al. [90] and Zampogna and Bottaro [169]).

1.5   Stability of flows over permeable surfaces

Flows through submerged aquatic plants exhibit large scale vortices at the top of the vegetation, advected along the flow direction and causing a periodic waving of the plants, referred to as monami (if the fluid is air) and honami (in case of water) (Inoue [79], Ackerman and Okubo [1]). The effect of the onset of the monami is depicted qualitatively in figure 1.15.

Vortices arise from the nonlinear amplification of a Kelvin-Helmholtz instability mode, related to the presence of an inflection point in the base flow profile (Asaeda et al. [7]).
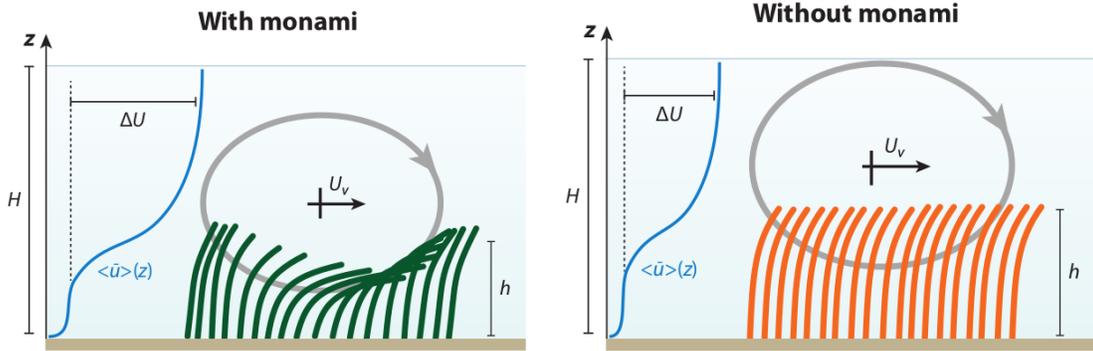
Figure 1.15: Left: when the drag of the canopy is large enough it generates canopy-scale vortices by Kelvin-Helmholtz instability. These vortices may interact with the flexible vegetation and generate a waving motion called monami. Right: when this interaction is too weak, the canopy only bend. Image from Nepf [117].

The profile itself is inflectional because the fluid is slowed down by the drag exerted by the canopy, whose modeling has recently been addressed (Py et al. [127]; Singh et al. [143]; Zampogna et al. [170]; Tilton and Cortelezzi [151]). The correct prediction of the onset and characteristics of the Kelvin-Helmholtz instability is important to assess the effects of turbulence (Finnigan [55], Jimenez et al. [83]) in particular to:

- understand how the vertical exchange of momentum occurs (Ikeda and Kanazawa [78]).

- clarify how the transport of CO_2 and dissolved nutrients or sediments take place. This exchange occur between the obstructed vegetation flow and the free overflow motion (Gambi et al. [59], Eckman [49], Grizzle et al. [73]).

- assess the changes in the morphology of the vegetation in inland or coastal wetlands in response to continuous periodic forcing (Asaeda et al. [7], Patil and Singh [123]).

One of the possible approaches to study how and when these instabilities start is the linear stability analysis. In the following section we briefly introduce the key assumption and simplifications of the method, and some results in the context of permeable surfaces are also presented.

1.5.1 Stability theory generalities

Stability theory covers the modeling of transition of fluid systems towards unstable states eventually leading to turbulence. The theory provides a fast and robust method to compute the frequency and growth rate of the unstable mode in the base flow.

The linear stability relies on the decomposition of the flow variables $\mathbf{q}$ into a steady-state part $\overline{\mathbf{q}}$, called base flow, and an unsteady part $\widetilde{\mathbf{q}}$:

$$\mathbf{q}(\mathbf{x}, t) = \overline{\mathbf{q}}(\mathbf{x}) + \widetilde{\mathbf{q}}(\mathbf{x}, t)$$

Where the unsteady part is small compared to the steady one. We also simplify $\widetilde{\mathbf{q}}$ with the hypothesis to have a general wave form:

$$\widetilde{\mathbf{q}} = \widehat{\mathbf{q}}(\mathbf{x}) e^{i\Theta(\mathbf{x}, t)}$$

where $\widehat{\mathbf{q}}$ is the amplitude function and Θ is the phase of the perturbation. The choice made to determine the time and space dependency of either the phase function and the amplitude determine a certain hierarchy inside the stability theories. This hierarchy depends on how many directions we consider to be periodic in the amplitude function[3]. Figure 1.16 below present each possible choice in literature and the theory that derives from it.

	Denomination	Basic state assumption	Amplitude function	Phase function Θ
Global	TriGlobal	—	$\overline{\mathbf{q}}(x_1, x_2, x_3)$	$\widehat{\mathbf{q}}(x_1, x_2, x_3)$	ωt
	PSE-3D	$\partial_1 \overline{\mathbf{q}} \ll \partial_2 \overline{\mathbf{q}}, \partial_3 \overline{\mathbf{q}}$	$\overline{\mathbf{q}}(x_1^*, x_2, x_3)$	$\widehat{\mathbf{q}}(x_1^*, x_2, x_3)$	$\int^{x_1} \alpha(x') dx' - \omega t$
	BiGlobal	$\partial_1 \overline{\mathbf{q}} = 0$	$\overline{\mathbf{q}}(x_2, x_3)$	$\widehat{\mathbf{q}}(x_2, x_3)$	$\alpha x_1 - \omega t$
Nonlocal	PSE	$\partial_1 \overline{\mathbf{q}} \ll \partial_2 \overline{\mathbf{q}}; \partial_3 \overline{\mathbf{q}} = 0$	$\overline{\mathbf{q}}(x_1^*, x_2)$	$\widehat{\mathbf{q}}(x_1^*, x_2)$	$\int^{x_1} \alpha(x') dx' + \beta x_3 - \omega t$
Local	OSE	$\partial_1 \overline{\mathbf{q}} = \partial_3 \overline{\mathbf{q}} = 0$	$\overline{\mathbf{q}}(x_2)$	$\widehat{\mathbf{q}}(x_2)$	$\alpha x_1 + \beta x_3 - \omega t$

Figure 1.16: Classification of modal linear stability theories. Table from Juniper et al. [84].

In our case we have limited our study to a local approach build on normal mode decomposition, *local stability theory* (LST, also known as *ordinary stability equations* OSE in the denomination of table 1.16). In the LST we make the hypothesis that the amplitude and the base flow depend only on the wall normal spatial coordinate (parallel flow) and the phase function takes into account of the periodicity in time and in the streamwise and cross-flow directions. The last hypothesis should not only be seen as a simplification since there are some problems (such as canopy flows) in which two of the three directions are really homogeneous. The complete formulation is:

$$\widetilde{\mathbf{q}}(\mathbf{x}, t) = \widehat{\mathbf{q}}(x_2) e^{i(\alpha x_1 + \beta x_3 - \omega t)}$$

where x_2 is the wall normal direction, α is the streamwise (x_1) wavenumber, β is the crossflow (x_3) wavenumber and the real part of ω is the temporal frequency.

Casting this form for the pressure and velocity inside the Navier-Stokes equation, the equations that we get describe the evolution of the perturbations, taking the base flow

---

[3]The hierarchy goes from local approach with 2 direction periodic out of 3, to tri-global with all the 3 directions considered space dependent.

as an input of the problem. In order to study the stability of the perturbations in their time evolution, problem known as *temporal stability*, we fix the space perturbation form imposing α and β as real numbers (inputs of the problem) and solving for ω as a complex number. With such choices the problem become a generalized eigenvalue problem for ω:

$$A\widehat{\mathbf{q}} = \omega B\widehat{\mathbf{q}}$$

The solution gives the frequency (real part of the eigenvalues) and the growth-rate (imaginary part) of the perturbation modes (eigenvectors) of the flow.

The above introduction of the method is quite condensed, however there is much literature on the subject (Juniper et al. [84], Criminale et al. [41], Schmid and Henningson [139] and Ortiz et al. [121]). The problem has also been extensively studied in its computational aspects by Canuto et al. [32].

1.5.2   Monami/Honami and Kelvin-Helmholtz rolls

We have already highlighted that the above framework concerning the stability problem has been applied in some porous media flow (canopy) configurations, also including the vegetation movement. Because of the flexibility of the vegetation, some theoretical studies have focused on the modeling of the stems of the aquatic plants and their displacement in response to the forcing by the water flow (Py et al. [127]; Patil and Singh [123]; Gosselin and De Langre [69]; Py et al. [128]).

It has been studied in Finnigan [55] that these large coherent structures control turbulence dynamics over the canopy. Movements of the latter generate sweeps (and ejections) of fluids that generates the counter-rotating stream-wise eddy evolving as Kelvin-Helmholtz rolls. The complex evolution of vortices is shown in figure 1.17.
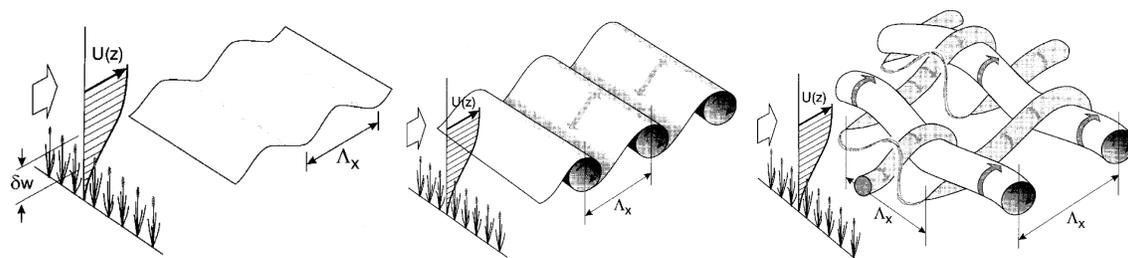
Figure 1.17: Left: first emergence of the Kelvin-Helmholtz instability. The growth-rate is proportional to the shear magnitude at the inflection point. Center: the instability evolves in rollers consisting of high vorticity that are spaced with a similar wave-length Λ_x as the previous stage. Right: secondary instabilities in the rollers lead to their kinking and pairing, coherent structures appear in the transverse and streamwise dimensions. Image from Finnigan [55].

However, Kelvin-Helmholtz vortices occur whether the plants bend or not, and to ascertain causes and effects to first order it is acceptable to focus on rigid porous structures. The flow over and through a submerged array of rigid, cylindrical pillars has been the basis of the approach of Ghisalberti and Nepf [64] [65] [66], who have conducted a series of careful experiments. Their results have often been used by fluid dynamicists to put forth and test theoretical hypotheses to predict the frequency and wavelength of the large scale vortical motion, for a variety of conditions. The configuration studied consists of a regular grid of rigid pillars, orthogonal to the surface, of identical height h. In some of the theoretical models proposed to analyze the stability of this system, the Rayleigh equation is used throughout the water channel, with or without a drag term in correspondence of the canopy (Raupach et al. [134]; Py et al. [127]; Singh et al. [143]; Zampogna et al. [170]; Luminari et al. [97]). The same authors have recently demonstrated that the addition of a drag term through the vegetation reduces the amplification factor of the Kelvin-Helmholtz instability throughout the whole range of wave-numbers and increases mildly the wavelength of the fastest growing mode (Zampogna et al. [170]; Luminari et al. [97]). In chapter 3 we study how the perturbation of the base flow affects the predicted amplification factor and wavelength. We also test the difference between the isotropic drag model and the tensorial approach, in order to show which approach is more robust for stability computations.

1.6 Conclusions

The key point of this introductory chapter was to first present the context of this research. We have started explaining that the idea of using porous surface as aerodynamical performance enhancement from various examples in Nature. Many models based on this idea already exist and we gave an extensive summary of the results present in the literature. We have also presented the key points of the mathematical methods used to derive the porous medium equations that supply a basis for the next chapter in which the volume average method is formally explained.

Chapter 2

Volume Average Method

> *Do not worry about your difficulties in mathematics; I can assure you that mine are still greater.*
>
> - Letter to junior high school student Barbara Wilson,
> January 7, 1943, *Albert Einstein*

2.1 Introduction

In the previous chapter we have already introduced the volume averaging method and how it can be used to derive a macroscopic description of the microscopic system of equations. The homogenized version of the system is valid everywhere in the porous medium domain, and not only in the fluid phase. Theoretical aspect of the volume averaging method can be found in Whitaker [162] [159] [161], Quintard and Whitaker [129] [130] [131] [132] [133] and many other contributions that are introduced in the next chapter. The various steps necessary to derive the local average version of the fluid dynamic equations are listed in the following.

2.2 Homogenization procedure

The mathematical method of volume averaging is based on some fundamental steps that one should follow in order to retrieve the homogenized version of the equations. The main steps are:

- The definition of the averaging operator;

- The use of theorems that permit to interchange the derivation and the averaging operation;

- The decomposition of fields as a sum of mean field and a perturbed field;

- The assumption of length-scales constraints (based on the problem definition) that help to simplify and define a local closure problem.

Such scheme is graphically summarized in Paéz-García et al. [122] and Davit et al. [44]. A similar flowchart of the complete overall procedure is shown in figure 2.1.

2.3 Derivation of VANS equations for 3D incompressible fluids

2.3.1 Navier-Stokes equations

The dynamics of the fluid phase (indicated with the subscript β), inside and above the porous medium, is governed by the Navier-Stokes equation for an incompressible Newtonian fluid:

$$
\begin{cases}
\dfrac{\partial \mathbf{v}_\beta}{\partial t} + \nabla \cdot (\mathbf{v}_\beta \mathbf{v}_\beta) = -\dfrac{1}{\rho_\beta} \nabla p_\beta + \nu_\beta \nabla^2 \mathbf{v}_\beta \\
\nabla \cdot \mathbf{v}_\beta = 0 \\
\mathbf{v}_\beta = \mathbf{v}_\sigma \quad \text{at } A_{\beta\sigma} \\
\mathbf{v}_\beta = \phi(\mathbf{x}, t) \quad \text{at } A_{\beta e}
\end{cases}
\tag{2.1}
$$

where $\mathbf{v}_\beta$, p_β, ρ_β and ν_β stand, respectively, for the velocity, the pressure, the density and the kinematic viscosity of the fluid. The interface between the fluid and the solid is indicated as $A_{\beta\sigma}$, in which the no-slip condition for the velocity apply. In the above boundary condition $\mathbf{v}_\sigma$ is the velocity of the solid phase. $A_{\beta e}$ indicate the external flow boundary of the macroscopic region in which a certain velocity field $\phi(\mathbf{x}, t)$ is defined. Initial conditions should also be specified in order to solve the system, but they do not take active part in the homogenization procedure. The next sections show how to average this system using the volume averaging method.

2.3.2 Definition of the averaging operators

Figure 2.2 shows the schematics of the internal structure of a fibrous porous medium, the important quantities are also indicated in the same picture. The shape of the volumes used in the averaging operations are enclosed in continuous lines. $V|_{\mathbf{x}}$ indicate the volume with centroid $\mathbf{x}$ and $V_\beta|_{\mathbf{x}}$ indicate the fluid volume fraction inside the latter. The coordinate vector $\mathbf{r} = \mathbf{x} + \mathbf{y}$ represents the centroid of another possible volume in which one can compute the average quantities, the boundaries of the same volume are indicated with dotted lines.

$$\mathcal{L}(\psi) = 0$$

$$\langle \mathcal{L}(\psi) \rangle = 0$$

$$\psi = \langle \psi \rangle^\beta + \tilde{\psi}$$

$$\mathcal{L}(\tilde{\psi}) - \left\langle \mathcal{L}(\tilde{\psi}) \right\rangle = \mathcal{S}$$

$$\tilde{\psi} = \mathbf{R} \langle \psi \rangle^\beta$$

$$\mathcal{Q}(\mathbf{R}) = 0$$

$$\mathbf{H} = \mathcal{F}(\mathbf{R})$$

$$\mathcal{M}(\langle \psi \rangle^\beta) = 0$$
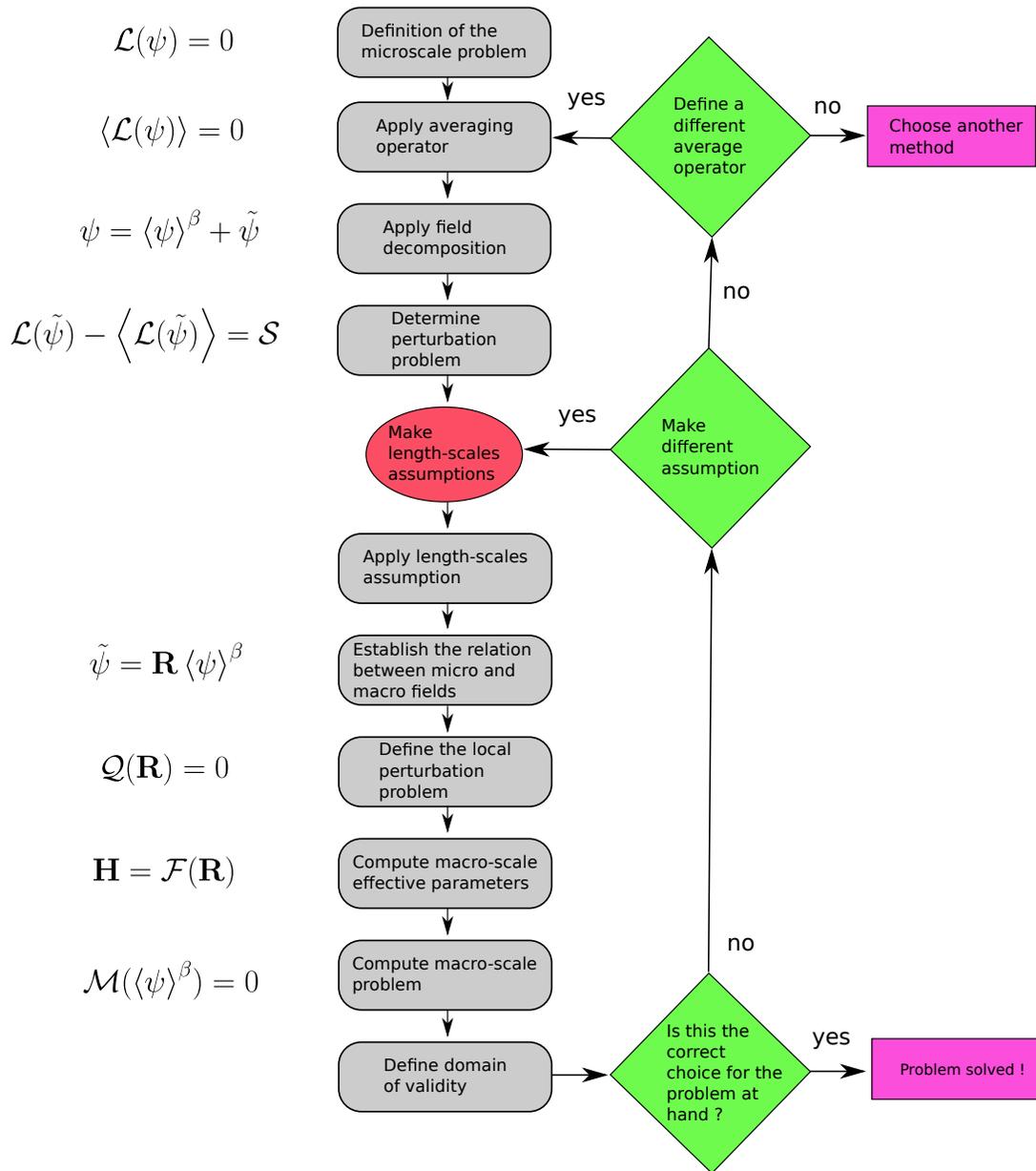
Figure 2.1: Illustration of the volume average homogenization procedure. Image adapted from Davit et al. [44]
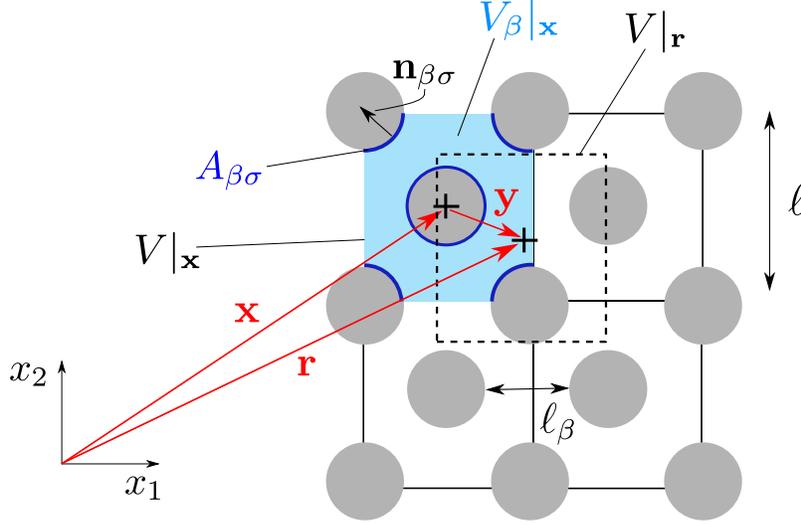
Figure 2.2: A graphical representation of the averaging volumes and interfaces in case of fibrous (ordered) porous media. In this example the fibers are in a staggered arrangement. The edges of the volumes that have centroid position $\mathbf{x}$ are shown in continuous lines and the ones with centroid $\mathbf{r}$ are shown in dotted lines.

Let ψ_β be an arbitrary order tensor (scalar, vector or second order tensor) defined in the fluid phase of the volume V with $\mathbf{x}$ as centroid.

Two different volume averaging operators can be defined. The *intrinsic average* indicated as $\langle . \rangle^\beta$ reads:

$$\langle \psi_\beta \rangle^\beta |_{\mathbf{x}} = \frac{1}{V_\beta(\mathbf{x})} \int_{V_\beta(\mathbf{x})} m(\mathbf{y}) \psi_\beta(\mathbf{x} + \mathbf{y}, t) dV_\beta, \tag{2.2}$$

where m is a weight function defined on V_β and $\mathbf{y}$ is the relative position vector with respect to the centroid $\mathbf{x}$ of the averaging volume V_β.

The second one is the *superficial average* indicated with $\langle \rangle$:

$$\langle \psi_\beta \rangle |_{\mathbf{x}} = \frac{1}{V} \int_{V_\beta(\mathbf{x})} m(\mathbf{y}) \psi_\beta(\mathbf{x} + \mathbf{y}, t) dV_\beta. \tag{2.3}$$

In the two definitions $\mathbf{y}$ is the integration variable. The difference between the two formulations is that the former takes into account the actual fluid fraction in averaging the field instead of the size of the total volume.

In order to use a less heavy notation, the subscript $|_{\mathbf{x}}$ is dropped in the following procedure, but should be kept in mind that the volume averaged quantities are explicitly dependents on the volume center position as both averaging operators are defined as a

volume integral. The size and shape of the integration domain can also be problematic and more details on these issues are presented in section 2.3.3.

The weight function m, has the aim to guarantee smooth volume averaged fields. However, the choice of this formulation depends on the porous medium geometry, as the size of the average volume.

The notation is further simplified if a constant weight is considered, in such a case it is possible to drop it from the average operators. However any shape of the function m can be used without formally changing the final form of the averaged equations.

The porosity of a porous medium cell is defined as:

$$\varepsilon = \frac{V_\beta}{V}, \tag{2.4}$$

it represents how much fluid is actually present inside the averaging volume, in other terms it is an indication of how packed are the fibers of our porous medium.

Using the above definition, it is possible to express a relationship between the two averaging operators:

$$\langle \psi_\beta \rangle = \varepsilon \langle \psi_\beta \rangle^\beta. \tag{2.5}$$

2.3.3 Choice of shape and size of averaging volume and weight function

The problem of choosing the right weight function, for a given porous medium geometry, has been extensively studied by the series of works Quintard and Whitaker [129] [130] [131] [132] [133] and more recently generalized by Davit and Quintard [43].

The authors above distinguish their results for ordered and disordered porous media. They show that in each case a specific size and shape of the weight function (and the volume) is needed in order to produce smooth averaged fields. The volume in which the average procedure is applied is called *reference elementary volume* (REV). Usually for disordered porous media a spherical volume is the most appropriate, and the REV size (ℓ) satisfy the length scale constraint:

$$\ell_\beta \ll \ell \ll L,$$

where ℓ_β is a characteristic distance of the pore spacing. In case of ordered porous media the most appropriate shape is usually a cube with side:

$$O(\ell_\beta) = \ell \ll L.$$

The above constraint can be reinterpreted as the separation of scale parameter in the multiple scale method, $\epsilon = \ell/L \ll 1$.

Ochoa-Tapia and Whitaker [118] confirm the same length-scale constraints even in case of an interface between a free fluid and a porous medium.

The size of the REV (ℓ) should be chosen with the above specifications. These length scale constraints ensure that the volume is large enough that periodic boundary conditions

can be applied in the exterior of the volume. The REV size should also capture all the phenomena that take place at the micro-scale (ℓ_β). If the REV size is the correct one, increasing or decreasing its size should not change the average quantities. The weight function can also help to attenuate variation of the averaged fields due to geometrical inhomogenities of the porous medium. As a matter of fact, it acts as a low-pass filter for the perturbations fields.

The weight function can also play an important role in the interpretation of the averaged equation. As shown later on, in order to retrieve a local form of the VANS equations, the following statement should in principle be true:

$$\left\langle \langle \psi_\beta \rangle |_{\mathbf{r}} \right\rangle |_{\mathbf{x}} = \langle \psi_\beta \rangle |_{\mathbf{x}} \tag{2.6}$$

This means that the averaged field contain small variations at the micro-scale (inside the averaging volume V). In order to satisfy this requirement certain weight functions can perform better than others, although the same conclusion can be derived from the length-scales constraints. In paragraph 2.6, at the end of this chapter, some details of this approximation are further explained.

For a disordered porous medium the *hat function* $m^{\sqcap}$ which has the form:

$$m^{\sqcap}(\mathbf{y}) \begin{cases} \dfrac{1}{V} & |\mathbf{y}| \leqslant \ell/2 \\ 0 & |\mathbf{y}| > \ell/2 \end{cases} \tag{2.7}$$

can be used to produce smooth averaged fields.

Instead, for an ordered porous medium the literature shows that a triangle shaped function, called *cellular filter*, $m^{\triangle}$, performs better:

$$m^{\triangle}(\mathbf{y}) \begin{cases} (\ell/2 - |\mathbf{y}|) & |\mathbf{y}| \leqslant \ell/2 \\ 0 & |\mathbf{y}| > \ell/2 \end{cases} \tag{2.8}$$

Davit and Quintard [43] have recently expanded the required assumption that a m function should satisfy. In general the weight function m should:

- be normalized as: $\displaystyle\int_{V_\beta} m(\mathbf{y})\, dV_\beta = 1$;

- have compact support;

- satisfy: $m * \psi_\beta \in C^k$, where k represent the order at which the equation (2.6) is exact[1];

- satisfy[2]: $(m\, \mathcal{P}^j(\mathbf{y})) * \psi_\beta = \begin{cases} 0 & \text{for odd j,} \\ const & \text{for even j,} \end{cases}$

---

[1] see equation (2.9).
[2] this requirement is clarified in paragraph 2.6.

where $\mathcal{P}^j(\mathbf{y})$ is a polynomial of order j. The last requirement uses the fact that the average operation can also be defined as a convolution product between the weight function and the flow field quantities (Marle [102]):

$$\langle\psi_\beta\rangle|_\mathbf{x} = \frac{1}{V}\int_{V_\beta(\mathbf{x})} m(\mathbf{y})\psi_\beta(\mathbf{x}+\mathbf{y},t)dV_\beta = m*\psi_\beta \tag{2.9}$$

The choice of the weight function shape is very important, however previous works in which the authors had implicitly used $m^\sqcap$ are not wrong. As a matter of fact, if the assumption of well behaved fields holds[3] then the homogenized equations are the correct one. However neglecting the use of the proper weight function can induce some problem on the interpretation of the averaged fields[4]; as a consequence particular care should be used especially when making comparison to experiments.

In the following derivation of the equations no weight function is used inside the averaged operators, in order to not make the notation too heavy. In any case in the following sections it is indicated whether this special hypothesis on the weight function is required.

2.3.4 Theorems involving derivatives of spatial averaged quantities

The purpose of these theorems is to be able to swap the derivative and the volume average operation.

Theorem 1 (Spatial averaging theorem). *Let ψ_β be a scalar quantity defined in the fluid phase β, then:*

$$\langle\nabla\psi_\beta\rangle = \nabla\langle\psi_\beta\rangle + \frac{1}{V}\int_{A_{\beta\sigma}}\psi_\beta\mathbf{n}_{\beta\sigma}\,dA \tag{2.10}$$

In the above $\langle\psi_\beta\rangle$ is evaluated at $\mathbf{x}$ and the operator ∇ expresses the differentiation operation with respect to $\mathbf{x}$. Also $\mathbf{n}_{\beta\sigma}$ represent the unit outward vector of the surface $A_{\beta\sigma}(t)$, directed from the β phase to the σ phase.

Corollary 1 (Vector form of (2.10)). *The vector form of the spatial averaging theorem is given by:*

$$\langle\nabla\cdot\boldsymbol{\psi}_\beta\rangle = \nabla\cdot\langle\boldsymbol{\psi}_\beta\rangle + \frac{1}{V}\int_{A_{\beta\sigma}}\boldsymbol{\psi}_\beta\cdot\mathbf{n}_{\beta\sigma}\,dA \tag{2.11}$$

Corollary 2. *Applying the theorem (2.10) to a constant field $\psi_\beta = 1$ the following relation can be found:*

$$\nabla\varepsilon = -\frac{1}{V}\int_{A_{\sigma\beta}}\mathbf{n}_{\beta\sigma}dA, \tag{2.12}$$

---

[3]it means that the equation (2.6) can be verified a posteriori.
[4]as Quintard and Whitaker [129] show for the example of the hydrostatic pressure.

Theorem 2 (Transport theorem). *Let ψ_β be a quantity defined in the fluid phase β, then:*

$$\left\langle \frac{d\psi_\beta}{dt} \right\rangle^\beta = \frac{\partial \langle \psi_\beta \rangle^\beta}{\partial t} + \int_{A_{\beta\sigma}(t)} \mathbf{n}_{\beta\sigma} \cdot \psi_\beta \, \mathbf{v}_\sigma \, dA, \tag{2.13}$$

where $\mathbf{v}_\sigma$ is the point velocity of the solid-fluid interface $A_{\beta\sigma}$.

The three theorems and the corollary are essential to develop the closed form of the equations. One interesting thing to pay attention to is that the theorems switch the average and derivative operation but always introduce a non local integral term.

2.3.5 Averaged continuity equations

We start by finding the averaged version of the continuity equation in (2.1):

$$\langle \nabla \cdot \mathbf{v}_\beta \rangle = 0 \tag{2.14}$$

Applying theorem (2.11) to the previous equation we get:

$$\langle \nabla \cdot \mathbf{v}_\beta \rangle = \nabla \cdot \langle \mathbf{v}_\beta \rangle + \frac{1}{V} \int_{A_{\beta\sigma}} \mathbf{v}_\beta \cdot \mathbf{n}_{\beta\sigma} \, dA.$$

The boundary condition at the interface ($\mathbf{v}_\sigma = \mathbf{v}_\beta$) implies that the integral above can be modified as:

$$\langle \nabla \cdot \mathbf{v}_\beta \rangle = \nabla \cdot \langle \mathbf{v}_\beta \rangle + \frac{1}{V} \int_{A_{\beta\sigma}} \mathbf{v}_\sigma \cdot \mathbf{n}_{\beta\sigma} \, dA.$$

Now we rewrite the last term as if it were a result of the transport theorem applied to a constant unitary scalar field:

$$\langle \nabla \cdot \mathbf{v}_\beta \rangle = \nabla \cdot \langle \mathbf{v}_\beta \rangle + \frac{\partial}{\partial t} \frac{1}{V} \int_{V_\beta} dV - \frac{1}{V} \int_{V_\beta} \frac{\partial 1}{\partial t} \, dV,$$

where the last integral is zero. The first term can be further developed, obtaining finally the averaged continuity equation:

$$\nabla \cdot \langle \mathbf{v}_\beta \rangle + \frac{\partial \varepsilon}{\partial t} = 0. \tag{2.15}$$

2.3.6 Averaged momentum equations

We seek the average version of the momentum equation (2.1) re-written below:

$$\frac{\partial \mathbf{v}_\beta}{\partial t} + \nabla \cdot (\mathbf{v}_\beta \mathbf{v}_\beta) = -\frac{1}{\rho_\beta} \nabla p_\beta + \nu_\beta \nabla^2 \mathbf{v}_\beta. \tag{2.16}$$

In order to keep the procedure readable the development of each term is performed separately, in the same order as they appear in equation (2.16).

Temporal derivative term

Using theorem (2.13) we can write the first term of the equation as:

$$\left\langle \frac{\partial \mathbf{v}_\beta}{\partial t} \right\rangle = \frac{\partial \langle \mathbf{v}_\beta \rangle}{\partial t} - \frac{1}{V} \int_{A_{\beta\sigma}} \mathbf{v}_\beta (\mathbf{v}_\sigma \cdot \mathbf{n}_{\beta\sigma}) \, dA. \tag{2.17}$$

Convective term

Theorem (2.11) applied to the convective term gives:

$$\langle \nabla \cdot (\mathbf{v}_\beta \mathbf{v}_\beta) \rangle = \nabla \cdot \langle \mathbf{v}_\beta \mathbf{v}_\beta \rangle + \frac{1}{V} \int_{A_{\beta\sigma}} (\mathbf{v}_\beta \mathbf{v}_\beta) \cdot \mathbf{n}_{\beta\sigma} \, dA. \tag{2.18}$$

The boundary condition at the interface ($\mathbf{v}_\sigma = \mathbf{v}_\beta$) implies that the integrals inside the convective and temporal part are equal, so the left end side of the momentum equation becomes:

$$\text{LHS} = \frac{\partial \langle \mathbf{v}_\beta \rangle}{\partial t} + \nabla \cdot \langle \mathbf{v}_\beta \mathbf{v}_\beta \rangle. \tag{2.19}$$

Pressure term

The pressure term is also expanded using theorem (2.10):

$$\left\langle -\frac{1}{\rho_\beta} \nabla p_\beta \right\rangle = -\frac{1}{\rho_\beta} \nabla \langle p_\beta \rangle - \frac{1}{V} \int_{A_{\beta\sigma}} \frac{p_\beta}{\rho_\beta} \mathbf{n}_{\beta\sigma} \, dA. \tag{2.20}$$

Diffusion term

Here we fist use the identity $\nabla^2 = \nabla \cdot (\nabla)$, then we apply theorem (2.12) directly to this expansion to get:

$$\left\langle \nu_\beta \nabla^2 \mathbf{v}_\beta \right\rangle = \langle \nu_\beta \nabla \cdot \nabla \mathbf{v}_\beta \rangle = \nabla \cdot \langle \nu_\beta \nabla \mathbf{v}_\beta \rangle + \frac{1}{V} \int_{A_{\beta\sigma}} \nu_\beta \mathbf{n}_{\beta\sigma} \cdot \nabla \mathbf{v}_\beta \, dA. \tag{2.21}$$

Now using theorem (2.10) on $\langle \nabla \mathbf{v}_\beta \rangle$ we get:

$$
\begin{aligned}
\left\langle \nu_\beta \nabla^2 \mathbf{v}_\beta \right\rangle &= \nabla \cdot \nu_\beta \nabla \langle \mathbf{v}_\beta \rangle + \nabla \cdot \left(\frac{1}{V} \int_{A_{\beta\sigma}} \nu_\beta \mathbf{n}_{\beta\sigma} \mathbf{v}_\beta \, dA \right) + \frac{1}{V} \int_{A_{\beta\sigma}} \nu_\beta \mathbf{n}_{\beta\sigma} \cdot \nabla \mathbf{v}_\beta \, dA \\
&= \nu_\beta \nabla^2 \langle \mathbf{v}_\beta \rangle + \nabla \cdot \left(\frac{1}{V} \int_{A_{\beta\sigma}} \nu_\beta \mathbf{n}_{\beta\sigma} \mathbf{v}_\beta \, dA \right) + \frac{1}{V} \int_{A_{\beta\sigma}} \nu_\beta \mathbf{n}_{\beta\sigma} \cdot \nabla \mathbf{v}_\beta \, dA,
\end{aligned}
$$

The first integral term is null in case of rigid porous media and is also null in case of rigid motion of the solid. A manipulation procedure of this term has been proposed in Hussong

43

et al. [77] but its influence in the poroelastic case is yet to be clarified. In the following development this term will be included for completeness although, it is out of scope of our study.

Before continuing the development, by summing all the terms together we get:

$$\frac{\partial \langle \mathbf{v}_\beta \rangle}{\partial t} + \nabla \cdot \langle \mathbf{v}_\beta \mathbf{v}_\beta \rangle = -\frac{1}{\rho_\beta} \nabla \langle p_\beta \rangle + \nu_\beta \nabla^2 \langle \mathbf{v}_\beta \rangle +$$

$$+ \frac{1}{V} \int_{A_{\beta\sigma}} \mathbf{n}_{\beta\sigma} \cdot \left(-\frac{p_\beta}{\rho_\beta} \mathbf{I} + \nu_\beta \nabla \mathbf{v}_\beta \right) \, dA + \nabla \cdot \left(\frac{1}{V} \int_{A_{\beta\sigma}} \nu_\beta \mathbf{n}_{\beta\sigma} \mathbf{v}_\beta \, dA \right). \quad (2.22)$$

This is still not the averaged version of the momentum equation, since it has the presence of the non-homogeneous term $\langle \mathbf{v}_\beta \mathbf{v}_\beta \rangle$ and some local (microscopic) variables remains inside the integral term. In the next section these two terms are treated in order to make them function only of averaged quantities.

2.3.7   Length scale decomposition

The decomposition proposed by Gray [71] is now used to get the average version of the problem (2.1):

$$\psi_\beta(\mathbf{r}, t) = \langle \psi_\beta \rangle^\beta |_{(\mathbf{r}, t)} + \tilde{\psi}_\beta(\mathbf{r}, t), \quad (2.23)$$

where $\tilde{\psi}_\beta$ is the microscopic scale contribution and $\langle \psi_\beta \rangle^\beta$ the volume-averaged one. The two contributions should be added together to obtain the local field values for the considered quantity ψ_β. In this equation the independent variable is $\mathbf{r}$ because we want to put emphasis on the fact that the Gray's decomposition is valid at every point in the space and, not only in the REV's centroid $\mathbf{x}$. The implication of computing this decomposition in a point in space rather than $\mathbf{x}$ are explained in paragraph 2.6. This decomposition has been introduced in order to separate the different scales of the spatial variation of the fields, and so separate the low frequencies from the high ones.

If the hypothesis of this decomposition holds, it is possible to demonstrate that the average value of the perturbation field vanishes[5]:

$$\left\langle \tilde{\psi}_\beta \right\rangle = \langle \psi_\beta \rangle - \left\langle \langle \psi_\beta \rangle^\beta \right\rangle \approx \langle \psi_\beta \rangle - \varepsilon \langle \psi_\beta \rangle^\beta = \langle \psi_\beta \rangle - \langle \psi_\beta \rangle = 0.$$

Using the above results, the non-linear term in equation (2.22) can be converted to:

$$\langle \mathbf{v}_\beta \mathbf{v}_\beta \rangle = \left\langle \langle \mathbf{v}_\beta \rangle^\beta \langle \mathbf{v}_\beta \rangle^\beta \right\rangle + \left\langle \langle \mathbf{v}_\beta \rangle^\beta \tilde{\mathbf{v}}_\beta \right\rangle + \left\langle \tilde{\mathbf{v}}_\beta \langle \mathbf{v}_\beta \rangle^\beta \right\rangle + \langle \tilde{\mathbf{v}}_\beta \tilde{\mathbf{v}}_\beta \rangle = \varepsilon \langle \mathbf{v}_\beta \rangle^\beta \langle \mathbf{v}_\beta \rangle^\beta + \langle \tilde{\mathbf{v}}_\beta \tilde{\mathbf{v}}_\beta \rangle. \quad (2.24)$$

---

[5]the paragraph 2.6 addresses specifically the hypothesis behind this result.

For each integral term of (2.22) the same field decomposition should be applied:

$$
\begin{aligned}
\frac{1}{V} \int_{A_{\beta\sigma}} - \left(\frac{p_\beta}{\rho_\beta} \mathbf{I} \right) \cdot \mathbf{n}_{\beta\sigma} \, dA &= \frac{1}{V} \int_{A_{\beta\sigma}} -\frac{1}{\rho_\beta} \left(\langle p_\beta \rangle^\beta + \tilde{p}_\beta \right) \mathbf{n}_{\beta\sigma} \, dA \\
&= \frac{1}{\rho_\beta} \nabla \varepsilon \, \langle p_\beta \rangle^\beta - \frac{1}{V} \int_{A_{\beta\sigma}} \frac{\tilde{p}_\beta}{\rho_\beta} \mathbf{n}_{\beta\sigma} \, dA, \qquad (2.25)
\end{aligned}
$$

$$
\begin{aligned}
\frac{1}{V} \int_{A_{\beta\sigma}} \nu_\beta \mathbf{n}_{\beta\sigma} \cdot \nabla \mathbf{v}_\beta \, dA &= \frac{1}{V} \int_{A_{\beta\sigma}} \nu_\beta \mathbf{n}_{\beta\sigma} \cdot \nabla (\langle \mathbf{v}_\beta \rangle^\beta + \tilde{\mathbf{v}}_\beta) \, dA \\
&= -\nu_\beta \nabla \langle \mathbf{v}_\beta \rangle^\beta \cdot \nabla \varepsilon + \frac{1}{V} \int_{A_{\beta\sigma}} \nu_\beta \mathbf{n}_{\beta\sigma} \cdot \nabla \tilde{\mathbf{v}}_\beta \, dA. \quad (2.26)
\end{aligned}
$$

The momentum equation now reads:

$$
\begin{aligned}
\frac{\partial \langle \mathbf{v}_\beta \rangle}{\partial t} + \nabla \cdot (\varepsilon \langle \mathbf{v}_\beta \rangle^\beta \langle \mathbf{v}_\beta \rangle^\beta) + \nabla \cdot \langle \tilde{\mathbf{v}}_\beta \tilde{\mathbf{v}}_\beta \rangle &= -\frac{1}{\rho_\beta} \nabla \langle p_\beta \rangle + \nu_\beta \nabla^2 \langle \mathbf{v}_\beta \rangle - \nu_\beta \nabla \langle \mathbf{v}_\beta \rangle^\beta \cdot \nabla \varepsilon \\
+ \frac{1}{\rho_\beta} \nabla \varepsilon \, \langle p_\beta \rangle^\beta + \frac{1}{V} \int_{A_{\beta\sigma}} \mathbf{n}_{\beta\sigma} \cdot \left(-\frac{\tilde{p}_\beta}{\rho_\beta} \mathbf{I} + \nu_\beta \nabla \tilde{\mathbf{v}}_\beta \right) \, dA &+ \nabla \cdot \left(\frac{1}{V} \int_{A_{\beta\sigma}} \nu_\beta \mathbf{n}_{\beta\sigma} \mathbf{v}_\beta \, dA \right).
\end{aligned}
$$

$$(2.27)$$

At this step the momentum equation is not closed since both the averaged quantities and perturbation fields are present. In order to overcome this problem the intrinsic version of the equation will be derived in the next section.

2.3.8 Intrinsic average form

In order to get the intrinsic average formulation, relation (2.5) is used to express surface averaged quantities in terms of intrinsic ones. First, the continuity equation becomes:

$$
\nabla \cdot (\varepsilon \langle \mathbf{v}_\beta \rangle^\beta) + \frac{\partial \varepsilon}{\partial t} = 0.
$$

The temporal derivative term of the momentum equation becomes:

$$
\frac{\partial \langle \mathbf{v}_\beta \rangle}{\partial t} = \frac{\partial (\varepsilon \langle \mathbf{v}_\beta \rangle^\beta)}{\partial t} = \frac{\partial \varepsilon}{\partial t} \langle \mathbf{v}_\beta \rangle^\beta + \varepsilon \frac{\partial \langle \mathbf{v}_\beta \rangle^\beta}{\partial t}.
$$

Applying the same relation to the viscous term yields:

$$
\nabla^2 \langle \mathbf{v}_\beta \rangle = \nabla^2 \left(\varepsilon \langle \mathbf{v}_\beta \rangle^\beta \right) = \varepsilon \nabla^2 \langle \mathbf{v}_\beta \rangle^\beta + \langle \mathbf{v}_\beta \rangle^\beta \nabla^2 \varepsilon + 2 \nabla \varepsilon \nabla \langle \mathbf{v}_\beta \rangle^\beta, \qquad (2.28)
$$

45

and the pressure term is also transformed into:

$$\nabla\langle p_\beta\rangle = \nabla\left(\varepsilon\langle p_\beta\rangle^\beta\right) = \varepsilon\nabla\langle p_\beta\rangle^\beta + \langle p_\beta\rangle^\beta\nabla\varepsilon. \tag{2.29}$$

Summing up all the terms, we get:

$$\begin{aligned}
&\frac{\partial\varepsilon}{\partial t}\langle\mathbf{v}_\beta\rangle^\beta + \varepsilon\frac{\partial\langle\mathbf{v}_\beta\rangle^\beta}{\partial t} + \nabla\cdot\left(\varepsilon\langle\mathbf{v}_\beta\rangle^\beta\langle\mathbf{v}_\beta\rangle^\beta\right) + \nabla\cdot\left(\langle\tilde{\mathbf{v}}_\beta\tilde{\mathbf{v}}_\beta\rangle\right) \\
&= -\varepsilon\,\nabla\left(\frac{\langle p_\beta\rangle^\beta}{\rho_\beta}\right) - \nabla\varepsilon\,\frac{1}{\rho_\beta}\langle p_\beta\rangle^\beta + \nu_\beta\varepsilon\,\nabla^2\langle\mathbf{v}_\beta\rangle^\beta + \nu_\beta\langle\mathbf{v}_\beta\rangle^\beta\,\nabla^2\varepsilon + 2\nu_\beta\nabla\langle\mathbf{v}_\beta\rangle^\beta\cdot\nabla\varepsilon \\
&\quad + \frac{1}{\rho_\beta}\nabla\varepsilon\langle p_\beta\rangle^\beta - \frac{1}{V}\int_{A_{\beta\sigma}}\frac{\tilde{p}_\beta}{\rho_\beta}\mathbf{n}_{\beta\sigma}\,dA \\
&\quad -\nu_\beta\nabla\langle\mathbf{v}_\beta\rangle^\beta\cdot\nabla\varepsilon + \frac{1}{V}\int_{A_{\beta\sigma}}\nu_\beta\mathbf{n}_{\beta\sigma}\cdot\nabla\tilde{\mathbf{v}}_\beta\,dA \\
&\quad +\nabla\cdot\left(\frac{1}{V}\int_{A_{\beta\sigma}}\nu_\beta\mathbf{n}_{\beta\sigma}\mathbf{v}_\beta\,dA\right).
\end{aligned} \tag{2.30}$$

After the proper simplification we have the final versions of the Navier-Stokes system of equations (2.1) using intrinsic quantities:

$$\begin{cases}
\begin{aligned}
\frac{\partial\varepsilon}{\partial t}\langle\mathbf{v}_\beta\rangle^\beta + \varepsilon\frac{\partial\langle\mathbf{v}_\beta\rangle^\beta}{\partial t} \quad &+\nabla\cdot\left(\varepsilon\langle\mathbf{v}_\beta\rangle^\beta\langle\mathbf{v}_\beta\rangle^\beta\right) + \nabla\cdot\left(\langle\tilde{\mathbf{v}}_\beta\tilde{\mathbf{v}}_\beta\rangle\right) \\
&= -\varepsilon\nabla\left(\frac{\langle p_\beta\rangle^\beta}{\rho_\beta}\right) + \nu_\beta\varepsilon\nabla^2\langle\mathbf{v}_\beta\rangle^\beta + \nu_\beta\nabla\langle\mathbf{v}_\beta\rangle^\beta\cdot\nabla\varepsilon + \nu_\beta\langle\mathbf{v}_\beta\rangle^\beta\nabla^2\varepsilon \\
&\quad +\frac{1}{V}\int_{A_{\beta\sigma}}\mathbf{n}_{\beta\sigma}\cdot\left(-\frac{\tilde{p}_\beta}{\rho_\beta}\mathbf{I} + \nu_\beta\nabla\tilde{\mathbf{v}}_\beta\right)\,dA \\
&\quad +\nabla\cdot\left(\frac{1}{V}\int_{A_{\beta\sigma}}\nu_\beta\mathbf{n}_{\beta\sigma}\mathbf{v}_\beta\,dA\right),
\end{aligned} \\
\nabla\cdot(\varepsilon\langle\mathbf{v}_\beta\rangle^\beta) + \dfrac{\partial\varepsilon}{\partial t} = \quad 0.
\end{cases} \tag{2.31}$$

It is important to highlight that the intrinsic momentum equation explicitly depends on the porosity of the medium, because of the terms involving gradients of the porosity field. In applications where the porosity can vary spatially, like the interface of a porous medium, this formulation has the advantage to treat explicitly the interface non-homogeneities [6].

Equation (2.31) is also *non-local* since it has volume-averaged quantities and surface integrals. These terms need some explicit manipulation in order to get a close formulation of

---

[6]further discussion of the interface treatment is presented in paragraph 2.5

the above system. In the next paragraphs a closure formulation of these terms is discussed. Usually these terms are named *sub-filter stresses* $\boldsymbol{\zeta}$ and *microscopic force* $\mathbf{F}^m$:

$$\boldsymbol{\zeta} = \nabla \cdot \left(\langle \tilde{\mathbf{v}}_\beta \tilde{\mathbf{v}}_\beta \rangle \right),$$

$$\mathbf{F}^m = \frac{1}{V} \int_{A_{\beta\sigma}} \mathbf{n}_{\beta\sigma} \cdot \left(-\frac{\tilde{p}_\beta}{\rho_\beta} \mathbf{I} + \nu_\beta \nabla \tilde{\mathbf{v}}_\beta \right) \, dA.$$

We remember that the last integral term will not be further developed since it vanishes in case of rigid porous media (assumption required further in the development).

2.4 Closure problems

2.4.1 Microscopic force $\mathbf{F}^m$

The term $\mathbf{F}^m$ acts as a surface filter in the momentum equation. The perturbation fields are filtered out by the integral operation over the fluid-solid interface. However, the term is usually called microscopic force since it physically represents the force per unit mass that the fluid exerts on the solid inclusions.

There is no simple representation for $\mathbf{F}^m$ if we include the terms that contain gradients of the porosity ($\nabla \varepsilon$). Since we are interested in developing a **local** closure problem, which will depend on the geometry of each REV, it is possible to neglect these terms. This means that the closure problems are not correct at the interface between a porous medium and a free fluid. However, if we use these closure problems at the interface we can still obtain good results, as shown in the last chapter, even if they are not formally correct.

The continuity equation in system (2.31) becomes $\nabla \cdot \langle \mathbf{v}_\beta \rangle^\beta = 0$ after the assumption of constant porosity. We subtract this last equation from the continuity equation valid for the local velocity velocity (2.1):

$$\nabla \cdot \mathbf{v}_\beta - \nabla \cdot \langle \mathbf{v}_\beta \rangle^\beta = 0.$$

From Gray's decomposition (2.23) the perturbation velocity field is written as $\tilde{\mathbf{v}}_\beta = \mathbf{v}_\beta - \langle \mathbf{v}_\beta \rangle^\beta$. Using this relation after collecting the divergence we obtain the continuity equation for the perturbations:

$$\nabla \cdot \tilde{\mathbf{v}}_\beta = 0. \tag{2.32}$$

To continue the development, we first divide the momentum equation of system (2.31) by the permeability ε, and we also apply the assumption of constant porosity:

$$\frac{\partial \langle \mathbf{v}_\beta \rangle^\beta}{\partial t} + \nabla \cdot \left(\langle \mathbf{v}_\beta \rangle^\beta \langle \mathbf{v}_\beta \rangle^\beta \right) + \frac{1}{\varepsilon} \nabla \cdot \left(\langle \tilde{\mathbf{v}}_\beta \tilde{\mathbf{v}}_\beta \rangle \right)$$

$$= -\nabla \left(\frac{\langle p_\beta \rangle^\beta}{\rho_\beta} \right) + \nu_\beta \nabla^2 \langle \mathbf{v}_\beta \rangle^\beta + \frac{1}{V_\beta} \int_{A_{\beta\sigma}} \mathbf{n}_{\beta\sigma} \cdot \left(-\frac{\tilde{p}_\beta}{\rho_\beta} \mathbf{I} + \nu_\beta \nabla \tilde{\mathbf{v}}_\beta \right) \, dA$$

Subtracting the above momentum equation from the local field one (2.1) it is found:

$$\frac{\partial \tilde{\mathbf{v}}_\beta}{\partial t} + \mathbf{v}_\beta \cdot \nabla \tilde{\mathbf{v}}_\beta + \tilde{\mathbf{v}}_\beta \cdot \nabla \langle \mathbf{v}_\beta \rangle^\beta + \varepsilon^{-1} \nabla \cdot \langle \tilde{\mathbf{v}}_\beta \tilde{\mathbf{v}}_\beta \rangle =$$

$$= -\nabla \left(\frac{\tilde{p}_\beta}{\rho_\beta} \right) + \nu_\beta \nabla^2 \tilde{\mathbf{v}}_\beta - \frac{1}{V_\beta} \int_{A_{\beta\sigma}} \mathbf{n}_{\beta\sigma} \cdot \left(-\frac{\tilde{p}_\beta}{\rho_\beta} \mathbf{I} + \nu_\beta \nabla \tilde{\mathbf{v}}_\beta \right) \, dA. \qquad (2.33)$$

Now in order to simplify this last equation the following length-scale estimates can be introduced:

$$\tilde{\mathbf{v}}_\beta = O(\langle \mathbf{v}_\beta \rangle^\beta), \qquad \nabla \tilde{\mathbf{v}}_\beta = O\left(\frac{\langle \mathbf{v}_\beta \rangle^\beta}{\ell} \right), \qquad \nabla \langle \mathbf{v}_\beta \rangle^\beta = O\left(\frac{\langle \mathbf{v}_\beta \rangle^\beta}{L} \right), \qquad \varepsilon = O(\delta).$$

The last relation state that the porosity varies over a length scale δ. Valdés-Parada et al. [153] and Ochoa-Tapia and Whitaker [118] propose the estimate $\ell \ll \delta$ arguing that δ has the size of the zone in which the porosity varies, in case of an interface between a porous medium and a free fluid. However it is important to state that this assumption does not holds at the interface of all porous media geometries. For ordered porous media $\varepsilon = O(\ell)$. Whitaker [161] states clearly that there is not any easy way to define a *local* closure problem when the relation $\ell \ll \delta$ does not hold. In order to continue with the development of the model, the relationship $\ell \ll \delta$ is assumed to be true. However, the derived closure problem will be formally correct only far from regions where the porosity varies.

Analyzing the orders of magnitude, it is possible to neglect some of the terms in the momentum equation (2.33):

$$\mathbf{v}_\beta \cdot \nabla \tilde{\mathbf{v}}_\beta \gg \tilde{\mathbf{v}}_\beta \cdot \nabla \langle \mathbf{v}_\beta \rangle^\beta \qquad \Rightarrow \qquad O\left(\frac{\langle \mathbf{v}_\beta \rangle^\beta}{\ell} \right) \gg O\left(\frac{\langle \mathbf{v}_\beta \rangle^\beta}{L} \right), \qquad (2.34)$$

$$\mathbf{v}_\beta \cdot \nabla \langle \tilde{\mathbf{v}}_\beta \rangle^\beta \gg \varepsilon^{-1} \nabla \cdot \left(\langle \tilde{\mathbf{v}}_\beta \tilde{\mathbf{v}}_\beta \rangle \right) \qquad \Rightarrow \qquad O\left(\frac{(\langle \mathbf{v}_\beta \rangle^\beta)^2}{\ell} \right) \gg O\left(\frac{(\langle \mathbf{v}_\beta \rangle^\beta)^2}{\delta} \right), \quad (2.35)$$

$$\nu_\beta \nabla^2 \tilde{\mathbf{v}}_\beta \gg \frac{\partial \tilde{\mathbf{v}}_\beta}{\partial t} \qquad \Rightarrow \qquad O\left(\frac{(\langle \mathbf{v}_\beta \rangle^\beta)^2}{\ell} \right) \gg O\left(\frac{(\langle \mathbf{v}_\beta \rangle^\beta)^2}{L} \right). \quad (2.36)$$

In the last assessment it has been assumed that the time scale associated respectively with the micro and the macro-scale are $t = \ell/\langle \mathbf{v}_\beta \rangle^\beta$ and $T = L/\langle \mathbf{v}_\beta \rangle^\beta$. These assumptions

imply that the perturbation problem is *quasi-stationary*, since physically the perturbation field can be considered steady from the macroscopic point of view (Davit et al. [44]; Zhu et al. [173]). It can also be noticed that in the above simplifications we have neglected terms that contains the small parameter ϵ or its powers. This last results is coherent with the multiple scale theory (Mei and Vernescu [108]) in which only zero order terms are kept in the local closure problem formulation.

With this order of magnitude analysis the governing equations are simplified as:

$$\begin{cases} \mathbf{v}_\beta \cdot \nabla \tilde{\mathbf{v}}_\beta = -\nabla \left(\dfrac{\tilde{p}_\beta}{\rho_\beta} \right) + \nu_\beta \nabla^2 \tilde{\mathbf{v}}_\beta - \dfrac{1}{V_\beta} \int_{A_{\beta\sigma}} \mathbf{n}_{\beta\sigma} \cdot \left(-\dfrac{\tilde{p}_\beta}{\rho_\beta} \mathbf{I} + \nu_\beta \nabla \tilde{\mathbf{v}}_\beta \right) \, dA, \\ \nabla \cdot \tilde{\mathbf{v}}_\beta = 0, \\ \tilde{\mathbf{v}}_\beta = -\langle \mathbf{v}_\beta \rangle^\beta \quad \text{at } A_{\beta\sigma}, \end{cases} \tag{2.37}$$

and these represent the transport equations for the perturbation fields.

Considering rigid porous media it is possible to derive the boundary conditions at the interface, substituting Gray's decomposition inside the boundary condition (2.1). As a consequence the solid phase is assumed rigid in this section. The above system is still defined on all the porous domain and so we would like to find a way to reduce its size and still obtain the same results. One possibility (not explored further here) is to use Green's functions to solve the problem in this form (Wood and Valdés-Parada [163]).

Here we proceed by restricting the solution region to a single REV, enforcing periodic boundary conditions at the boundaries of such a volume. Such hypothesis is consistent with the hypothesis of periodic ordered porous media in which the macroscopic field variation inside the REV are negligible[7]. The problem on the REV thus becomes:

$$\begin{cases} \mathbf{v}_\beta \cdot \nabla \tilde{\mathbf{v}}_\beta = -\nabla \left(\dfrac{\tilde{p}_\beta}{\rho_\beta} \right) + \nu_\beta \nabla^2 \tilde{\mathbf{v}}_\beta - \dfrac{1}{V_\beta} \int_{A_{\beta\sigma}} \mathbf{n}_{\beta\sigma} \cdot \left(-\dfrac{\tilde{p}_\beta}{\rho_\beta} \mathbf{I} + \nu_\beta \nabla \tilde{\mathbf{v}}_\beta \right) \, dA, \\ \nabla \cdot \tilde{\mathbf{v}}_\beta = 0, \\ \tilde{\mathbf{v}}_\beta = -\langle \mathbf{v}_\beta \rangle^\beta \quad \text{at } A_{\beta\sigma}, \\ \tilde{p}_\beta(\mathbf{x} + \boldsymbol{\ell}_i) = \tilde{p}_\beta(\mathbf{x}), \qquad \tilde{\mathbf{v}}_\beta(\mathbf{x} + \boldsymbol{\ell}_i) = \tilde{\mathbf{v}}_\beta(\mathbf{x}), \qquad i = 1, 2, 3, \\ \langle \tilde{\mathbf{v}}_\beta \rangle^\beta = 0. \end{cases} \tag{2.38}$$

In this set of equations the last condition, $\langle \tilde{\mathbf{v}}_\beta \rangle^\beta = 0$, is imposed to ensure a unique solution.

Now the perturbed field has to be expressed as a function of some averaged values. Let us introduce the closure tensor $\mathbf{S}$ and the closure vector $\mathbf{s}$ as:

$$\tilde{\mathbf{v}}_\beta = \mathbf{S} \cdot \langle \mathbf{v}_\beta \rangle^\beta(\mathbf{x}) + \boldsymbol{\xi} \tag{2.39}$$

$$\tilde{p}_\beta = \mu_\beta \mathbf{s} \cdot \langle \mathbf{v}_\beta \rangle^\beta(\mathbf{x}) + \gamma \tag{2.40}$$

---

[7]see paragraph 2.6.

49

where $\boldsymbol{\xi}$ is a vector and γ a scalar. Whitaker [161] has demonstrated that the first vanishes and the second is constant. It is very important to point out that equation (2.39) and (2.40) are crucial since a linear correlation between the micro and macro-scale fields is implied. However these relations can be function of the space coordinate $\mathbf{x}$ as explored later in chapter 4.

Whitaker [161] proposes to define $\mathbf{S}$ and $\mathbf{s}$ via the following problem:

$$
\begin{cases}
\dfrac{\mathbf{v}_\beta}{\nu_\beta} \cdot \nabla \mathbf{S} = -\nabla \mathbf{s} + \nabla^2 \mathbf{S} - \dfrac{1}{V_\beta} \displaystyle\int_{A_{\beta\sigma}} \mathbf{n}_{\beta\sigma} \cdot (-\mathbf{s}\mathbf{I} + \nabla \mathbf{S}) \ dA, \\
\nabla \cdot \mathbf{S} = 0, \\
\mathbf{S} = \mathbf{I} \quad \text{at } A_{\beta\sigma}, \\
\mathbf{s}(\mathbf{x} + \ell_i) = \mathbf{s}(\mathbf{x}), \qquad \mathbf{S}(\mathbf{x} + \ell_i) = \mathbf{S}(\mathbf{x}), \qquad i = 1, 2, 3, \\
\langle \mathbf{S} \rangle^\beta = 0.
\end{cases}
\tag{2.41}
$$

It is difficult to solve this problem computationally because it is an integral-differential equation. In order to simplify the problem, it is further decomposed into two parts, the solution of the first one gives us the *permeability tensor* and the solution of the second one the *Forchheimer tensor*. The variables $\mathbf{S}$ and $\mathbf{s}$ are further decomposed as:

$$\mathbf{S} = \mathbf{B} + \mathbf{C}, \qquad \mathbf{s} = \mathbf{b} + \mathbf{c}.$$

In this manner the micro-macro field relationship can be written as:

$$\tilde{\mathbf{v}}_\beta = \mathbf{B} \cdot \langle \mathbf{v}_\beta \rangle^\beta + \mathbf{C} \cdot \langle \mathbf{v}_\beta \rangle^\beta, \tag{2.42}$$

$$\tilde{p}_\beta = \mu_\beta \mathbf{b} \cdot \langle \mathbf{v}_\beta \rangle^\beta + \mu_\beta \mathbf{c} \cdot \langle \mathbf{v}_\beta \rangle^\beta, \tag{2.43}$$

where $\mathbf{B}$ is defined from:

$$
\begin{cases}
0 = -\nabla \mathbf{b} + \nabla^2 \mathbf{B} - \dfrac{1}{V_\beta} \displaystyle\int_{A_{\beta\sigma}} \mathbf{n}_{\beta\sigma} \cdot (-\mathbf{b}\mathbf{I} + \nabla \mathbf{B}) \ dA, \\
\nabla \cdot \mathbf{B} = 0, \\
\mathbf{B} = -\mathbf{I} \quad \text{at } A_{\beta\sigma}, \\
\mathbf{b}(\mathbf{x} + \ell_i) = \mathbf{b}(\mathbf{x}), \qquad \mathbf{B}(\mathbf{x} + \ell_i) = \mathbf{B}(\mathbf{x}), \qquad i = 1, 2, 3, \\
\langle \mathbf{B} \rangle^\beta = 0.
\end{cases}
\tag{2.44}
$$

and $\mathbf{C}$ from:

$$\begin{cases} \dfrac{\mathbf{v}_\beta}{\nu_\beta} \cdot \nabla \mathbf{B} + \dfrac{\mathbf{v}_\beta}{\nu_\beta} \cdot \nabla \mathbf{C} = -\nabla \mathbf{c} + \nabla^2 \mathbf{C} - \dfrac{1}{V_\beta} \displaystyle\int_{A_{\beta\sigma}} \mathbf{n}_{\beta\sigma} \cdot (-\mathbf{cI} + \nabla \mathbf{C}) \ dA, \\ \nabla \cdot \mathbf{C} = 0, \\ \mathbf{C} = 0 \quad \text{at } A_{\beta\sigma}, \\ \mathbf{c}(\mathbf{x} + \ell_i) = \mathbf{c}(\mathbf{x}), \qquad \mathbf{C}(\mathbf{x} + \ell_i) = \mathbf{C}(\mathbf{x}), \qquad i = 1, 2, 3, \\ \langle \mathbf{C} \rangle^\beta = 0. \end{cases} \tag{2.45}$$

Substituting the decomposition (2.39) and (2.40) inside the surface filter $\mathbf{F}^m$ we get:

$$\mathbf{F}^m = \nu_\beta \left(\dfrac{1}{V_\beta} \int_{A_{\beta\sigma}} \mathbf{n}_{\beta\sigma} \cdot (-\mathbf{sI} + \nabla \mathbf{S}) \ dA \right) \langle \mathbf{v}_\beta \rangle^\beta$$

Decomposing then the closure variables as in (2.42) it is possible to define the *permeability tensor* $\mathbf{K}$:

$$\dfrac{1}{V_\beta} \int_{A_{\beta\sigma}} \mathbf{n}_{\beta\sigma} \cdot (-\mathbf{bI} + \nabla \mathbf{B}) \ dA = -\varepsilon \mathbf{K}^{-1},$$

and the *Forchheimer tensor* $\mathbf{F}$:

$$\dfrac{1}{V_\beta} \int_{A_{\beta\sigma}} \mathbf{n}_{\beta\sigma} \cdot (-\mathbf{cI} + \nabla \mathbf{C}) \ dA = -\varepsilon \mathbf{K}^{-1} \cdot \mathbf{F}.$$

A change of variables is now made (Barrere et al. [10]):

$$\mathbf{d} = \varepsilon^{-1} \mathbf{b} \cdot \mathbf{K}, \qquad \mathbf{D} = \varepsilon^{-1} (\mathbf{B} + \mathbf{I}) \cdot \mathbf{K}, \tag{2.46}$$

$$\mathbf{m} = \varepsilon^{-1} \mathbf{c} \cdot \mathbf{H}, \qquad \mathbf{M} = \varepsilon^{-1} (\mathbf{C} + \mathbf{I}) \cdot \mathbf{H}, \tag{2.47}$$

problem (2.44) can be written as:

$$\begin{cases} 0 = -\nabla \mathbf{d} + \nabla^2 \mathbf{D} + \mathbf{I}, \\ \nabla \cdot \mathbf{D} = 0, \\ \langle d \rangle^\beta = 0, \\ \mathbf{D} = 0 \quad \text{at } A_{\beta\sigma}, \\ \mathbf{d}(\mathbf{x} + \ell_i) = \mathbf{d}(\mathbf{x}), \qquad \mathbf{D}(\mathbf{x} + \ell_i) = \mathbf{D}(\mathbf{x}), \qquad i = 1, 2, 3, \\ \langle \mathbf{D} \rangle^\beta = \varepsilon^{-1} \mathbf{K}, \end{cases} \tag{2.48}$$

the permeability tensor $\mathbf{K}$ can now be computed from $\mathbf{D}$.

Problem (2.45) with the change of variables (2.47) becomes:

$$
\begin{cases}
\dfrac{\mathbf{v}_\beta}{\nu_\beta}\nabla\mathbf{M} = -\nabla\mathbf{m} + \nabla^2\mathbf{M} + \mathbf{I}, \\
\nabla\cdot\mathbf{M} = 0, \\
\langle m\rangle^\beta = 0, \\
\mathbf{M} = 0 \quad at\ A_{\beta\sigma}, \\
\mathbf{m}(\mathbf{x}+\ell_i) = \mathbf{m}(\mathbf{x}), \qquad \mathbf{M}(\mathbf{x}+\ell_i) = \mathbf{M}(\mathbf{x}), \qquad i=1,2,3, \\
\langle\mathbf{M}\rangle^\beta = \varepsilon^{-1}\mathbf{H},
\end{cases}
\tag{2.49}
$$

where $\mathbf{H}$ is called *effective permeability tensor* and it represents a generalization of the permeability tensor in the inertia regime. The relation between the Forchheimer tensor and the effective permeability is the following:

$$
\mathbf{H}^{-1} = \mathbf{K}^{-1}\left(\mathbf{I}+\mathbf{F}\right).
$$

With the help of the above closure problem the final closed formulation for the microscopic force becomes:

$$
\mathbf{F}^m \approx \mathbf{F}^M = -\nu_\beta\varepsilon\mathbf{H}^{-1}\cdot\langle\mathbf{v}_\beta\rangle^\beta
\tag{2.50}
$$

in which the correspondence between the descriptions by means of the perturbation fields and the one that uses only the macroscopic fields become readily apparent.

It is also possible to use simplified regressions that permit to by-pass the *local* closure problems and get directly the tensors $\mathbf{K}$ and $\mathbf{F}$. One of the most famous relations are the Kozeny-Carman equation (Kozeny [87]) and the modified Ergun equation. An extended version of this empirical formulation can be found in Zampogna and Bottaro [167] and Yazdchi and Luding [164]. The above relationships are always based on regressions from experiments and they are usually parameterized with the porosity and some geometrical characteristics of the medium. The downsize in using these simplified formulas is that the geometries used are most of the times very simple such as spheres, or 2D regular arranged cylinders and they are difficult to generalize. Also their range of application is usually restricted to very small Reynolds number. Such restrictions render the local closure problems the most reliable means to compute the Forchheimer and permeability tensors.

2.4.2 Sub-filter stresses $\boldsymbol{\zeta}$

The model is not yet completed, also the *sub-filter stresses* need to be closed. This term acts as a volume filter for the perturbation velocity, in fact the product of the velocity perturbations appear inside the volume averaging operator:

$$
\boldsymbol{\zeta} = \nabla\cdot\langle\tilde{\mathbf{v}}_\beta\tilde{\mathbf{v}}_\beta\rangle.
$$

The same term has already been neglected in equation (2.35) in the previous paragraph, based on some length-scale argument [161]. Here we want to explain briefly what this term represents and possibly when it can become important.

Breugem et al. [24] and Nepf [116] separate the nature of sub-filter stresses into two different components:

- *mechanical diffusion:* when the fluid is forced to flow through the pores, it has to pass around the solid structure causing an increase of diffusion inside the VANS momentum equations. This mechanism is usually studied by means of the flow path tortuosity for each different particle (Duda et al. [47]; Sivanesapillai et al. [144]).

- *turbulent dispersion:* it is caused by the subfilter scales eddies that appear at the pore scale. This turbulent diffusivity can be anisotropic. For example, in the case of fibrous porous media the vertical penetration and breakdown of eddies is much higher than the horizontal one.

Breugem et al. [24] show that even if the two different components are equally important they are negligible in the volume averaged field equations.

However, we speculate that this term can becomes important in situations involving elastic porous media where sweeps and ejection of fluid can be observed at the interface. This statement is supported by Finnigan [55] and De Langre [45] who have shown the turbulence spectrum modification in the case of canopy flows. Possibly, the sub-filter stresses could model this shift of the spectrum to high frequencies.

In order to better study this term, we need many reliable full DNS inside the porous media at high pore Reynolds number. However, such simulations are very expensive and almost absent from the literature. Experimental measurements inside the porous structure can be another way to study this volume filter, even though such measurements can be very difficult to perform.

2.5   Interface treatment

The problem of the interface condition between a porous medium and a free fluid has been approached by many different authors. Ehrhardt [51] has given a concise but very clear introduction on the problem, even thought the field is rapidly evolving (Minale [111], Angot et al. [6], Lācis and Bagheri [89], Zampogna et al. [171]). Our work is not focused on the development of a new condition although, here, we want to explain our choice for the interface treatment over the many possible ones.

The interface conditions can be classified into two groups: the *one domain approach* (ODA) and the *two domain approach* (TDA). In the TDA the whole domain is split into two and a boundary condition at the interface is specified. Historically, the necessity of such a treatment was mainly due by the difference of order of the Stokes equations and the Darcy one, that makes them incompatible at the interface. The Brinkmann model

adjusts the order of the porous medium equation, however the validity of this correction deep inside the porous medium is questionable. The TDA was followed by Beavers and Joseph [14], Mikelic and Jäger [109], Ochoa-Tapia and Whitaker [118] and Le Bars and Worster [94]. These works have all in common the fact that a certain slip is specified at the interface, for example the Beavers and Joseph [14] condition reads:

$$\langle \mathbf{v}_\beta \rangle^\beta(x, \Gamma^+) = \frac{\sqrt{K_{11}}}{\alpha} \frac{\partial \langle \mathbf{v}_\beta \rangle^\beta(x, \Gamma^-)}{\partial y},$$

where Γ^+ and Γ^- represent the wall normal coordinate above and below the interface, K_{11} is a measure of the permeability component in the tangential direction and α is a coefficient based on the porous medium geometry. Other propositions change and extend this formulation but basically they still impose a velocity jump at the interface, as a function of a parameter α needed to fit the experimental data.

On the contrary in the ODA approach the final averaged equation are valid through the whole domain and the quantities that define the presence of the porous media, i.e. the porosity and the permeability, vanish in the free fluid region. This method is also know as *penalization method*. One of the first applications of the penalization method can be found in Caltagirone [31]; after that it was used by many other authors, like Bruneau and Mortazavi [27], Bruneau and Mortazavi [28], Bruneau et al. [29], Hussong et al. [77]. It is possible that the interface boundary condition approach is not superior, neither physically nor mathematically. As a matter of fact either methods require a parameter to close the formulation. The advantage of using the penalization method is that in this case the parameter needed is the spatial distribution of the porosity field that is trivial to compute when the geometry of the medium is known. However, it is still not clear how to vary the permeability in the transition zone. Most of the authors propose a sharp jump from the porous media value and the free fluid one. Neglecting the variation of permeability across the transition zone appears to be acceptable, even though examples of linear variation of this term exists (Caltagirone [31]). Hussong et al. [77] make a direct comparison with a DNS simulation which included a discretization of all the pores, and concluded that the variation of the permeability is very important in order to have a good comparison with high fidelity computation.

A direct comparison between the ODA and TDA is presented in Cimolin and Discacciati [40] who conclude that the macroscopic description of the interface provided by the two different methods is similar. They also point out that the penalization method has the advantage to be easily implemented in a Navier-Stokes solver and it does not present sensitive convergence properties as the TDA do.

Also, there is evidence in the literature (Ochoa-Tapia et al. [119]) that transition zone of the size of the pore scale exist, in which the velocity and pressure exhibit a continuous variation and not a steep one. It has been demonstrated by the same authors that the same transition zone is physical and not a result of the averaging procedure.

In the following work we adopt the penalization approach with the porosity variation computed directly from the geometry of our fibrous medium and a steep variation of the effective permeability at the interface. In chapter 5 we show some details and results from this approach.

2.6 Note on the average of an average field

In the above sections we have briefly talked about the results in equation (2.6) that we recall here:

$$\left\langle \langle \psi_\beta \rangle |_\mathbf{r} \right\rangle |_\mathbf{x} = \langle \psi_\beta \rangle |_\mathbf{x}.$$

Introducing the decomposition (2.23) the above results can be used to state that the perturbation fields have zero average:

$$\left\langle \tilde{\psi}_\beta \right\rangle = 0.$$

Let us recall what the average operator really does when applied to an averaged quantities:

$$\left\langle \langle \psi_\beta \rangle |_\mathbf{r} \right\rangle |_\mathbf{x} = \frac{1}{V} \int_{V_\beta(\mathbf{x})} \langle \psi_\beta \rangle |_\mathbf{r}(\mathbf{r}) \, dV;$$

the above equation can be described as the average computed over the volume V with centroid $\mathbf{x}$, of the averaged field $\langle \psi_\beta \rangle |_\mathbf{r}$ that can vary spatially, because of the change of $\mathbf{r}$.

In order to show how the above expression can be simplified we expand the averaged quantity $\langle \psi_\beta \rangle |_\mathbf{r}$ over the centroid $\mathbf{x}$ using a Taylor expansion:

$$\langle \psi_\beta \rangle |_\mathbf{r} = \langle \psi_\beta \rangle |_\mathbf{x} + \mathbf{y} \cdot \nabla \langle \psi_\beta \rangle |_\mathbf{x} + \frac{1}{2} \mathbf{y}\mathbf{y} : \nabla\nabla \langle \psi_\beta \rangle |_\mathbf{x} + O(\mathbf{y}^3)$$

Now, if we put this expansion inside the averaging operator, we get:

$$\left\langle \langle \psi_\beta \rangle |_\mathbf{r} \right\rangle |_\mathbf{x} = \langle \psi_\beta \rangle |_\mathbf{x} + \langle \mathbf{y} \rangle |_\mathbf{x} \cdot \nabla \langle \psi_\beta \rangle |_\mathbf{x} + \frac{1}{2} \langle \mathbf{y}\mathbf{y} \rangle |_\mathbf{x} : \nabla\nabla \langle \psi_\beta \rangle |_\mathbf{x} + O(\mathbf{y}^3)$$

The term $\langle \mathbf{y} \rangle$ is zero for REVs used in ordered porous media. The second term can be shown to be negligible either with the same length-scale constraint used in the REV definition, in fact Ochoa-Tapia and Whitaker [118], Paéz-García et al. [122] showed that this term is order $O(\epsilon^2)$. Although it is possible to choose an appropriate weight function that strictly enforces $m * \mathbf{y}\mathbf{y} = 0$, these function are unpractical (Davit and Quintard [43]). As we recall from section 2.3.3 the triangle shaped weight function almost satisfies this hypothesis. The function $m^\triangle$ guarantees a second order closure. This means that $\frac{1}{2} \langle \mathbf{y}\mathbf{y} \rangle |_\mathbf{x} : \nabla\nabla \langle \psi_\beta \rangle |_\mathbf{x}$ is a constant. Further manipulations ([43]) can show that it is also negligible ($O(\epsilon^2)$).

2.7 Conclusions

We have shown in this chapter how to formally derive the homogenized version of the Navier-Stokes equations. We have also discussed the extension of the model in case of an elastic porous medium. A lot of emphasis has been put on the closure problem for the microscopic force and the topic is further developed in chapter 4. Although the average volume method is not new, we think that this chapter helps to place in context the recent works in the literature. The chapter also forms a basis for a better understanding of the next chapters.

Chapter 3

Drag-model sensitivity of Kelvin-Helmholtz waves in canopy flows

While knowledge can create problems, it is not through ignorance that we can solve them.

- Asimov's New Guide to Science, 1984, *Isaac Asimov*

3.1 Introduction

In section 1.5 of the introduction we have already introduced the stability problems for flow through porous media. In the same text some results has already been discussed and it has been enlightened that most of the modelling problem rely on the choice of the drag model that include the canopy effects inside the flow.

Questions remain, however, on which is the most accurate and/or less sensible model for the canopy drag. Most of the authors (Raupach et al. [134], Py et al. [127] and Singh et al. [143]) uses a drag coefficient based source term, inside the momentum equation, that mimic the presence on the canopy. Instead in the work of Zampogna et al. [170] a different model, applicable within the vegetated layer and based on the equations ruling the behavior of a transversely isotropic porous medium, has been developed and the stability results appear to better match experimental correlations. This conclusion is, however, not consolidated yet, and further studies are needed to assess the influence of the model of the drag force through the vegetation, both in setting up a particular (inflectional) mean flow and on the onset and growth of Kelvin-Helmholtz waves. The present work addresses the points above through an adjoint based sensitivity analysis along the lines of Bottaro et al. [21] the direct stability equations are written with account of viscosity, and the adjoint

equations are found and solved in the temporal framework. Results in the spatial setting are discussed in section 3.5, where a digression is made on the computation of the group velocity of the instability waves by the use of the adjoint fields. The sensitivity functions to both mild modifications in the base shear layer and in the drag coefficient are computed and discussed. Finally, a different sensitivity analysis is developed on the basis of the recent anisotropic model by Zampogna et al. [170] and the results qualitatively compared to those obtained with the more conventional isotropic drag force model.

3.2 Model of the canopy flow

3.2.1 The mean flow

To obtain the mean flow on top of which small amplitude perturbations are superimposed, the procedure outlined by Ghisalberti and Nepf [65] and recently closely followed by Zampogna et al. [170] is used. For the sake of conciseness, the procedure which relies on several empirical correlations is not repeated here, aside from a few brief comments. A mildly inclined water channel is considered, with a canopy formed by rigid cylindrical dowels of height h equal to $13.8\,cm$ and diameter $d = 0.64cm$. The frontal area of the vegetation per unit volume, i.e., the packing density of the elements, is either $a = 0.04cm^{-1}$ or $0.08cm^{-1}$; the free surface is positioned at a level $H = 46.7cm$ from the bottom plate and the flow velocity at the free surface, U_2 , varies from 4.4 to $13.7cm/s$. The Froude number, $F_r = \dfrac{U_2}{gH}$ is thus very low and water surface fluctuations can be ignored (Brevis et al. [25]). To a good approximation the mean flow can be taken as steady and parallel, with the streamwise velocity varying from the value U_1 at the bottom wall (not accounting for the thin bottom boundary layer) to the value U_2 at the top, near the free surface (3.1). The slope of the bottom surface is very small; it is denoted as S and, in the experiments by Ghisalberti and Nepf [65] varies from 1.8×10^{-6} to 10^{-4}; such a slope provides the driving force for the motion. The viscous term is small compared to the turbulent diffusion term, so that the mean streamwise momentum equation can be approximated by:

$$gS = \frac{\partial \overline{u'v'}}{\partial y} + \frac{1}{2}C_D(y)aU(y)^2 \tag{3.1}$$

with g the acceleration of gravity and C_D an isotropic drag function available from the experiments, variable across the canopy and equal to zero when $y \geq h$.

The Reynolds stress $\overline{u'v'}$ is modelled with the Boussinesq assumption, introducing a turbulent viscosity which depends on a mixing length and on the gradient of the mean velocity U. Referring to Ghisalberti and Nepf [65] for details of the empirical correlations used to close the equations and the solution method, we limit ourselves here to stating that the results obtained for the mean flow are very close to those reported in Zampogna et al. [170] (cf. their Figure 3) and closely match experimental points for the cases G, H,
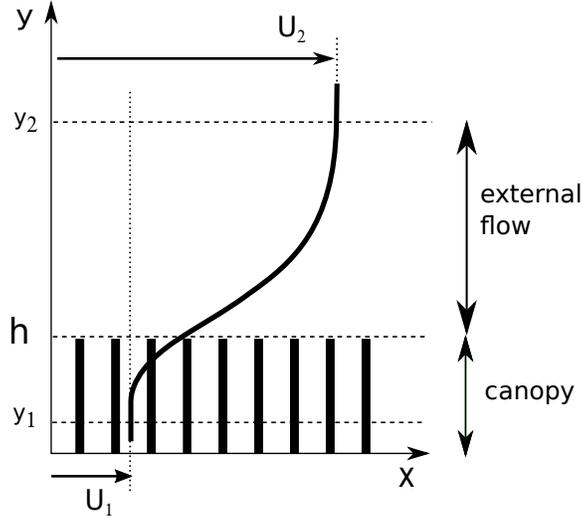
Figure 3.1: Configuration studied with main notations

I, and J considered (we use the same terminology of Ghisalberti and Nepf [64] [65] [66] to indicate the different flow configurations). An example of mean flow is reported in 3.2 (left frame). There, one can observe the computed flow (against discrete measurement points), its first derivative, and the drag coefficient distribution for one representative case (experiment G), used below also to discuss stability and sensitivity results. Other procedures have been employed in the past to calculate the mean flow, with satisfactory results. For example, Singh et al. [143] have considered a constant value of C_D through the canopy, while Zampogna et al. [170] have coupled, at a fictitious interface, the fluid equations outside the canopy to Darcy's law within the vegetation. Thus, for the purposes of the present paper, the mean flow is assumed as given; it could be, for example, simply a fit through experimental data.

3.2.2 Stability and sensitivity equations

A temporal linear stability analysis is carried out, with the generic perturbation $q'(x, y, t)$ of the form:

$$q'(x, y, t) = \tilde{q}(y)\mathrm{e}^{i(\alpha\ x - \omega\ t)} \tag{3.2}$$

with α the real streamwise wavenumber and ω a complex number whose real part, ω_r, is the frequency of the mode and the imaginary part, ω_i , is the growth rate.

The dimensionless linear stability equations in primitive variables read:

$$i\alpha u + Dv = 0, \qquad D = d/dy$$

$$\left[i(\alpha U - \omega) - \frac{D^2 - \alpha^2}{Re} + aC_d U \right] u + U'v + i\alpha p = 0, \qquad U' = \frac{dU}{dy} \qquad (3.3)$$

$$\left[i(\alpha U - \omega) - \frac{D^2 - \alpha^2}{Re} \right] v + Dp = 0$$

with the perturbation velocity components which vanishes when $y = 0$ and $y = y_\infty$. The upper boundary of the computational domain is taken far enough away from the lower boundary to ensure that the results do not vary upon modifications of y_∞. All the terms in the equations are dimensionless; the mean speed through the shear layer, $U_m = \dfrac{U_1 + U_2}{2}$, is used to scale the disturbance velocity components, pressure is scaled with ρU_m^2, distances with h, and time with h/U_m. The Reynolds number in the equations above is thus defined as $Re = \rho U_m h / \mu$, with ρ and μ the fluid's density and dynamic viscosity, respectively. The computations are performed both at the Re values of the experiments and in the inviscid limit ($Re^{-1} \to 0$), for comparison purposes. In the latter case, the boundary conditions are simply $v = 0$ at $y = 0$ and y_∞. System (3.3) above and its boundary conditions are, in the following, also written in short notation as $\mathscr{L}q = 0$. The eigenvalues of the system are those complex values of ω which yield non trivial solutions for u, v, and p. Two numerical collocation codes are written, and successfully compared; one is based on the equations in primitive variables form, the second solves an Orr-Sommerfeld like equation (with the addition of the drag term) along the lines of Singh et al. [143]. In both cases, a spectral scheme based on N Chebyshev polynomials is used (N is typically equal to 300 to ensure grid converged results), with an algebraic mapping between the physical and the spectral domains (Hussaini and Zang [76]).

Viscous and inviscid stability results for case G are shown in figure 3.2 (center and right frames); differences are small, in consideration of the fact that the Reynolds number of the viscous case is relatively large ($Re = 3450$). The viscous wavenumber of largest amplification is found for $\alpha = 0.4790$; the waves are weakly dispersive, particularly at low wavenumbers (an original interpretation of phase and group velocities is proposed in section 3.5). The wavelength of largest growth is smaller than that found by Zampogna et al. [170] which was 0.73; this is related to the slightly different base flow in the two cases (in the present contribution a smoothing has been applied to the U velocity distribution to render dU/dy continuous across y) and highlights the sensitivity of this stability problem to base flow variations. Following Bottaro et al. [21] it is assumed that small variations in base flow and drag coefficient entail infinitesimal variations in the system's eigenvalues and eigenfunctions. We stress here the fact that C_D is identically equal to zero outside of the canopy, and this implies that there are no possible variations in C_D for $y \geq 1$.
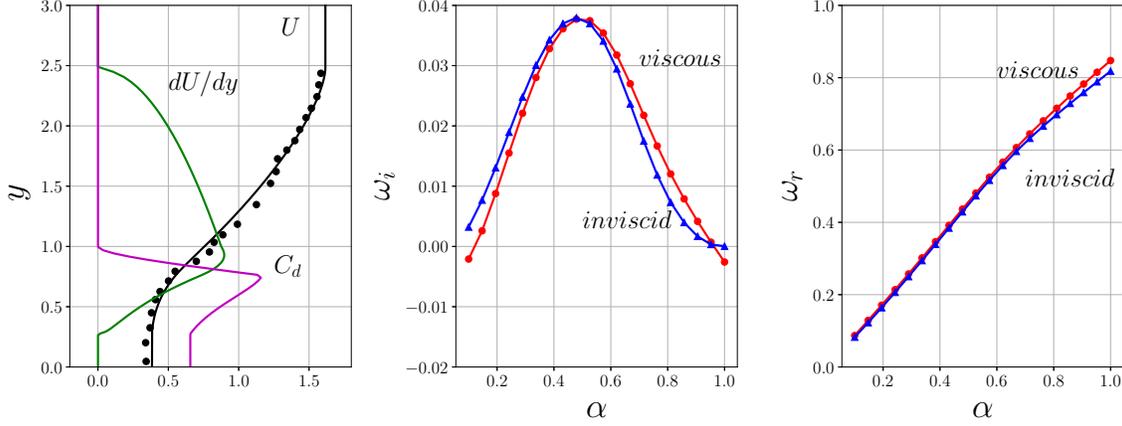
Figure 3.2: Left frame: mean flow U , together with experimental data points Ghisalberti and Nepf [65], its first derivative, and drag coefficient distribution (case G). Center: viscous and inviscid growth rates, ω_i , as a function of the streamwise wavenumber α. Right: corresponding frequencies, ω_r

The sensitivity functions to variations in U and C_D are obtained by using the properties of the adjoint system which is defined from the Lagrange identity:

$$0 = \delta\langle q^\dagger, \mathscr{L}q \rangle = \langle q^\dagger, \mathscr{L}\delta q \rangle + \langle q^\dagger, \frac{\partial\mathscr{L}}{\partial U}q\delta U \rangle + \langle q^\dagger, \frac{\partial\mathscr{L}}{\partial C_d}q\delta C_d \rangle + \langle q^\dagger, \frac{\partial\mathscr{L}}{\partial \omega}q \rangle\delta\omega \qquad (3.4)$$

and considering the effect of independent variations of U and C_D onto q and ω. It is found that:

$$\delta\omega = \delta\omega_r + i\delta\omega_i = \int_0^{y_\infty} G_U(y)\delta U(y)dy + \int_0^1 G_{C_D}(y)\delta C_D(y)dy \qquad (3.5)$$

with:

$$
\begin{aligned}
G_U &= \alpha\left[\overline{v^\dagger v} + \overline{u^\dagger u}\right] + i(\overline{u^\dagger v})' - ia C_d\overline{u^\dagger u} \\
G_{C_D} &= -i\alpha U\overline{u^\dagger u}
\end{aligned}
\qquad (3.6)
$$

the required sensitivity functions; the real parts of G_U and G_{C_d} express sensitivities to variations in the frequency of the mode while the imaginary parts are sensitivities to variations in the growth rate. Direct and adjoint eigenfunctions are normalized so that $N_\omega = 1$, with:

$$N_\omega = \int_0^{y_\infty} \left[\overline{v^\dagger v} + \overline{u^\dagger u}\right] dy \qquad (3.7)$$

61
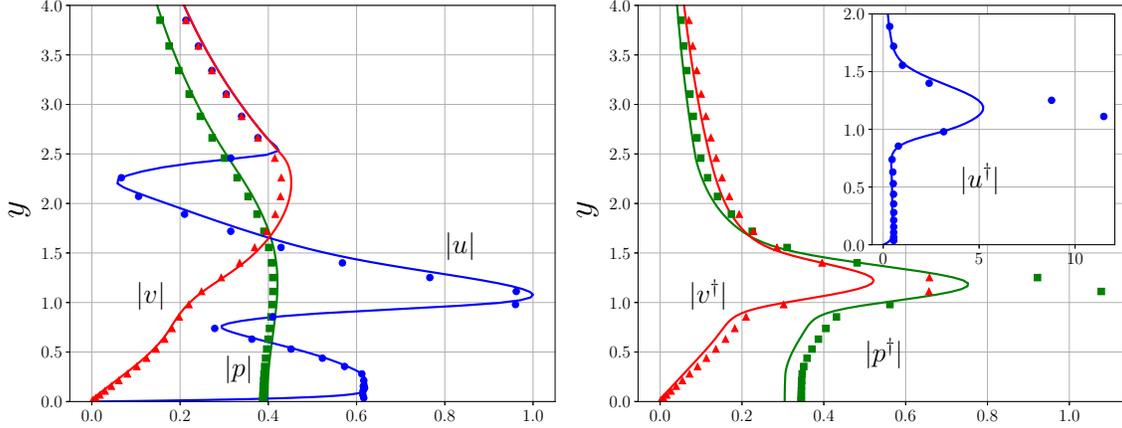
Figure 3.3: Moduli of direct (left frame) and adjoint (right frame) eigenfunctions for the viscous (continuous lines, $Re = 3450$) and the inviscid (symbols) case, in correspondence to the wavenumber of largest amplification.

An example of direct and adjoint eigenfunctions is provided in figure 3.3, both in the viscous case ($Re = 3450$) and in the inviscid limit, for $\alpha = 0.4790$. It is interesting to observe that while the direct eigenfunctions are almost overlapped, the same is not the case for the adjoint eigenfunctions, with the inviscid mode (drawn with symbols) which has a larger amplitude than the viscous one. The shapes of the direct eigenfunctions are very close to those reported in Zampogna et al. [170]. The adjoint modes reveal that the flow is most sensitive to streamwise forcing, particularly when it occurs slightly above the edge of the canopy. Source terms in the mass conservation and in the vertical momentum equations are much less effective.

3.3   Sensitivity results for the isotropic drag model

Some representative sensitivity functions are plotted in figure 3.4; viscous and inviscid results concur in showing that the largest sensitivities to variations of U are found right above the vegetation's edge, where there are peaks in the adjoint eigenfunctions and where d^2U/dy^2 vanishes. The U sensitivities are negligible within the vegetated layer and for values of y larger than twice the canopy's height. The C_D sensitivities are non negligible only in close proximity of the interface. It is interesting to observe that real and imaginary parts of the U sensitivity functions are shifted in y with respect to one another; this means that, for example, a localized perturbation at a given y position (above the canopy) might have a strong repercussion on the growth rate but not on the frequency of the most unstable Kelvin-Helmholtz mode, or vice versa. Comparing left and right frames of the figure 3.4, it is seen that inviscid G_U sensitivity functions display sharper peaks and steeper gradients,

62
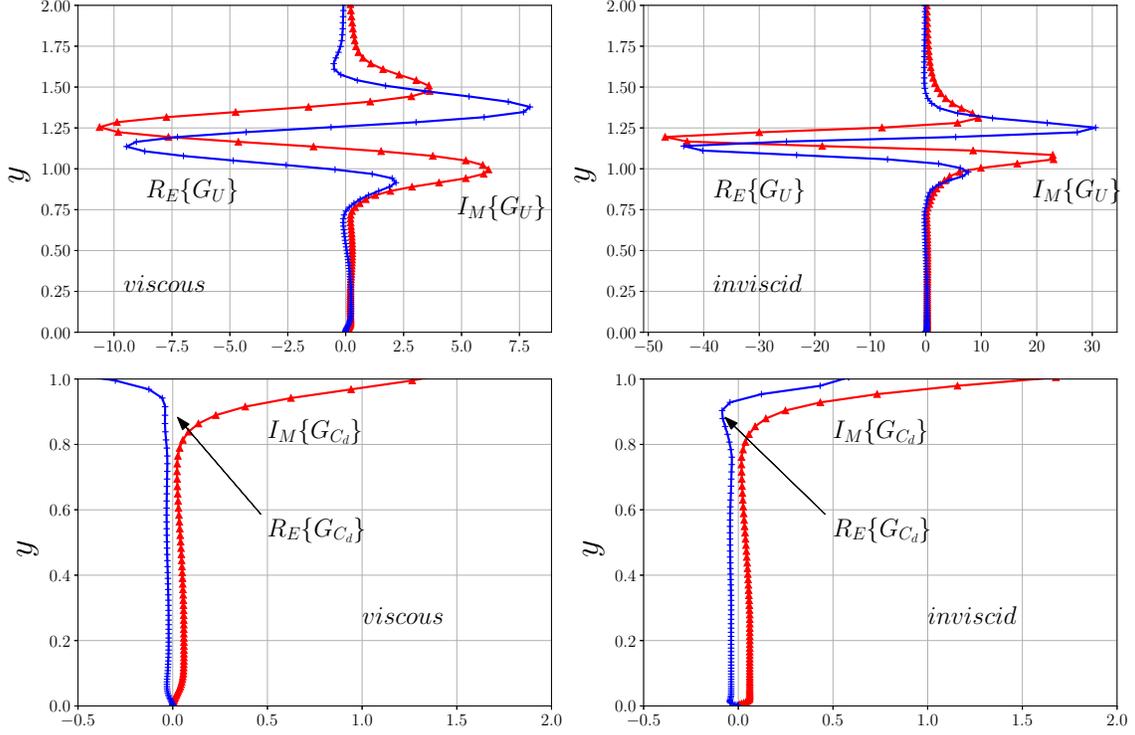
Figure 3.4: Real and imaginary parts of the sensitivities to mean flow variations (top) and to variations in the drag distribution function (bottom), for the parameters of 3.3

and yield larger variations in ω than their viscous counterparts in the proximity of the U inflection point, a clear consequence of the inviscid mechanism ruling the instability. In both the viscous and the inviscid models, the sensitivity to base flow variations is typically one order of magnitude larger than the sensitivity to changes in the drag coefficient.

The infinite norm of the sensitivities for the four cases studied (G, H, I, and J) is reported in 3.5; the main result found is that $|G_U|_\infty$ grows monotonically with α (and more so in the inviscid case) whereas $|G_{C_d}|_\infty$ does not. It is consistently found that $|G_U|_\infty$ of case H is larger than that of case I, which exceeds the corresponding value of case J, in turn larger than $|G_U|_\infty$ of case G. This is not unexpected in view of the values of the mean shear $\dfrac{U_2 - U_1}{H}$ which are, going from H to G, equal to 0.236, 0.158, 0.084, and $0.071s^{-1}$, respectively. The sensitivity of the eigenvalue ω to variations in the mean flow is generally stronger than the corresponding sensitivity to variations in the drag coefficient (aside for the long wave limit, where they are comparable). This might be interpreted positively, considering that the use of a scalar coefficient C_D to represent the drag within the canopy is but a crude approximation.
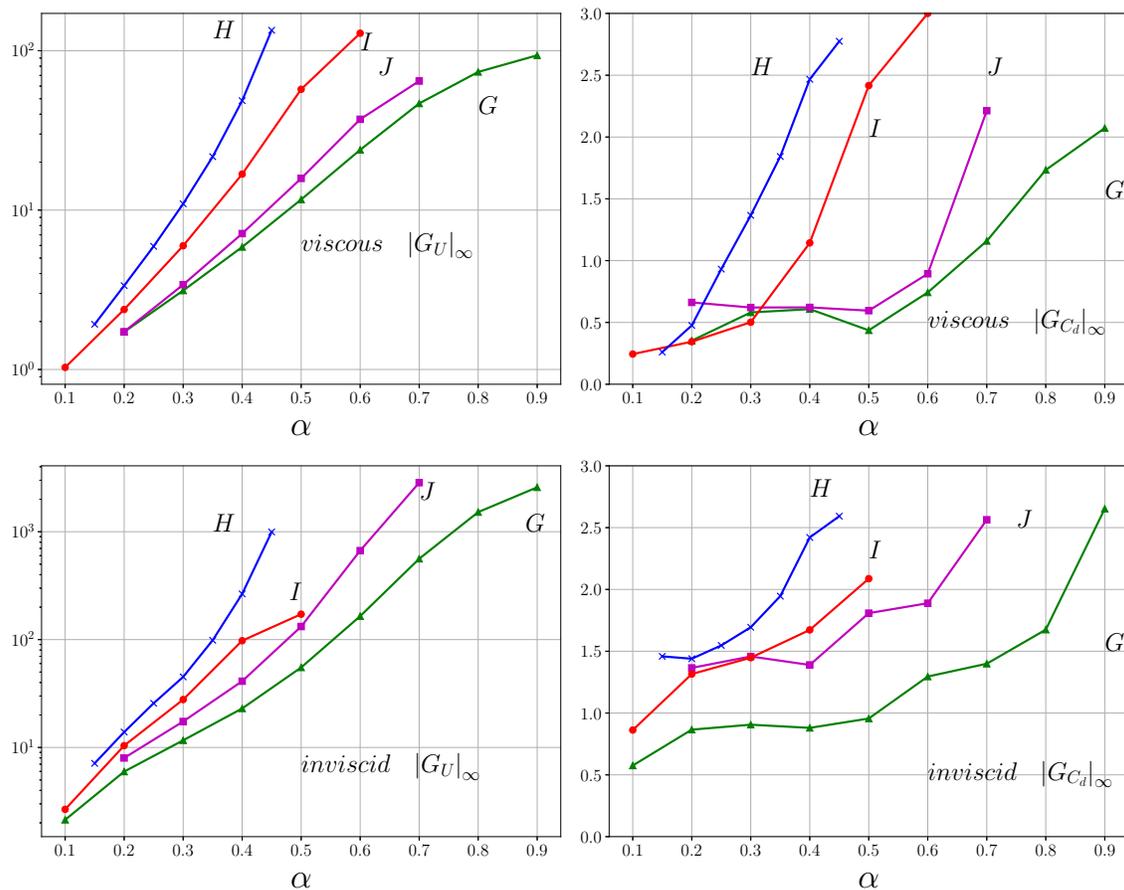
Figure 3.5: Infinite norms of the sensitivity functions for varying α

An alternative model to represent the flow throughout a network of rigid, cylindrical dowels has recently been proposed by Zampogna et al. [170] The sensitivity results for such a new model are discussed next.

3.4   An alternative sensitivity model: accounting for the canopy anisotropy

The stability problem in this section is based on the coupling between two regions, one outer region dominated by inertia and ruled by the inviscid equations and an inner one dominated by viscosity and ruled by Darcy's law, with account of the canopy geometry through a tensorial permeability, as described by Zampogna et al. [170].

Normalizing the disturbance equation which couples pressure and velocity in the inner region with the same scales as previously, we obtain

$$u_i{}' = -Re\frac{d}{ah^2}H_{ij}\frac{\partial p'}{\partial x_j}, \qquad (x_1, x_2) = (x, y) \tag{3.8}$$

with H_{ij} the dimensionless apparent (or effective) permeability. The effective interface between the inertial region and the slow, viscosity dominated region does not coincide with the edge of the canopy; in fact, the rapid outer flow penetrates through the upper part of the vegetation and an effective matching between outer and inner flows must be enforced some distance δ below the canopy's edge (Le Bars and Worster [94]). This distance, a penetration depth, has been successfully computed by Zampogna and Bottaro [167] for a few cases and is found to increase with the Reynolds number of the flow; for experiment G discussed below it is $\delta = 0.40$ (Zampogna and Bottaro [168]). On account of the results shown in figure 3.4, with the sensitivities which are negligible for $y \approx 0.60$, we expect that the exact position of the effective interface will not affect the results significantly. Using the fact that the velocity within the orthotropic porous medium is divergence free, the interface condition to be applied at $y_{itf} = 1 - \delta$ is found to be (3.9)

$$v|_{itf} + B(\alpha)p|_{itf} = 0 \tag{3.9}$$

with:

$$B(\alpha) = Re\frac{d}{ah^2}\sqrt{H_{11}H_{22}}\alpha\tanh(\theta), \qquad \theta = \alpha\sqrt{\frac{H_{11}}{H_{22}}}y_{itf}$$

The second boundary condition that the Rayleigh stability equation must satisfy at y_∞ is simply $v = 0$. Thus, we solve only for the inviscid flow in the outer region, and the permeability of the inner domain enters the equations only through the interface condition (3.9). H_{ij} is a two by two diagonal tensor; H_{11} is the component of the dimensionless permeability along x and H_{22} is the y component. For case G considered here, the packing density of the elements is $a = 0.04cm^{-1}$; it is also found that $H_{11} = 0.0512$ and $H_{22} = 0.0575$ (Zampogna and Bottaro [168]), so that the function $B(\alpha)$ reads $B = 15.727\alpha\tanh(0.566\alpha)$.

3.4.1 The sensitivity equations

The adjoint equations in this case are the same as system (3.3), without the terms containing $1/Re$ and C_D , and the boundary conditions are:

$$v^\dagger|_{itf} - B(\alpha)p^\dagger|_{itf} = 0, \qquad v^\dagger|_{y_\infty} = 0 \tag{3.10}$$

The variation in the complex frequency is related to variations in the mean flow and in the permeability components through the equation:

$$\delta\omega = \int_{y_{itf}}^{y_\infty} G_U(y)\delta U(y)dy + G_{H_{11}}\delta H_{11} + G_{H_{22}}\delta H_{22}$$

with:

$$G_U = \alpha\left[\overline{v^\dagger v} + \overline{u^\dagger u}\right] + i(\overline{u^\dagger v})'$$

$$G_{H_{11}} = -\frac{i}{2}\alpha Re\frac{d}{ah^2}\left[\overline{p^\dagger p}\right]|_{itf}\sqrt{\frac{H_{22}}{H_{11}}}\left\{\tanh\theta + \frac{\theta}{\cosh^2\theta}\right\} \tag{3.11}$$

$$G_{H_{22}} = -\frac{i}{2}\alpha Re\frac{d}{ah^2}\left[\overline{p^\dagger p}\right]|_{itf}\sqrt{\frac{H_{11}}{H_{22}}}\left\{\tanh\theta - \frac{\theta}{\cosh^2\theta}\right\}$$

the required sensitivities, with the normalization $\int_{y_{itf}}^{y_\infty}\left[\overline{v^\dagger v} + \overline{u^\dagger u}\right] = 1$. In writing $\delta\omega$ above, we have made the assumption that the mean flow U does not vary at the two extreme points of the integration domain. The stability results (for the same parameters as in figure 3.2) are displayed in figure 3.6.

As already observed in Zampogna et al. [170], both the growth rate and the frequency are slightly larger with this model than with the isotropic resistance model, for all α's, and the most unstable mode is found at a larger value of α (here $\alpha \approx 0.8$) in better agreement with experimental correlations Zampogna et al. [170] Raupach et al. [134]. Also in this case the waves are found to be only weakly dispersive.
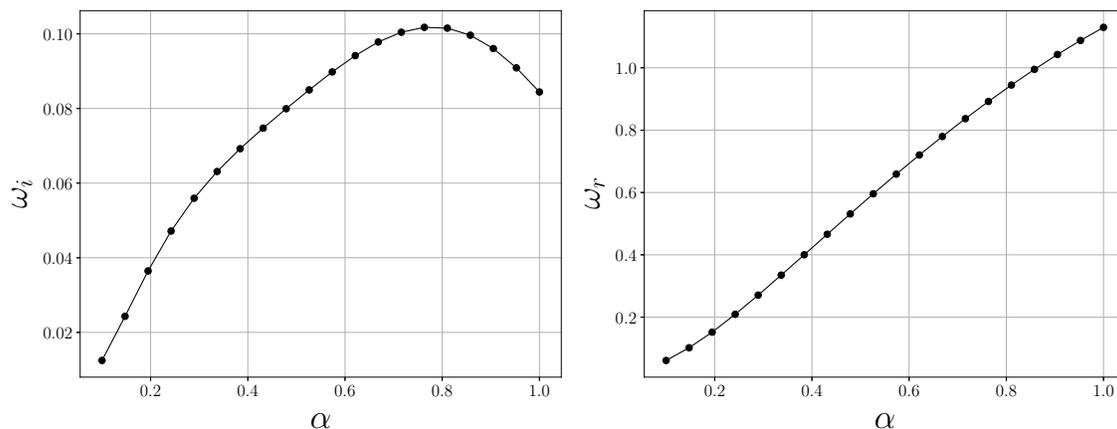
Figure 3.6: Amplification factor (left) and frequency of the most unstable mode as a function of α, for the anisotropic drag model
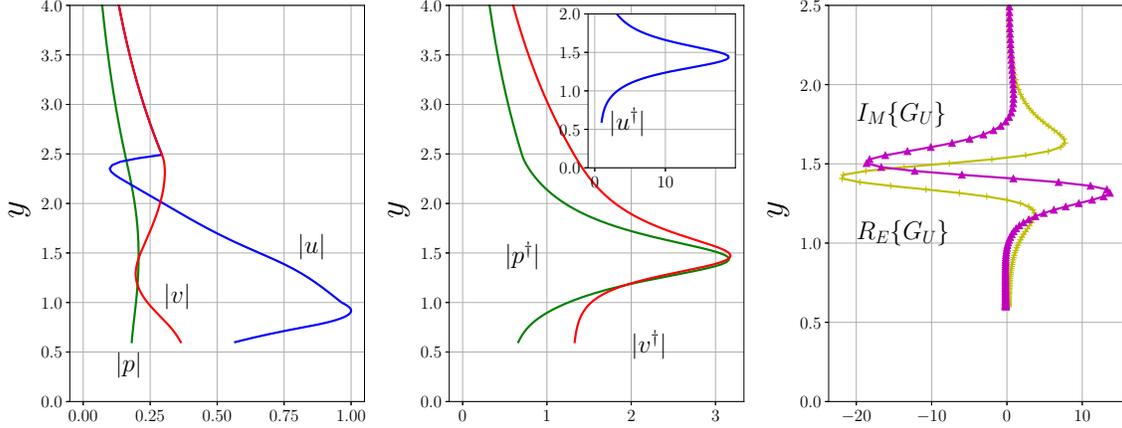
Figure 3.7: Left and center frames: moduli of direct and adjoint eigenfunctions; pressure and "adjoint pressure" are drawn with dashed lines. Right: real and imaginary parts of the sensitivity function G_U ($\alpha = 0.4790$)

Eigenfunctions are plotted in figure 3.7, together with the real and imaginary parts of the G_U sensitivity function. As in figure 3.3, the modulus of the u eigenfunction peaks near the edge of the canopy ($y = 1$), whereas the adjoint eigenfunctions have a maximum value slightly above. As a general remark, the shapes of the direct and adjoint modes are quite similar to those found with the isotropic resistance model; as reported at the end of 3.2.2, it is found that the flow is most sensitive to streamwise momentum forcing. Also, real and imaginary parts of G_U have a double peak structure, like in the isotropic drag model, but now the largest absolute value of G_U is smaller and shifted towards a larger y than in the previous inviscid case (cf.3.4, top right frame).

This can also be appreciated by the inspection of figure 3.8 (left); $|GU|_\infty$ still grows monotonically with α, but the sensitivity is smaller than that computed earlier (cf. 3.5) with either the viscous or inviscid model (it is actually closer to the viscous sensitivity, as an effect of the interface condition). Furthermore, it is interesting to observe that both real and imaginary parts of G_U vanish for $y = y|_{itf}$ (cf. figure 3.7, right), and this supports the statement made previously that a small shift in the position of the effective interface has but a minor influence on the most unstable mode. The sensitivity coefficients for the two components of the permeability tensors are displayed in figure 3.8 (center and right frames): the present model is more effective to variations in H_{11} than to H_{22} as far as modifying the complex eigenfrequency. Significantly, different ranges of wavenumbers behave differently as far as the variation in ω is concerned. The frequency ω_r of long waves (around $\alpha \approx 0.3$) is more easily modified by acting on H_{11} (with an almost negligible effect on the growth rate of the wave); conversely, the growth rate of modes with large values of α is affected efficiently by variations in the first component of the permeability tensor.

67
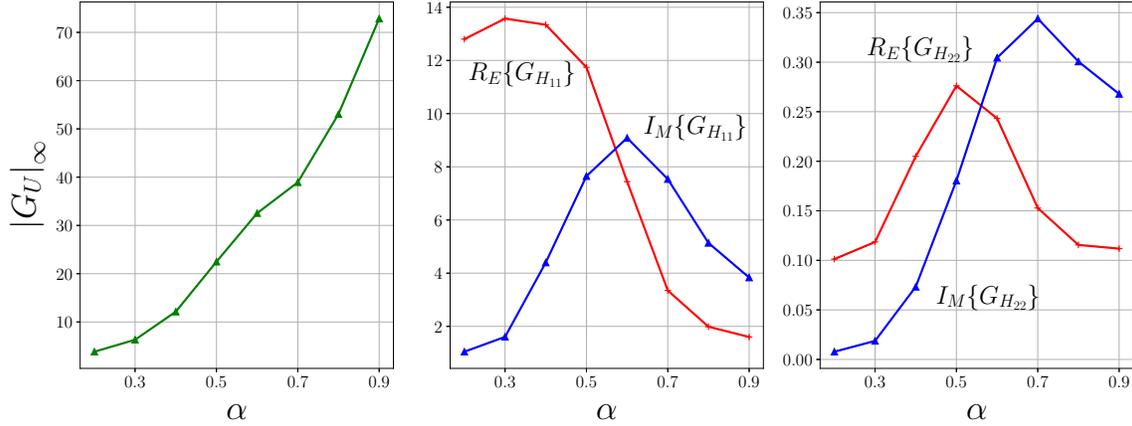
Figure 3.8: Case G. Left: infinite norm of G_U for varying α. Center and right frames: real and imaginary parts of the sensitivity coefficients to variations in the permeability components

3.5   Digression on spatial stability theory and group velocity

Stability problems such as the first one considered here can be approached with the spatial theory framework, with the wavenumber α complex, its imaginary part being a growth rate, and the circular frequency ω a real constant parameter. Let us generalize the sensitivity analysis by considering, as a first step, α and ω as complex numbers which can vary. Equation (3.4) contains one additional term and reads:

$$0 = \delta\langle q^\dagger, \mathscr{L}q\rangle = \langle q^\dagger, \mathscr{L}\delta q\rangle + \langle q^\dagger, \frac{\partial \mathscr{L}}{\partial U}q\delta U\rangle + \langle q^\dagger, \frac{\partial \mathscr{L}}{\partial C_d}q\delta C_d\rangle + \langle q^\dagger, \frac{\partial \mathscr{L}}{\partial \omega}q\rangle\delta\omega + \langle q^\dagger, \frac{\partial \mathscr{L}}{\partial \alpha}q\rangle\delta\alpha$$

(3.12)

To obtain the sensitivities in the spatial problem (for which $\delta\omega = 0$) we now have to solve an adjoint system similar to equation (3.3), where $\omega^\dagger$ is replaced by ω and α by $\alpha^\dagger$. The variation of the wavenumber $\delta\alpha = 0$ is thus given by:

$$\delta\alpha = \delta\alpha_r + i\delta\alpha_i = \int_0^{y_\infty} G_U(y)\delta U(y)dy + \int_0^1 G_{C_D}(y)\delta C_D(y)dy$$

the functions G_U and G_{C_d} maintain the same form as in the temporal theory (3.6), with the direct and adjoint eigenfunctions which are now normalized by imposing that $N_\alpha = -1$, with:

$$N_\alpha = \int_0^{y_\infty} \left[\left(U - \frac{2i\alpha}{Re}\right)(\overline{v^\dagger}v + \overline{u^\dagger}u) + \overline{p^\dagger}u + \overline{u^\dagger}p \right] d\,y$$

68

Let us now consider a problem in which U and C_D are not allowed to vary, but α and ω are. With reference to Equation (3.12), with any choice of normalization of direct and adjoint modes, it is found that $N_\omega \delta\omega = N_\alpha \delta\alpha$. Thus, once the adjoint problem is solved, it is possible to accurately compute the group velocity c_g of any stability problem using the value of N_ω and N_α , i.e.,

$$c_g := \frac{d\omega_r}{d\alpha_r} \approx \frac{real(N_\alpha)}{real(N_\omega)} \tag{3.13}$$

Note that c_g above is different from the "complex group velocity" $C_g := \dfrac{d\omega}{d\alpha} \approx \dfrac{N_\alpha}{N_\omega}$, and it is also $c_g \neq real(C_g)$. Relation (3.13) can be employed in either a spatial or temporal stability analysis and some representative results (for case G) are provided in Table I with the phase velocity $c_r := \omega_r/\alpha_r$ and the group velocity determined from Equation (3.13) . The temporal or spatial amplification factors, ω_i or $-\alpha_i$, respectively, are also given for all cases using Gaster's transformation: $\omega_i = -\alpha_i c_g$. Two types of errors on the calculation of the group velocity (noted err) are given in the table; the top four values, relative to the temporal theory, are defined as:

$$err = \frac{\left| c_g\big|_{(3.13)} - c_g\big|_{FD}\right|}{c_g\big|_{(3.13)}}$$

with $c_g\big|_{FD}$ arising from a first order finite difference approximation of the group velocity. The bottom four values are defined by the formula:

$$err = \frac{\left| c_g\big|_{temporal} - c_g\big|_{spatial}\right|}{c_g\big|_{temporal}}$$

The relative difference on c_g between temporal and spatial theory is rather low. It has to be kept in mind, however, that a stability analysis in the spatial framework yields a nonlinear eigenvalue problem, with a consequent larger numerical system than in the temporal framework; therefore, by inverting matrices of the same size, the accuracy is expected to be slightly lower. The accuracy of the growth rate approximated through Gaster's relationship is also found to be acceptable.

Theory	Re	α_r	ω_r	$-\alpha_i$	ω_i	c_r	c_g	$err(\%)$
Temporal	500	**0.5**	0.4778	*0.0248*	0.0254	0.9556	1.0245	0.54
	3450	**0.5**	0.4601	*0.0413*	0.0404	0.9202	0.9797	0.06
	10^5	**0.5**	0.4514	*0.0436*	0.0421	0.9028	0.9661	0.63
	10^9	**0.5**	0.4508	*0.0451*	0.0425	0.9016	0.9427	2.90
Spatial	500	0.4993	**0.4778**	0.0248	0.0250	0.9569	1.0100	1.41
	3450	0.4990	**0.4601**	0.0427	0.0404	0.9220	0.9471	3.30
	10^5	0.4996	**0.4514**	0.0449	0.0416	0.9109	0.9371	3.46
	10^9	0.4993	**0.4508**	0.0450	0.0411	0.9028	0.9143	3.01

Table 3.1: Temporal versus spatial stability, Case G. The model employed here is based on a modified Orr-Sommerfeld equation rather than a system based on primitive variables as done in the bulk of the paper—which is why the temporal results have slightly larger growth rates ω_i than those displayed in Fig. 3.2; this is related to the need of computing numerically d^2U/dy^2 and dC_d/dy in the Orr-Sommerfeld like equation. In italics, the growth rates obtained from Gaster's transformation are reported; the parameters imposed in each simulation are indicated with bold characters. The solutions for $Re = 10^9$ coincide with those found using the inviscid equations.

The amplitude of the sensitivity functions, $|G_U(y)|$ and $|G_{C_d}(y)|$, in the spatial and temporal stability frameworks is of same order of magnitude (not shown here) since they are related through the complex group velocity C_g . It is found that $|G_U^{temporal}| \approx |C_g||G_U^{spatial}|$ with $|C_g| \approx c_g \approx 1$ in the present case. Obtaining and comparing results in the temporal and spatial stability frameworks, such as in Table I, is a good means to validate the sensitivity functions and to verify the accuracy of the computations of the adjoint stability equations.

3.6   Concluding remarks

We have considered two different models of the flow through a vegetated layer experiencing Kelvin-Helmholtz destabilization. One model is based on the use of a single drag coefficient to express the force exerted by the vegetation on the fluid, the second considers the canopy as an orthotropic porous medium and is based on Darcy's equation with a tensorial permeability Zampogna and Bottaro [167]. Both models have advantages and drawbacks. The main advantage of the first model is that the drag coefficient can be taken to vary across the canopy; whether this positive consideration, based on macroscopic experimental measurements Ghisalberti and Nepf [64], Ghisalberti and Nepf [65] and Ghisalberti and Nepf [66], carries over to the stability problem remains to be established. The second model, applicable to dense porous media, considers two independent parameters to express

the disturbance flow perpendicular and parallel to the rigid dowels forming the canopy. Such parameters and components of the transversely isotropic permeability tensor $\mathbf{H}$ arise from the solution of a local Oseen problem (Zampogna and Bottaro [167]). The drawback of the second model is the fact that an interface (whether real or effective) appears, and adequate matching conditions must be enforced there. Despite much work since the seminal contribution by Beavers and Joseph [14], a consensus on the "best" interface conditions between a pure fluid region and a porous medium has not yet emerged. The models have been put to test through a classical sensitivity analysis (Bottaro et al. [21]). Beyond displaying stability results which correspond better to those to be expected from available experimental correlations Raupach et al. [134], Zampogna et al. [170], the anisotropic model is less sensitive to variations in the base flow (with potentially larger variations in frequency and growth rate of the instability mode for the case of shorter waves). As far as a direct comparison between G_{C_d} and $G_{H_{ii}}$ is concerned, this can hardly be made since the variables represent different objects; in particular, the pressure drop through the canopy depends directly on the drag coefficient and inversely on the permeability. The present results indicate that the anisotropic model depends significantly on the value of the apparent permeability component $\mathbf{H}_{11}$ (Zampogna and Bottaro [167]), whose evaluation must thus be conducted carefully. The problem of computing the effective permeability tensor will be addressed in the next chapter in which we show its modelling issues and possible solutions.

It also worth mention that the results presented here has been the basis for some other works (Gomez-de Segura et al. [68], Sharma et al. [142] and Garcia Mayoral and Abderrahaman-Elena [60]). The authors had used our approach to study some properties of the porous media to further explore drag reduction mechanisms and stability issues.

Chapter 4

Effect of geometrical parameters and inertia on the apparent permeability tensor in fibrous porous media

> *Before we work on artificial intelligence, why don't we do something about natural stupidity?*

> *- , Steve Polyak*

4.1   Introduction

Since Darcy's original formulation (Darcy [42]), which relates the flow rate through a porous bed to the pressure drop across the bed's sides, many corrections have been made to account, for example, for viscous effects (Brinkman [26]) or for the consequences of inertia (Forchheimer [58]). All of the cited works are of empirical nature, but the volume averaged methods (VANS) has been able to recover all of these formulations rigorously starting from the Navier-Stokes equations (Whitaker [162]).

As already seen in chapter 2, the VANS theory requires the knowledge of a number of terms, most notably, in the case of an isotropic porous bed, a permeability coefficient and a Forchheimer coefficient. Initial efforts in defining these terms were based on a combination of physical reasoning and measurements, leading to expressions known as the Kozeny-Carman Kozeny [87], Carman [34] and the Ergun Ergun and Orning [52] correlations. These approaches do not consider microstructural or geometrical features of the porous bed and are often restricted to simple unidirectional flows. In the present work we are concerned with a transversely isotropic material composed by parallel fibers of circular

cross-section, with one axis of symmetry, (O, x_3). In such materials the permeability is a diagonal tensor with the component in the direction parallel to the fibers greater than those along the transverse axes. For such an arrangement we will investigate, in this chapter, the effects of both the direction of the forcing pressure gradient and inertia. When the latter effect is present, embodied by a Reynolds number Re_d, based on mean velocity through the medium and fibers' diameter, exceeding an order one threshold, the permeability is no more simply defined upon geometrical properties. This extended permeability, which arises from a well-defined closure problem (2.49), is then called *apparent permeability.*

The influence of the geometry of the solid inclusions has been addressed previously by Yazdchi et al. [165] for arrays of cylinders in both square and hexagonal (or staggered) patterns, with the cylinders' section which can vary in shape. The results, in the two-dimensional and low Reynolds number limits, demonstrate the dependence of the permeability component along the flow direction to both the porosity and the direction of the macroscopic pressure gradient. The direction of the pressure gradient is found to have a weak effect for beds of medium-high porosity ($\varepsilon > 0.7$) and a stronger dependence appears upon the geometry of the solid inclusions.

The influence of the Reynolds number on the permeability and on the Forchheimer correction has been presented in a number of papers (Firdaouss et al. [56], Penha et al. [125] and Edwards et al. [50]). These authors show that, for arrays of fibers, the apparent permeability decreases with the increase of the Reynolds number, and the rate of this decrease depends on the geometry of the array; also, the Reynolds number is found to have a stronger influence on the apparent permeability when the medium is highly porous. The results of the work by Edwards et al. [50] agree with those by Zampogna and Bottaro [167] and with our own work (as shown later), all for the case of cylindrical fibers. Although some issues remain on the persistence of steady solutions in the simulations by Edwards et al. [50] in cases for which a limit cycle should have set in. A fully three-dimensional porous medium, more complex than those discussed so far, has been considered by Soulaine and Quintard [147], confirming the decreasing trend of the apparent permeability with the Reynolds number.

Another contribution which deserves mention is the one by Lasseux et al. [93]. They have computed the permeability tensor for various Reynolds numbers, in a two-dimensional geometry with cylinders of square cross-section. Forcing the flow along the main symmetric directions of the fiber, the same authors have identified different regimes:

- a creeping flow regime for $0 < Re_d < 10^{-3}$, without Forchheimer terms;

- a weak inertia regime for $10^{-3} < Re_d < 1$, with the Forchheimer correction quadratic in Re_d;

- a strong inertia regime for $1 < Re_d < 10$, where the Forchheimer correction is linear with the Reynolds number;

- a turbulent regime, for $Re_d > 10$, with the Forchheimer correction again quadratic with the Reynolds number.

The boundaries between the different regimes are specific to the geometrical arrangements and to the porosities being considered. A step forward in rendering (some of) these boundaries rigorous and independent of the arrangement of the pores, through the definition of a Reynolds number which accounts for a "topological" coefficient, has been recently made by Pauthenet et al. [124]. For the purposes of the present paper, we must retain that Lasseux et al. [93] have parametrized the Forchheimer correction with the Reynolds number, and have found that the inertial correction is orders of magnitude smaller than the Darcy's term, at least before the turbulent regime sets in. Moreover, Lasseux et al. [93] have studied how a Forchheimer tensor, **F**, depends upon the direction of the macroscopic forcing term with respect to the orientation of the square cross-section of the fibers, for Re_d up to 30. It is concluded that a deviation angle, γ, exists between the direction of the pressure gradient and that of the mean flow, because of the fibers' geometry. Finally, the inertial correction is strongly influenced by the orientation of the driving pressure gradient, and the Forchheimer tensor **F** is not symmetric (in fact the off-diagonal components are found to be inversely proportional to the diagonal terms, and symmetric with respect to rotations about the diagonal axis of the square, i.e. the direction at $45°$ in the $x_1 - x_2$ plane).

The effect of variations in the forcing angle, with restrictions to angles in the $x_1 - x_2$ plane, is also examined by Soulaine and Quintard [147] with conclusions in qualitative agreement with those of both the contribution just cited and our results described further below. In all cases, the off-diagonal components of the apparent permeability tensor are small and the diagonal components display but a small variation upon rotation of the driving pressure gradient.

Our aim is to show how the direction of the macroscopic pressure gradient, the porosity and the Reynolds number can modify the Darcy and Forchheimer closures arising from a VANS model of a fibrous porous medium. We are going to consider a three-dimensional unit cell for the microscopic model, with a generic forcing whose direction is defined by two Euler angles. Given the formidable space of parameters, some representative results are first shown and discussed. Response surfaces in the space of parameters are then identified by the use of a metamodel based on Kriging interpolation. They represent an extremely useful data base which can be afterward used in macroscopic simulations of flows through bundles of fibers of varying orientation and porosity.

4.2 The Volume-Averaged Navier-Stokes (VANS) method

The system under investigation consists of an incompressible Newtonian fluid which flows through a rigid porous medium. The governing equations valid at the microscale are:

$$\begin{cases} \dfrac{\partial \mathbf{v}_\beta}{\partial t} + \mathbf{v}_\beta \cdot \nabla \mathbf{v}_\beta = -\dfrac{1}{\rho_\beta}\nabla p_\beta + \nu_\beta \nabla^2 \mathbf{v}_\beta + \mathbf{f} \\ \nabla \cdot \mathbf{v}_\beta = 0 \end{cases}$$

where $\mathbf{v}_\beta$, p_β, ρ_β and ν_β stand, respectively, for the velocity, the pressure, the density and the kinematic viscosity of the fluid. The right-hand side term, $\mathbf{f}$, is a force (per unit mass) which drives the fluid motion and can be interpreted as the macroscopic pressure gradient acting on the system. In chapter 2 we have already shown how the above equations can be homogenized and a new set of equations, valid at the macroscale, can be retrieved. The macroscale system (2.31) introduce the surface integral term:

$$\mathbf{F}^m = \frac{1}{V} \int_{A_{\beta\sigma}} \mathbf{n}_{\beta\sigma} \cdot \left(-\frac{\tilde{p}_\beta}{\rho_\beta}\mathbf{I} + \nu_\beta \nabla \tilde{\mathbf{v}}_\beta \right)\, dA,$$

that we have discussed in chapter 2 section 2.4.1. This term is close by means of the equation (2.50) that we recall here:

$$\mathbf{F}^m \approx \mathbf{F}^M = -\nu_\beta \varepsilon \mathbf{H}^{-1} \cdot \langle \mathbf{v}_\beta \rangle^\beta \tag{4.1}$$

The two terms $\mathbf{F}^m$ and $\mathbf{F}^M$ can be interpreted as the force that the fluid exert on the solid structure of the porous medium. The two formulations are different only in the way of computing the force, the former one uses the miscroscopic representation and the latter the macroscopic one. The drag force $\mathbf{F}^m$ computed by direct numerical simulations (DNS) with account of all individual pores will be later compared to the model based on the permeability and Forchheimer tensors (whose equations are given below). Nonetheless, knowledge of the behavior of these tensors (or, equivalently, of the related apparent permeability) might prove both useful and instructive, in particular should one wish to extend the range of applicability of the model to cases for which the microscopic solution is not available.

The core of the VANS approach consists in the identification of the permeability and Forchheimer tensors. This problem, referred to as the closure problem, is discussed at length in paragraph 2.4.1. The two different tensors $\mathbf{K}$ and $\mathbf{F}$ can be computed by means by the two differential problems (2.48) and (2.49) reported here and discussed in detail in chapter 2.

$$
\begin{cases}
0 = -\nabla \mathbf{d} + \nabla^2 \mathbf{D} + \mathbf{I}, \\
\nabla \cdot \mathbf{D} = 0, \\
\langle d \rangle^\beta = 0 \\
\mathbf{D} = 0 \quad \text{at } A_{\beta\sigma}, \\
\mathbf{d}(\mathbf{x} + \ell_i) = \mathbf{d}(\mathbf{x}), \qquad \mathbf{D}(\mathbf{x} + \ell_i) = \mathbf{D}(\mathbf{x}), \qquad i = 1, 2, 3, \\
\langle \mathbf{D} \rangle^\beta = \varepsilon^{-1} \mathbf{K}.
\end{cases}
$$

The second closure problem differs from the first only for the presence of a linearised convective term in which the microscopic velocity obtained from the DNS, $\mathbf{v}_\beta$, is used as an input [1]. This of course implies knowledge of the microscopic velocity field. A Oseen-like approximation which relaxes this constraint has been proposed by Zampogna and Bottaro [167].

$$
\begin{cases}
\dfrac{\mathbf{v}_\beta}{\nu_\beta} \nabla \mathbf{M} = -\nabla \mathbf{m} + \nabla^2 \mathbf{M} + \mathbf{I}, \\
\nabla \cdot \mathbf{M} = 0, \\
\langle m \rangle^\beta = 0 \\
\mathbf{M} = 0 \quad \text{at } A_{\beta\sigma}, \\
\mathbf{m}(\mathbf{x} + \ell_i) = \mathbf{m}(\mathbf{x}), \qquad \mathbf{M}(\mathbf{x} + \ell_i) = \mathbf{M}(\mathbf{x}), \qquad i = 1, 2, 3, \\
\langle \mathbf{M} \rangle^\beta = \varepsilon^{-1} \mathbf{H}.
\end{cases}
$$

The closure problems reflect the structure of the solution of the two system (2.48) and (2.49). In particular, the solution of the former depends only on the geometry of the porous medium so that the permeability tensor $\mathbf{K}$ is symmetric. This is not the case for $\mathbf{H}$, because of the effect of the microscopic velocity amplitude and direction. Clearly, the solution of system (2.49) tends to that of (2.48) when $Re_d \to 0$.

4.3 Validation and setup

In this section the numerical methodology, the parameters, the setup and the validation for some reference cases are given.

4.3.1 Computational domain

The geometry used for the base REV is shown in figure 4.1: a cylindrical inclusion is present at the center of the REV and four quarters of cylinders are situated at the corners. The

---

[1]En extension to this model that does not require the DNS velocity as input has been proposed in Valdés-Parada et al. [154]. However this extension still need more verification and validation.
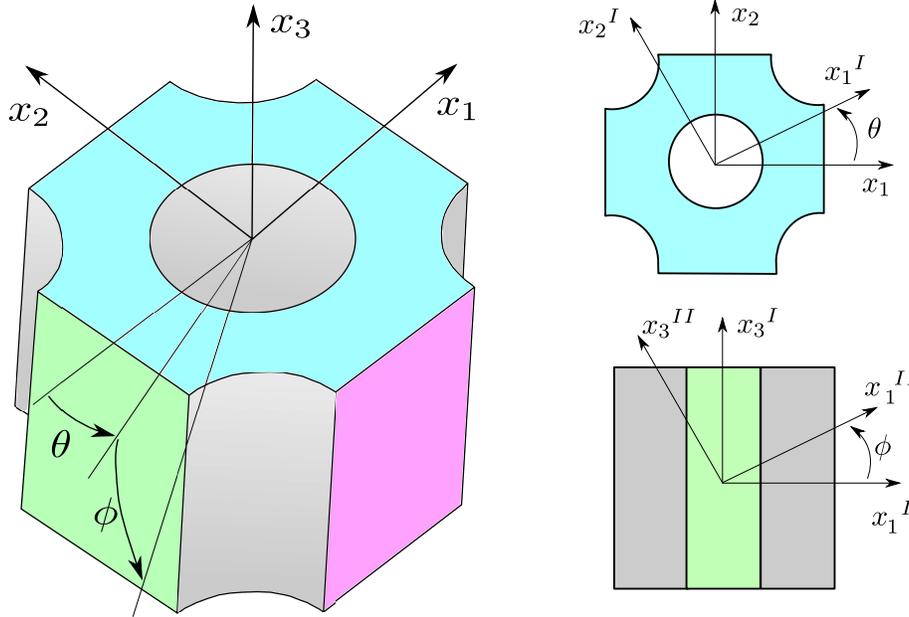
Figure 4.1: REV for the fiber geometry investigated.

lateral length of the cubic envelop is ℓ, which is used as length scale for the microscopic problem; the diameter d of the cylinders is adapted as a function of the desired porosity ε, ratio between the fluid volume over the total REV volume (ℓ^3).

The forcing term $\mathbf{f}$ of the DNS is a vector whose direction is defined by two Euler angles, with rotations of the form: $\theta \, \mathbf{e_3} + \phi \, \mathbf{e_2}^I$ (cf. figure 4.1). Its amplitude is set a priori and is connected to the Reynolds number, Re_d, defined with the mean velocity over the REV and the fiber diameter, d. Re_d is a result of the calculations, once the mean velocity is evaluated.

4.3.2 Numerical setup

The simulations have been carried out with the open-source code OpenFOAM Weller et al. [157], based on a finite volume discretization with a centered arrangement for the unknowns. The standard solver icoFoam (incompressible Navier-Stokes) has been modified in order to include a constant pressure gradient acting as a forcing term $\mathbf{f}$ in equation (4.1). The coupling between the velocity and the pressure equations is based on the pressure implicit split operator referred to as the PISO algorithm. The time derivative term is discretized using the second order backward Euler scheme and all the spatial terms use a second-order central difference stencil based on Gauss finite volume approach. The velocity system is solved with a preconditioned bi-conjugate gradient (PBiCG) iterative solver with the tolerance on the velocity residuals set to 10^{-8}, associated to a diagonal incomplete lower upper

pre-conditioner (DILU). The pressure equation is solved with a geometric-algebraic multi-grid (GAMG) algorithm associated to a Gauss-Seidel smoother and the tolerance on the pressure residuals is here equal to 10^{-6}. Cyclic boundary conditions are applied to all fields on all fluid boundaries along the three directions, and the no-slip condition is imposed on the surface of the solid inclusions. The time step Δt is automatically determined to ensure that the maximum Courant number, Co, respects the condition: $Co = ||v_\beta|| \, \Delta t/\Delta x < 1/2$, in which $||v_\beta||$ is the local velocity magnitude in the REV and Δx is the local grid spacing. Co is basically the ratio between the fluid speed and the velocity to propagate information through the mesh and the condition $Co < 1/2$ is found to be sufficient to have a stable solver.

4.3.3 Mesh convergence analysis

The mesh has been computed using the internal OpenFOAM mesher named *snappy-HexMesh*. The final grid is mainly composed by hexahedral cells with a refined regular grid in the boundary layer regions next to the solid surfaces. Three different mesh sizes, with 0.65×10^6, 10^6 and 1.5×10^6 elements, have been tested in order to demonstrate spatial convergence. This has been assessed using the Grid Convergence Index (GCI) introduced by Roache [136].

Details of the coarsest mesh used are shown in figure 4.2. On the right frame a close up of the grid in the neighborhood of the fiber's boundary is displayed: twenty points are used in the structured portion of the mesh along the wall-normal direction.
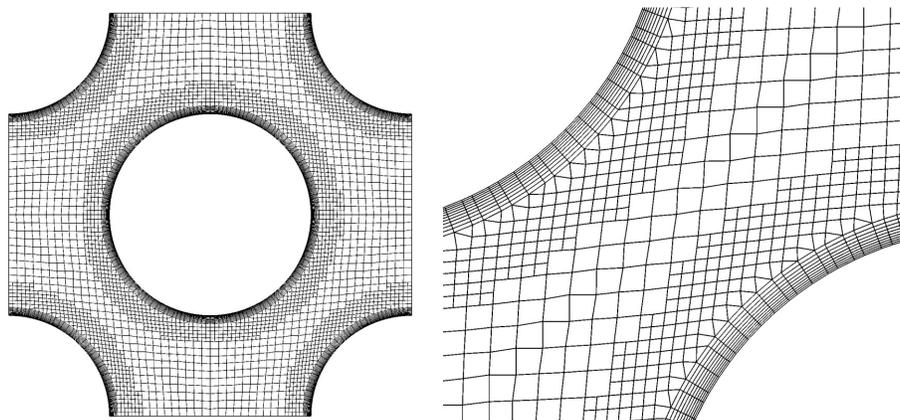
Figure 4.2: Mesh used for the computation; top view (left) and zoom in the boundary layer region (right). $\varepsilon = 0.6$.

The GCI method is based upon a grid refinement error estimator derived from the theory of generalized Richardson extrapolation. It measures the ratio between the computed value of a quantity over the asymptotic numerical value, thus indicating how far the

mesh index	mesh identifier	average REV velocity		metric	value
3	fine	1.11		GCI_{23}	0.366%
2	medium	1.07		GCI_{12}	1.11%
1	coarse	1.09		AC	1.006

Table 4.1: Convergence analysis. Left: average velocity within the REV, normalized with $\frac{K_{11}}{\nu_\beta}||\mathbf{f}||$. Right: grid convergence metrics. The REV has $\varepsilon = 0.6$, the motion is along x_1, i.e. $\theta = \phi = 0$ and $Re_d \to 180$.

solution is from the asymptotic ("exact") value. The procedure is simple and provides a method to estimate the order of the spatial convergence, based on two or three different grid sizes. First of all, the grids must be generated with the same algorithm and they must have the same final quality. In each simulation a physical scalar quantity representative of the physical phenomenon must be sampled. The method follows the following four steps:

1. Estimate the order of convergence of the procedure, defined as $p = \ln\left(\dfrac{f_3 - f_2}{f_2 - f_1}\right) / \ln r$, where r is the grid refinement ratio between each grid (it is computed as the ratio between the number of elements of two consecutive grids; the approach imposes that r should remain constant between any couple of consecutive grids and be larger than 1.1), and f_i represents the quantity of interest in each grid (1=coarse, 2=medium and 3=fine).

2. Compute the relative error between grid i and j: $\left.|\epsilon|\right|_{ij} = \dfrac{f_j - f_i}{f_i}$, for $(i,j) \in \{(1,2),(2,3)\}$.

3. Compute $GCI_{ij} = \dfrac{F_s |\epsilon|_{ij}}{r^p - 1}$, with F_s a safety factor equal to 1.25 if the grids are three, and equal to 3 if the grids are only two Roache [136].

4. Check whether each grid level yields a solution that is in the asymptotic range of convergence; this means that the quotient $AC = \dfrac{GCI_{23}}{GCI_{12}} \dfrac{1}{r^p}$ should be as close as possible to one.

In our case the quantity of interest chosen is the intrinsic average velocity inside the porous medium, and the we have used a Reynolds number equal to 180 to well take into account all possible inertia effects. For these specifications the results are summarized in table 4.1. From the table it can be seen that the intrinsic velocity difference is very small from one grid to the next and the coarse grid provides results close to the expected asymptotic value.
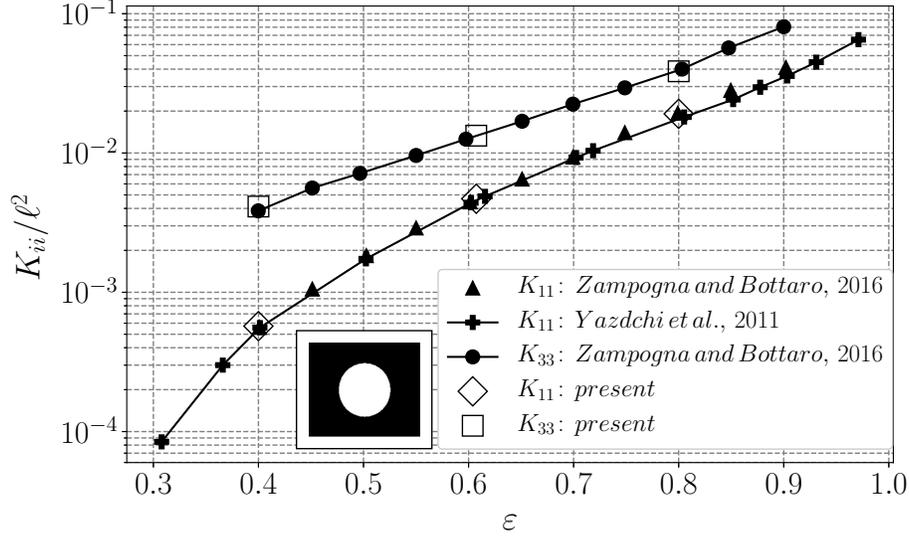
Figure 4.3: Permeability versus porosity for a square arrangement of cylinders. The scaling of the permeability is ℓ^2 and is explicitly indicated in the vertical axis.

This is taken as a sufficiently convincing argument to carry out all the computations in the following with a grid density equal to that of grid 1.

4.3.4 Validation on two different configurations

The results published in the literature by Zampogna and Bottaro [167] and Yazdchi et al. [165] are now used to validate both the methodology and our choices of the computational parameters. In the cited papers, three-dimensional computations of the permeability components in different cells geometries are presented.

Figure 4.3 displays the comparison for a cell with a square arrangements of the fibers; here the permeability is evaluated along the two principal directions, x_1 and x_3. A good agreement is found with the published results. Figure 4.4 shows a similar comparison for a staggered arrangement of the inclusions in the unit cell. In this case the section of the cell is rectangular. The agreement for the only permeability component available in the literature is again satisfactory.

Finally, to check the correct implementation of the closure model (4.1) it is important to verify the equality between the amplitude F^M of the macroscopic force and its microscopic counterpart F^m obtained through an integration of the DNS fields over the solid boundaries of the inclusions in the REV. Figure 4.5 shows a plot of the relative error between these two forces, i.e. $\dfrac{||F^M - F^m||}{||F^m||}$, as function of the Reynolds number. We consider the successful
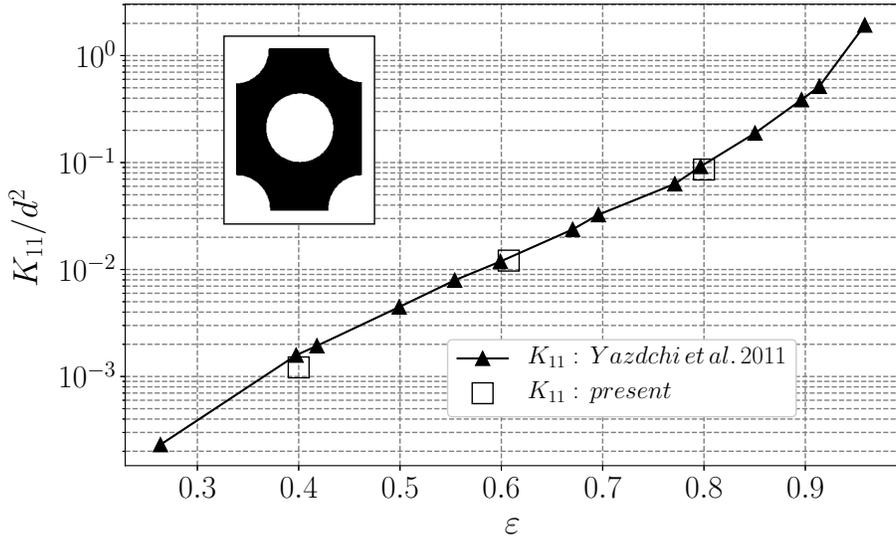
Figure 4.4: Permeability versus porosity for a staggered arrangement of cylinders. The permeability component is here scaled with d^2 (and not ℓ^2), with d the diameter of the inclusions.

comparison displayed in figure 4.5 as the conclusive demonstration of the validity of the approach described here. We have nonetheless carried out the same verification displayed in figure 4.5 for each one of the simulations described in the following, to our satisfaction.

4.3.5 Tests with larger REV's

Since the Reference Elementary Volume (REV) is the unit cell within the porous medium over which average quantities of the VANS are computed, it is important to choose its dimensions appropriately in the inertial regime for, if the REV is too small, it might be easy to miss crucial features of the wakes. For example, to predict the critical Reynolds number, Re_c, of the first Hopf bifurcation, a REV containing at least three solid inclusions in the direction of the mean pressure gradient is necessary in the simulations by Agnaou et al. [3]. Among the results reported, it is found that, for a fixed REV size, the error committed in the evaluation of the critical Reynolds number increases with the porosity. This same error is considerably reduced when the mean pressure gradient angle is $\theta = 45°$. Thus, the choice of the number of inclusions in a REV is a task not to be overlooked, and the final choice must account for the porosity, the direction of the pressure gradient and the microscopic Reynolds number.

Here, the influence of the numbers of inclusions present in a REV is assessed by focussing only on the velocity components after averaging over the REV. The unit cubic cell of side

81
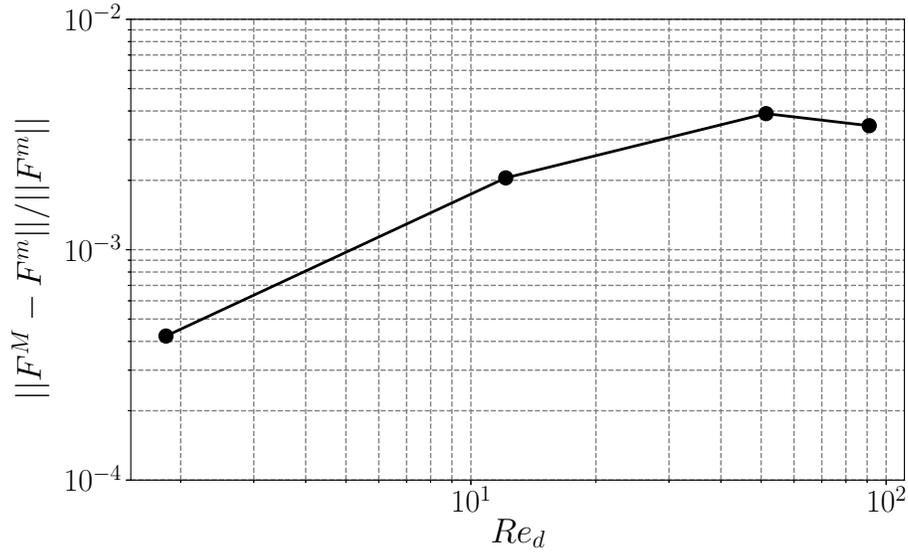
Figure 4.5: Relative error between the microscopically computed forces along the x_1 direction and those arising from the Darcy-Forcheimmer model; $\varepsilon = 0.8$ for the REV in the staggered arrangement of Yazdchi et al. [165].

ℓ is used as reference: starting from this, two additional REV's are built, as shown in figure 4.6. The first one is doubled in both the x_1 and x_2 directions and the case tested numerically is characterised by $\theta = 0$, $\phi = 0$ (i.e. the forcing pressure gradient is directed along x_1), porosity $\varepsilon = 0.6$ and $Re_d = 50$. The second REV configuration is a composition of 3 reference REVs on top of one another along x_3, with the parameters set to $\theta = 45°$, $\phi = 45°$, $\varepsilon = 0.6$ and $Re_d = 100$.

For both these test cases, no appreciable differences, neither in the mean velocity nor in the forces on the fibers, have been observed, with relative errors on the mean velocity with respect to the reference case which remain below 2%. We take this as sufficient evidence to use, in the following, only the reference cubic REV of side equal to ℓ, with the understanding that only configurations with Re_d up to around 100 can be considered.

4.4   Microscopic solutions

In this section, some local microscopic fields computed with direct numerical simulations are shown, together with components of the intermediate tensor $\mathbf{M}$ coming from the numerical solution of the closure equations (4.2).

In figure 4.7 (top row) the local x_1 velocity component is drawn for the two-dimensional flow when $\varepsilon = 0.6$, for three Reynolds numbers, to cover the transition from the Stokes
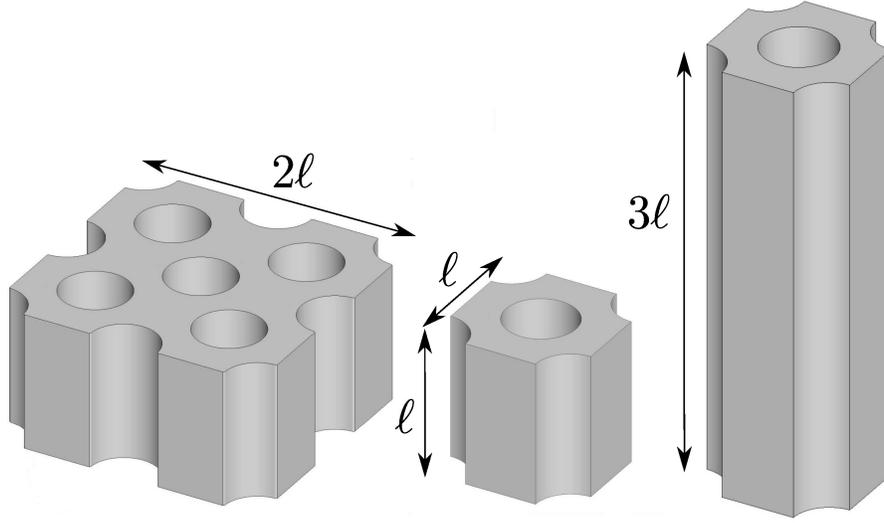
Figure 4.6: REV configurations. Left: $2 \times 2 \times 1$ arrangement; centre: $1 \times 1 \times 1$ arrangement (reference); right $1 \times 1 \times 3$ arrangement.

to the inertial regime. In all plots, the velocities are rendered non-dimensional by the corresponding value of $\dfrac{K_{11}}{\nu_\beta}||\mathbf{f}||$. When inertia is absent, the flow has a central symmetry; by increasing the Reynolds number, only the symmetry with respect to the x_1 axis is maintained (x_1 is the direction of the forcing pressure gradient), with the wake's length which increases with Re_d. When Re_d is of order 100 the wake spreads to the downstream boundary of the REV, re-entering, because of periodicity, at the upstream side. This Re_d represents the upper limit of validity for the cubic unit cell of side ℓ; larger values of Re_d could only be investigated with longer/larger/thicker REV's.

The non-dimensional local M_{11} fields for the same parameters are displayed in figure 4.7 (mid row). All values in the figures arise from scaling $\mathbf{M}$ with ℓ^2. Visually, these local fields are strongly correlated to the local streamwise velocity component in the whole Re_d range. This is not unexpected since the local velocity drives the convective term of system (4.2). The central symmetry of all components of $\mathbf{M}$ in the Stokes regime is coupled to the rotational invariance of the apparent permeability tensor in two-dimensional flows.

The effect of varying the porosity is shown in figure 4.7 (bottom row) where ε is taken equal to 0.4. Even at such a low porosity the stretching of the wake can be noticed, and it increases with Re_d. Interestingly, this effect is milder when the forcing is inclined by an angle ϕ, since the tighter packing of the inclusions causes a strong deviation of the mean flow along the axis of the fiber. In this case, M_{11} and M_{22} behave very similarly to the case $\phi = 90°$.
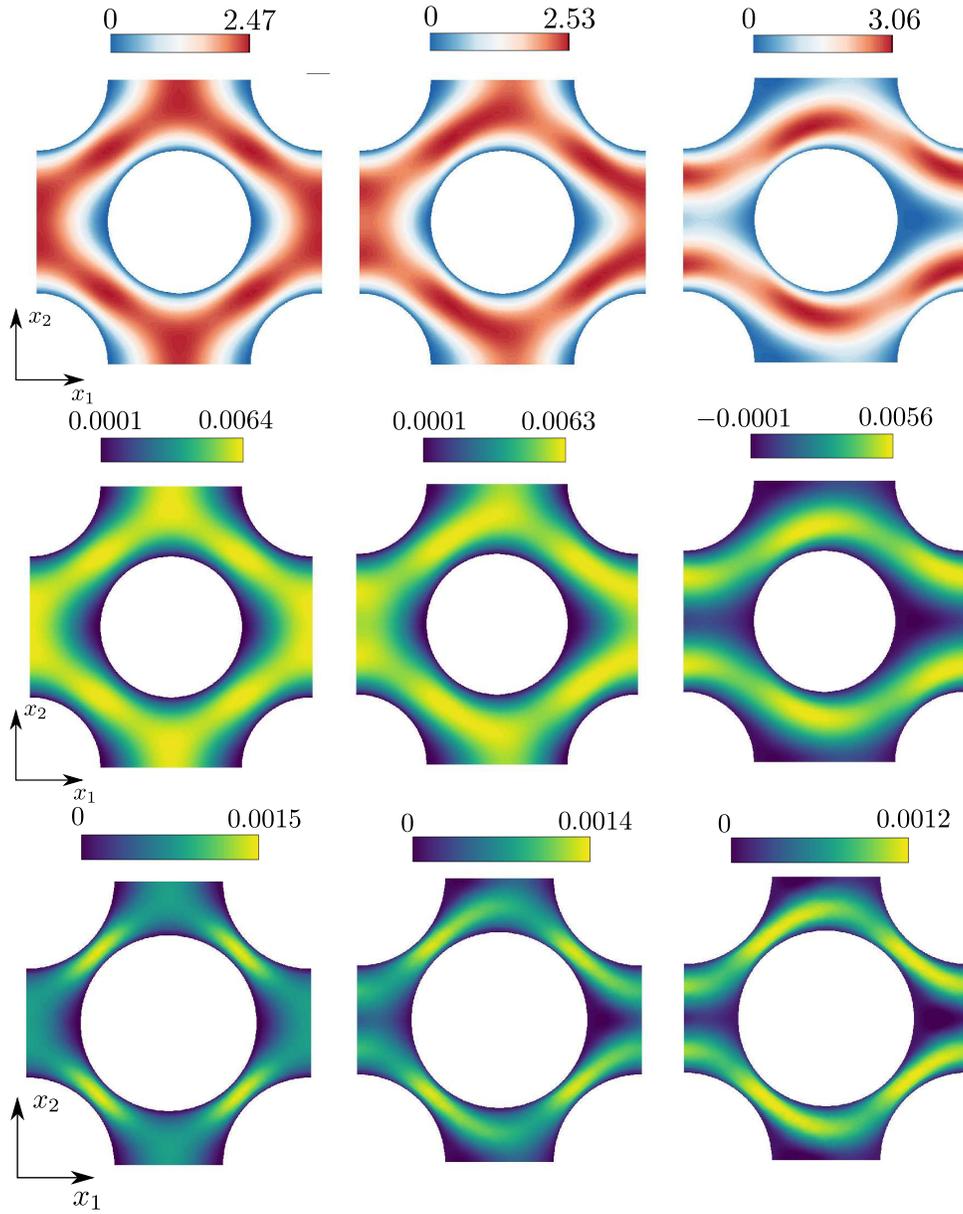
Figure 4.7: Top row: plane view of the dimensionless x_1 component of the local velocity field $\mathbf{v}_\beta$ for the case $\theta = 0$, $\phi = 0$, $\varepsilon = 0.6$ and for three Reynolds numbers $Re_d = 0, 10, 50$, from left to right. Mid row: microscopic M_{11} fields corresponding to the images in the top row. Bottom row: M_{11} fields for the same Euler angles and Reynolds number as in the top two rows, and smaller porosity ($\varepsilon = 0.4$).

Another interesting point emerges by inspection of figure 4.8 where two off-diagonal components of **M** are shown for two porosity values; the first image (left frame) represents a plane flow in the Stokes regime while the second is the plane cut of a three-dimensional solution in the inertial regime. Positive and negative values of the microscopic fields can be seen in both images but, once averaging is applied over the REV, the resulting permeability component is very close to zero (in fact, exactly equal to zero in the Stokes case). This same features occurs for all off-diagonal terms in all cases examined, so that, within the current range of Reynolds numbers, the apparent permeability tensor is, to a good approximation, diagonal[2].
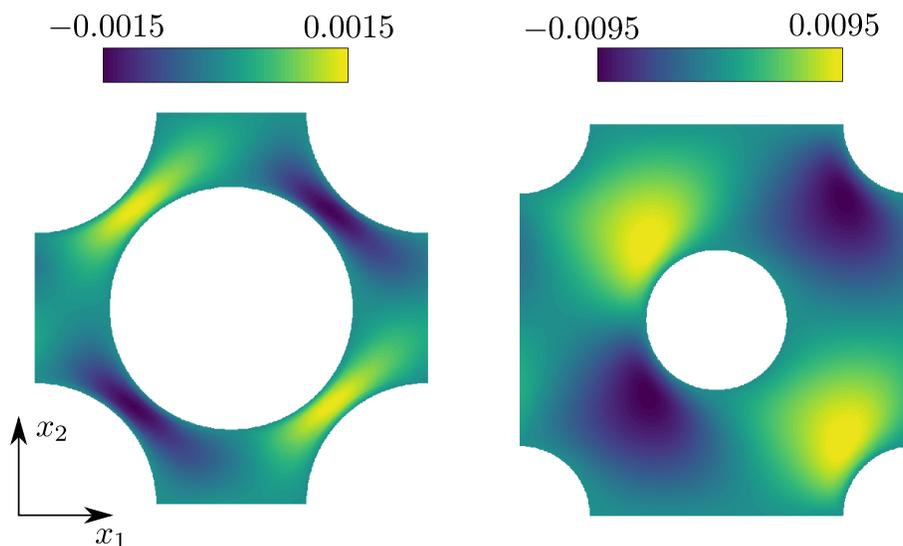
Figure 4.8: right: Non-dimensional M_{21} field for $\theta = 0, \phi = 0, Re_d = 10, \varepsilon = 0.8$, left: Non-dimensional M_{12} field for $\theta = 22.5°, \phi = 45°, Re_d = 50, \varepsilon = 0.4$.

A three-dimensional case is shown in figure 4.9, where all the non-zero terms of the **M** tensor are plotted for a porous structure with $\varepsilon = 0.6$. The components shown are M_{11}, M_{22}, M_{33}, M_{12} and M_{21}, while M_{i3} and M_{3j} are not plotted because they are identically zero to machine accuracy. Distinct features are visible in each image; in particular, in the last frame the M_{33} microscopic component displays a low wavelength structure along the cylinder's axis. Increasing the dimensions of the REV along x_3 does not alter such a structure, i.e. the ℓ^3 domain chosen with its periodic boundary conditions does not filter out significant high wave-numbers of the flow.

---

[2]In fact, there are always at least two orders of magnitude differences between the diagonal and the off-diagonal components. While the latter should not, in principle, be ignored, we will focus attention here only on the dominant terms of the permeability tensor.
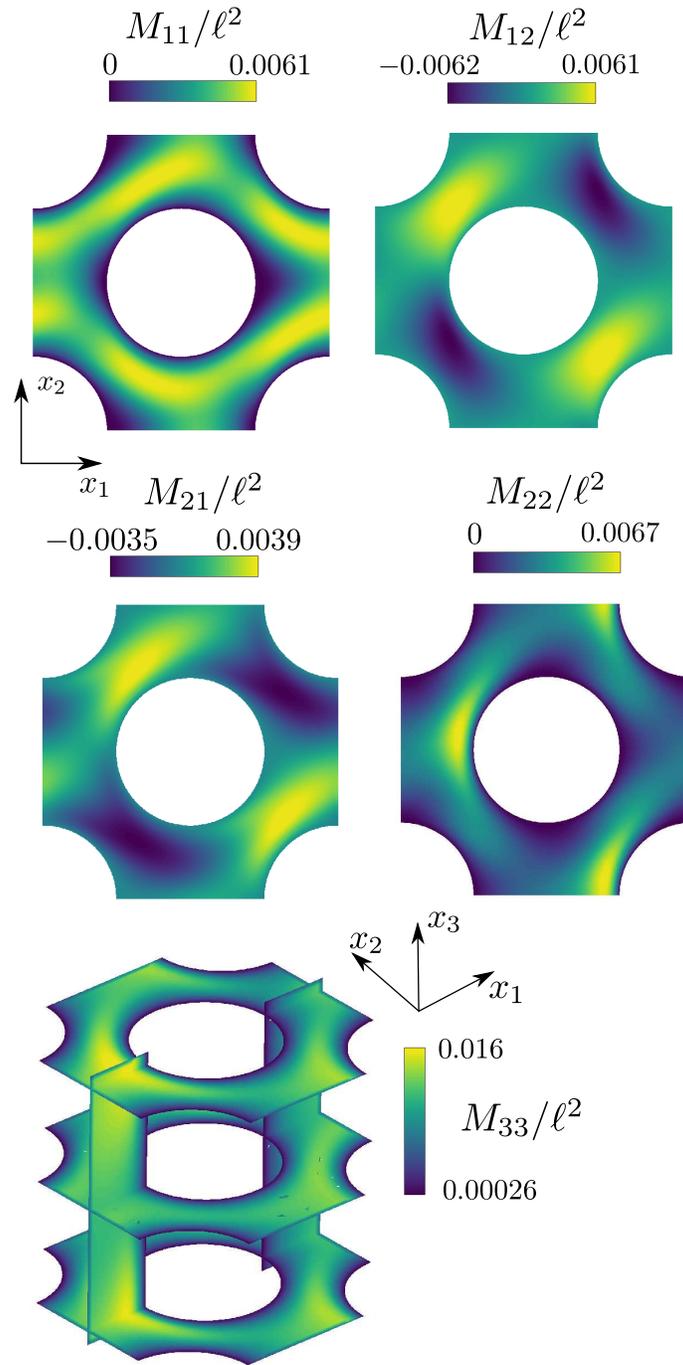
Figure 4.9: Non-dimensional **M** components fields for the case $\theta = 22.5°, \phi = 45°, Re_d = 50, \varepsilon = 0.6$.

index	θ	ϕ	field properties
1	0°	0°	2D symmetric
2	22.5°	0°	2D non-symmetric
3	0°	45°	3D symmetric
4	22.5°	45°	3D non-symmetric
5	–	90°	3D symmetric

Table 4.2: Directions of the forcing tested and property of the solutions.

We further note that the tensor $\mathbf{M}$ is not symmetric in this case since each off-diagonal component represents the solution of the closure problem in a specific direction (first index of the field) and the forcing term acts orthogonally to it (second index of the field). Once averaged over the REV it is found that both H_{12} and H_{21} are very close to zero.

4.5   The apparent permeability tensor

In this section the variations of the diagonal components of the permeability tensor $\mathbf{H}$ are discussed as function of the direction of the mean forcing, the Reynolds number and the porosity. As stated previously, the Reynolds number ranges from 0 to approximately 100 in order to capture phenomena associated with inertia; the cases considered never lead to unsteady signals. The porosity parameter ε is set to either 0.4 (low porosity), 0.6 (medium) or 0.8 (high). The forcing direction is defined by the Euler angles and all the configurations considered in this section are summarized in table 4.2; the choice has been made to explore a reasonably large range of parameters, with both two-dimensional and three- dimensional flows characterized by symmetric and asymmetric patterns.

Let us briefly recall the methodology. First, a DNS is carried out to compute the microscopic flow. Then the closure problem is solved for the tensor $\mathbf{M}$. Finally, each component of the apparent permeability $\mathbf{H}$ is obtained by averaging (equation (2.49)). The results are collected in figures 4.10, 4.11 and 4.12, showing the variation of the diagonal components of $\mathbf{H}$.
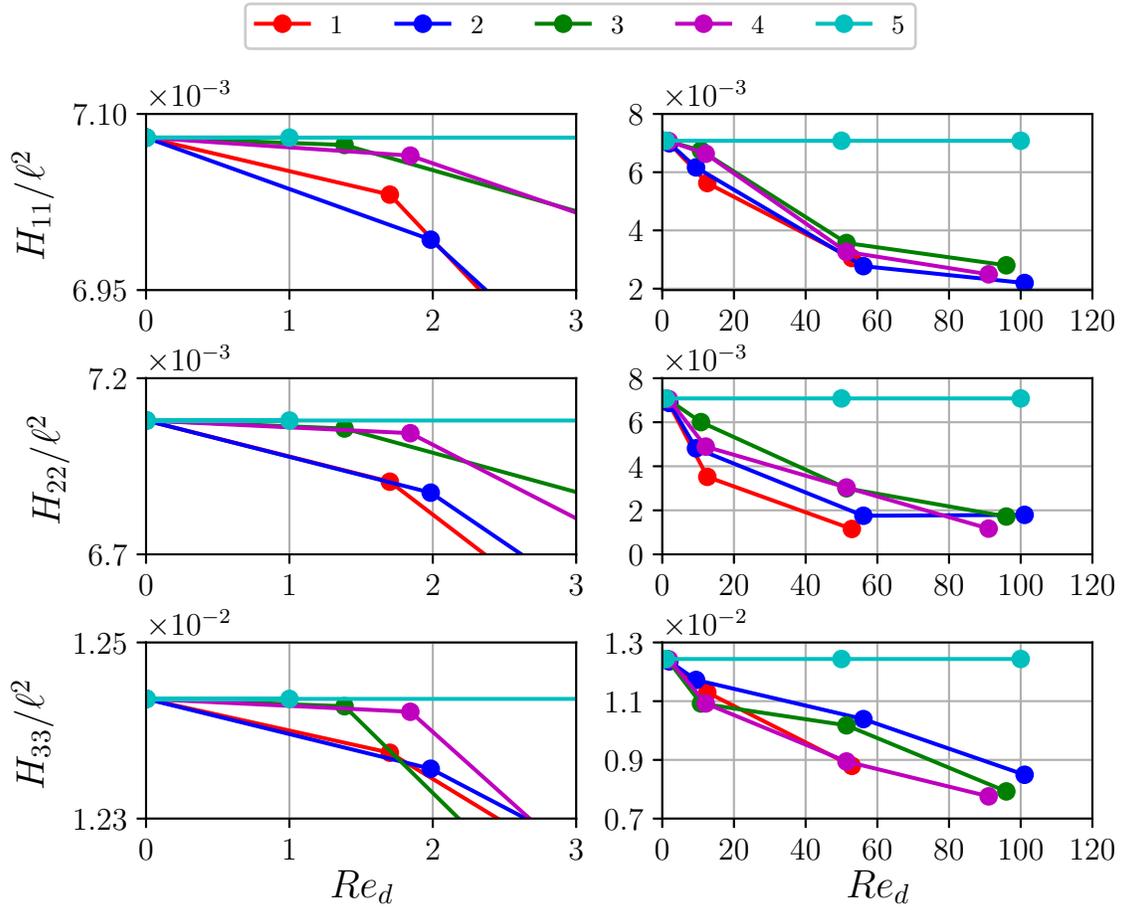
Figure 4.10: Diagonal elements of the apparent permeability $\mathbf{H}$ as function of the Reynolds number for porosity $\varepsilon = 0.8$. The forcing direction is represented through the couple of Euler angles (θ, ϕ) (cf. table 4.2 for the case index). Left column: low-Re_d regime; right column: inertial regime.
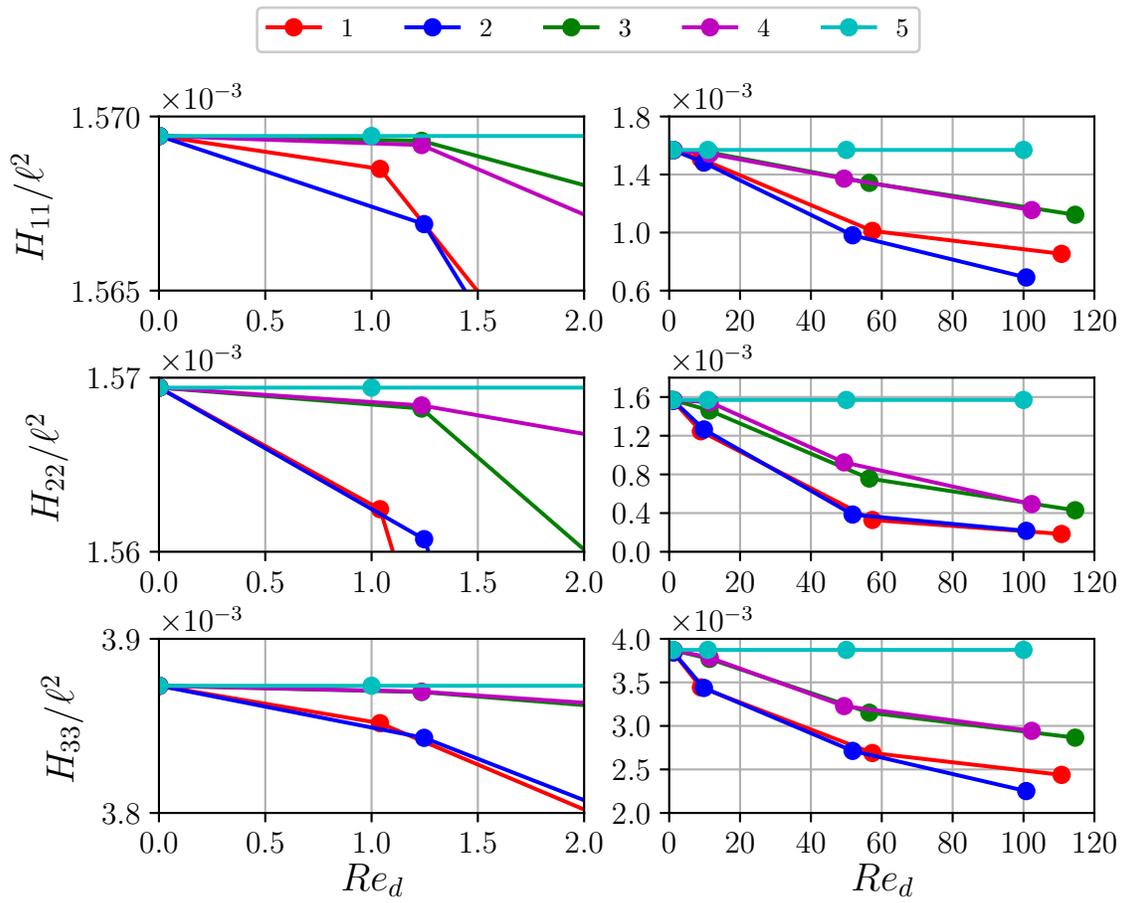
Figure 4.11: Same as figure 4.10 with porosity $\varepsilon = 0.6$.
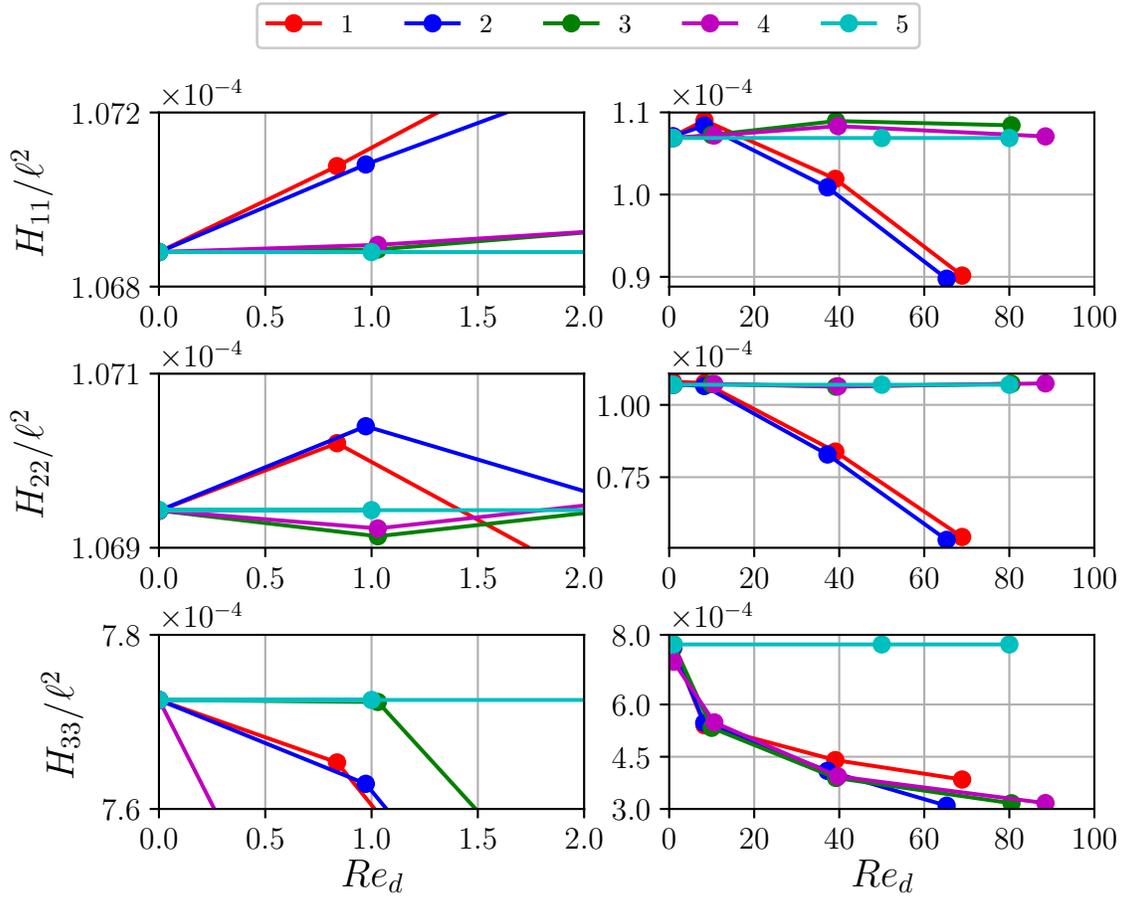
Figure 4.12: Same as figure 4.10 with porosity $\varepsilon = 0.4$.

In the left column of each figure we focus on the low-Re_d regime ($0 < Re_d < 2$), while in the right column the effect of inertia can be assessed. As expected, when Re_d is small the apparent permeability is quasi-Reynolds-number-independent (and can be approximated well by the true permeability). As the Reynolds number increases above a few units, inertial effects grow in importance yielding typically a monotonic decrease of all components of **H**, aside from case indexed 5 ($\phi = 90°$) for which the flow remains aligned with the cylinder's axis. In case 5 the microscopic flow solution is invariant with x_3 and does not change with Re_d in the range considered, so that **H** is a constant tensor.

When the porosity is large all components show a similar behaviour irrespective of the forcing angle (except, clearly, case 5). Differences start appearing at $\varepsilon = 0.6$; the two cases with $\phi = 0°$ (index 1 and 2) behave similarly, and so do the two cases indexed 3 and 4 (with $\phi = 45°$). This seems to suggest a weaker effect of θ on the permeability components.

90

For even smaller porosity ($\varepsilon = 0.4$), the blockage which the inclusions cause to the flow produces the unexpected behaviour displayed in figure 4.12. When the flow is purely two-dimensional (cases 1 and 2), variations in the Reynolds number affect $\mathbf{H}$ significantly; when a pressure gradient along x_3 is present the strong packing of the fibers constrain the fluid to flow prevalently along the fibers' axis, and the apparent permeability is almost Re_d-independent. When assessing variations in H_{jj} for this case, attention should also be paid to the fact that the permeability is now at least one order of magnitude smaller than in the previous cases so that variations of the diagonal components shown in figure 4.12 are tiny in absolute terms. This is related to the fact that the inverse of the permeability plays the role of a drag coefficient in the macroscopic expression of the force (cf. equation (2.31)). In other words, materials with higher porosity (larger space between solid inclusions) offer lower resistance to the motion of the fluid.

Applying the intrinsic average operator to the non-diagonal component of the tensor $\mathbf{M}$ results in terms that are negligible with respect to their diagonal counterparts, and these results are true for all the parameters considered. This means that there is a very weak coupling between the principal directions of the fiber. The directional decoupling and the diagonal property of the apparent permeability tensor has also been computationally demonstrated on a completely different REV geometry by Soulaine and Quintard [147]. Conversely, Lasseux et al. [93] have carried out a two-dimensional study with fibers of square cross-section, finding that the off-diagonal terms are non-negligible and only about one order of magnitude smaller than the diagonal components. This result is a consequence of the non-rotationally-invariant geometry considered. The present work and the two articles just cited suggest that the diagonal property of the tensor $\mathbf{H}$ is closely related to the geometry of the porous material, more than to the flow regime.

4.6 A metamodel for H

The previous sections has shown how the apparent permeability depends on the two Euler angles, the Reynolds number and the porosity. The space of parameters is formidable and the results found so far are not sufficient to treat, for example, cases characterized by multiple inclusions' sizes and orientations in different regions of the domain, or cases involving a poroelastic medium, with temporally and spatially varying porosity, flow direction and local Reynolds number. The complete solution of the closure problem for a single set of parameters takes approximately 4 CPU hours on our two-processor Intel(r) IVYBRIDGE 2.8Ghz, each with 10 cores and 64 GB of RAM, so that a complete parametric study is, to say the least, unpractical. In view of this, the construction of a metamodel capable to provide a full characterisation of the permeability as a function of all parameters is a worthy endeavor. We have tested several surrogate models, before eventually settling on the kriging approach Kleijnen [86] described in the following.

parameter	values				
θ	0°	22.5°	45°		
ϕ	0°	22.5°	45°	67.5°	90°
Re_d	0	10	50	100	
ε	0.4	0.6	0.8		

Table 4.3: Sampling parameters.

4.6.1   DACE sampling

The first step to build a metamodel is the collection of relevant samples. The quality of the final metamodel strongly depends on the samples collected and their number and distribution is of primary importance. The apparent permeability tensor, **H**, depends on four independent variables; the samples have been generated starting from the set of parameters given in table 4.3.

One of the best options to generate the relevant database would be to use a full factorial design approach in which all the combinations of the four variables from table 4.3 are computed. Because of the large number of computations required, this approach has not been retained. We have resorted to the methodology known as DACE (Design and Analysis of Computer Experiments), a technique to fill in the best possible way the space of the parameters of the problem. The Dakota library Adams et al. [2] has been selected for the purpose and the Monte-Carlo incremental random sampling algorithm Giunta et al. [67] has been chosen, in order to make efficient use of the cases already computed. This incremental approach selects in a quasi-random way the new samples to generate, starting from the existing ones. In the end, the set of samples comprises 118 cases.
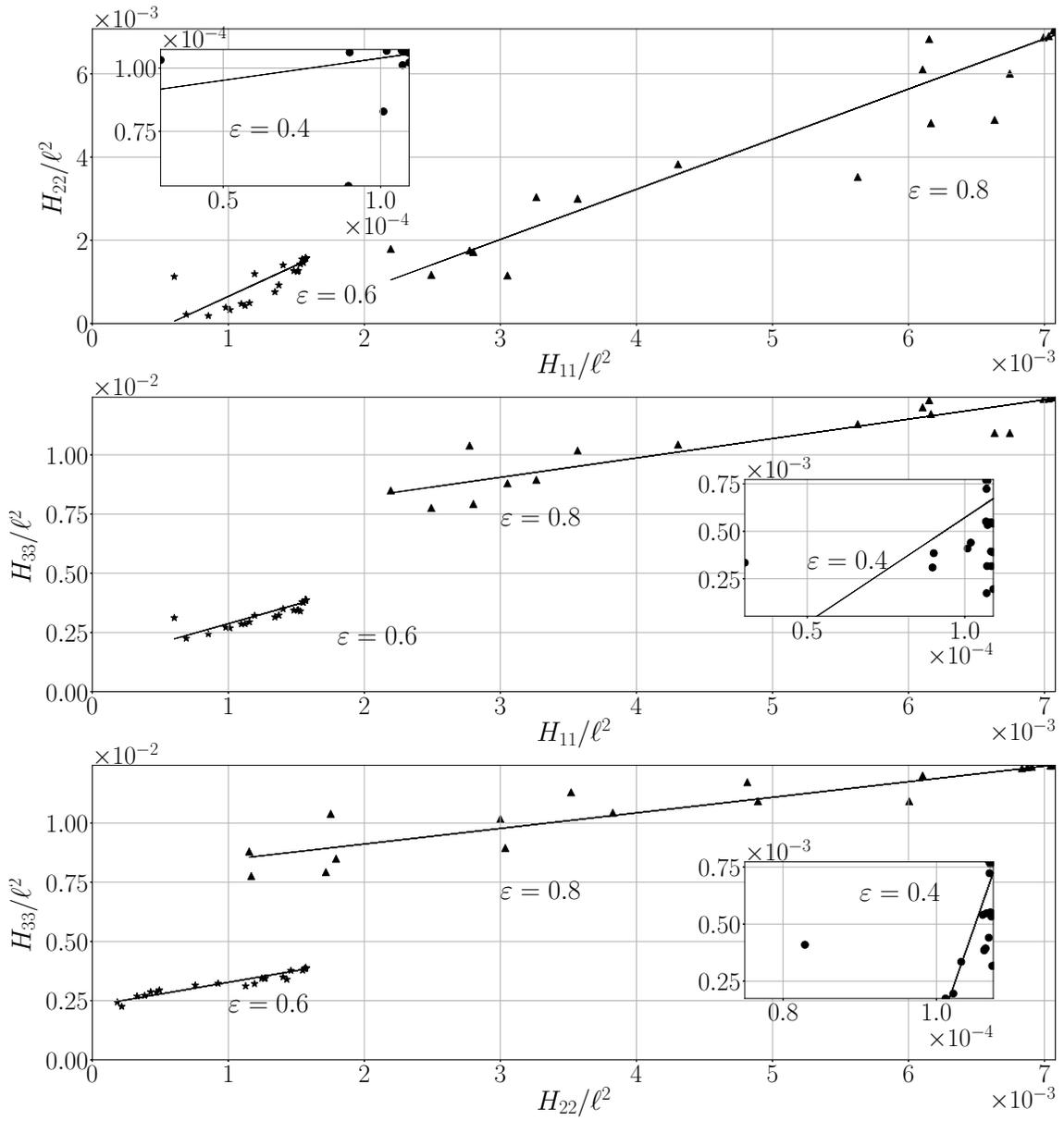
Figure 4.13: Scatter matrix plot for the collected numerical data of the apparent permeability tensor.

In the scatter plot of figure 4.13 the three diagonal components of the permeability tensor are shown as function of one another. The three porosities are separately considered in each of the above plot, and the permeability points are represented with their linear regression on top. This kind of plot is common in statistical analysis to determine if correlations in the data are present. The permeability components show some correlation with the data points which lie reasonably well on a straight line. This result has a physical implication. Remembering the diagonal dominance of the permeability tensor, we have in the low Re_d limit:

$$\left(\langle u_\beta\rangle^\beta, \langle v_\beta\rangle^\beta, \langle w_\beta\rangle^\beta\right) \sim \left(H_{11}\frac{\partial p}{\partial x_1}, H_{22}\frac{\partial p}{\partial x_2}, H_{33}\frac{\partial p}{\partial x_3}\right). \tag{4.2}$$

It is then possible to compute the angle between the forcing term, ∇p, and the average velocity vector, represented in figure 4.14 for the two-dimensional case, $\phi = 0$. This is achieved by taking the ratio between the first two components of Darcy's equation, calling γ the flow deviation with respect to the mean forcing. We thus have:

$$\tan(\theta + \gamma) = \frac{H_{22}}{H_{11}}\tan\theta. \tag{4.3}$$

If the ratio between the two permeability components is equal to one, the angle γ vanishes. The correlation between H_{11} and H_{22} controls the deviation of the flow in the (x_1, x_2) plane, and the argument can easily be extended to H_{11}/H_{33} and H_{22}/H_{33} for deviation angles in three-dimensions.
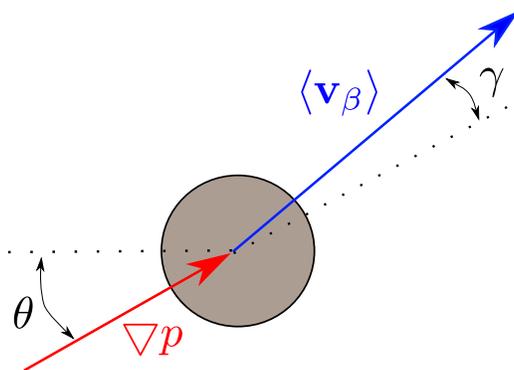
Figure 4.14: Explanatory sketch for the relation between mean pressure gradient and mean velocity field.

Using a linear correlation such as that shown in table 4.4 and figure 4.13, it is observed that in the low porosity case ($\varepsilon = 0.4$) the ratio can become very large indicating a strong deviation of the flow from the forcing direction, because of the strong constraint provided

ε	H_{11}/H_{22}	H_{11}/H_{33}	H_{22}/H_{33}
0.4	1.57	11.06	96.03
0.6	1.50	1.62	0.99
0.8	1.20	0.82	0.66

Table 4.4: Permeability components ratio for three values of the porosity. The permeability ratios here are given by the angular coefficients of the linear correlations displayed in figure 4.13.

by the inclusions. As the porosity increases, the ratio does not differ much from unity, which means that the deviation remains limited. It is simple to see that the deviation angle, for example in the (x_1, x_2) plane, satisfies the approximate relation

$$\tan \gamma = \frac{\left(1 - \dfrac{H_{11}}{H_{22}}\right) \tan \theta}{\dfrac{H_{11}}{H_{22}} + \tan^2 \theta},$$

so that for $\dfrac{H_{11}}{H_{22}}$ equal to, say, 1.5, the largest deviation remains always below $12°$ for any θ. It should however be kept in mind that trends based on these ratios are valid only as long as Darcy's law and linear correlations are acceptable. Cases exists for which such trends are violated; for example, a flow with $\theta = 45°$ and $\phi = 0°$ has deviation angle γ equal to zero, for whatever porosity. In this case H_{11}/H_{22} is equal to one and such a point is an outlier in the regression plots of figure 4.13.

4.6.2 Kriging interpolation method

The kriging approach is a linear interpolation/extrapolation method that aims to build a predictor field based on a set of observations $(\mathbf{x_i}, y(\mathbf{x_i}))$, for $i = 1, ..., n$.

The predictor $\hat{f}(\mathbf{x})$ is a sum of a trend function $t(\mathbf{x})$ and a Gaussian process error model $e(\mathbf{x})$:

$$\hat{f}(\mathbf{x}) = t(\mathbf{x}) + e(\mathbf{x}). \tag{4.4}$$

The aim of the error model is to make adjustments on the trend function so that, for any point of the sampling the predictor is exactly equal to the sample, i.e. $\hat{f}(\mathbf{x_i}) = y(\mathbf{x_i})$. This property represents one of the main qualities of this approach. In addition, when the model parameters are conveniently set, the trend function and the covariance model can take into account both smooth and steep variations in the data set.

The trend function defined here is based on a second order least-square regression, with the coefficients found from the solution of the associated linear system.

The Gaussian process error model has zero-mean and its covariance between two generic data-points, x_i and x_j, is written as

$$\text{Cov}(y(\mathbf{x_i}), y(\mathbf{x_j})) = c(\mathbf{x_i}, \mathbf{x_j})$$

The function $c(x^i, x^j)$ is a correlation model, based on the Matérn covariance model that reads:

$$c(\mathbf{x_i}, \mathbf{x_j}) = \sigma^2 \frac{2^{1-\nu}}{\Gamma(\nu)} \left(\frac{\sqrt{2\nu}|\mathbf{x_i} - \mathbf{x_j}|}{|\boldsymbol{\lambda}|} \right)^\nu K_\nu \left(\frac{\sqrt{2\nu}|\mathbf{x_i} - \mathbf{x_j}|}{|\boldsymbol{\lambda}|} \right), \quad (4.5)$$

where $K_\nu(.)$ is a modified Bessel function, $\Gamma(.)$ is the gamma function and the coefficient σ is an amplitude parameter. The parameters that can be used to tune the metamodel are the amplitude parameter σ, the exponent ν and the scale vector $\boldsymbol{\lambda}$. The kriging metamodel outputs can show different behaviours for different selections of the above three parameters and their setting is thus crucial. The amplitude parameter σ is chosen to be equal to 1; larger value lead to steeper gradients and undesirable local extrema around the data points. The vector $\boldsymbol{\lambda} = (\lambda_\theta, \lambda_\phi, \lambda_{Re_d}, \lambda_\varepsilon)$ is a scaling parameter for the distance $|\mathbf{x_i} - \mathbf{x_j}|$. In this study, through systematic variations of the parameters it is found that the choice $\boldsymbol{\lambda} = (1.2, 1, 1, 1)$ yields acceptable results; in particular, the weight along θ is mildly larger than in the other directions in order to obtain smoother metamodel surfaces in this direction. The exponent ν controls the covariance function and more especially its gradients. When $\nu = 1/2$ the covariance can be approximated by a negative exponential, $\exp(-\alpha x)$ and when ν goes to infinity it behaves as $\exp(-\alpha x^2)$. In the present study, the best (i.e. smoother) results are obtained for ν equal to 1.9. The above parameters have been chosen in order to avoid unphysical or unrealistic behaviour of the apparent permeability such as, for instance, negative values or steep, spurious local maxima/minima. The method above is implemented in OpenTURNS and full details are provided by Baudin et al. [13].

A procedure called k-fold, belonging to the class of cross-validation methods, has been used in order to prove the robustness of the metamodel. The k-fold method starts with the full database $S_n = (\mathbf{x_i}, \mathbf{y(x_i)})$, for $i = 1, ..., n$, split into two complementary set of size n_1 and n_2, such that $S_n = S_{n_1} \cup S_{n_2}$. Then, a new metamodel is built using only the points present in the set S_{n_1}. For the sake of clarity, the metamodel built with only the subset S_{n_1} will be called from now on $\hat{f}^{n_1}$, and the metamodel build with all the database will be indicated as $\hat{f}^n$. The idea now is to use the points in the set S_{n_2} as test, since they are essentially "new" for the metamodel $\hat{f}^{n_1}$. The division of the subset is performed picking points in a random way, and is repeated k times in order to rule out any possible "lucky" combination.

Thus, the metric used for the error computation is the following:

$$\xi_{cv} = \frac{1}{k\,n_2} \sum_{i=1}^{k} \sum_{j=1}^{n_2} (\hat{f}_i^{\ n}(x_j) - \hat{f}_i^{\ n_2}(x_j))^2,$$

quantifying the quadratic error between the original metamodel and the one built each time with a different set that belongs to different folds. The metric is also averaged over all the test points n_2 present in all the k folds. The relative mean error can be computed as:

$$E_{cv\%} = 100 \frac{\sqrt{\xi_{cv}}}{mean(|\hat{f}_i^{\ n}|)}.$$

In our case the number of points used to test the model n_2 is equal to $\sqrt{N} \approx 12$ as recommended for kriging metamodels Wang and Shan [156]. The number of folds has been varied from 5 to 25 and in all the cases tested the $E_{cv\%}$ has been found to decrease below 6% when we use at least 16 folds (which means leaving out 7 to 8 points from the metamodel construction), which is more than acceptable to prove that our kriging method is a robust approximation.

The metamodel provides a scalar function (for each term of the **H** tensor) defined in a four-dimensional space. In each of the following figures two parameters are fixed and the response surface is displayed as function of the remaining two, focussing on the H_{11} component. The other diagonal components of the apparent permeability tensor behave in
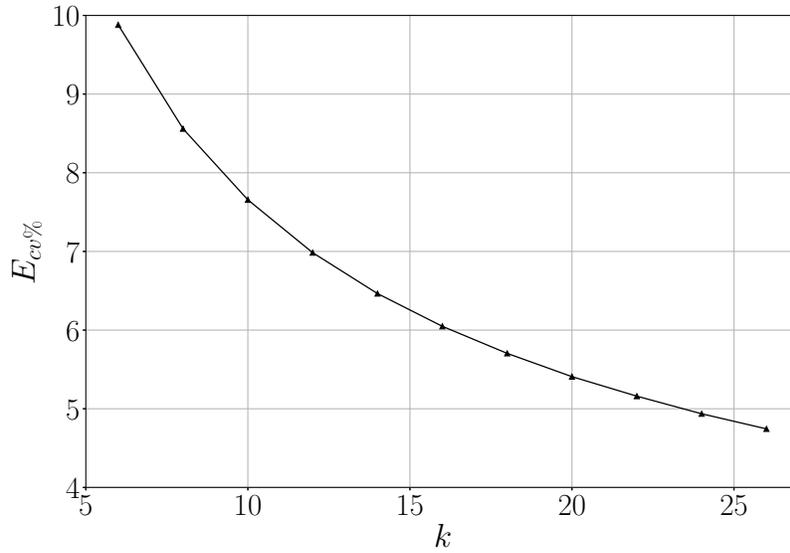
Figure 4.15: Relative mean error computed using the k-fold approach presented against the number of folds k used to divide the dataset
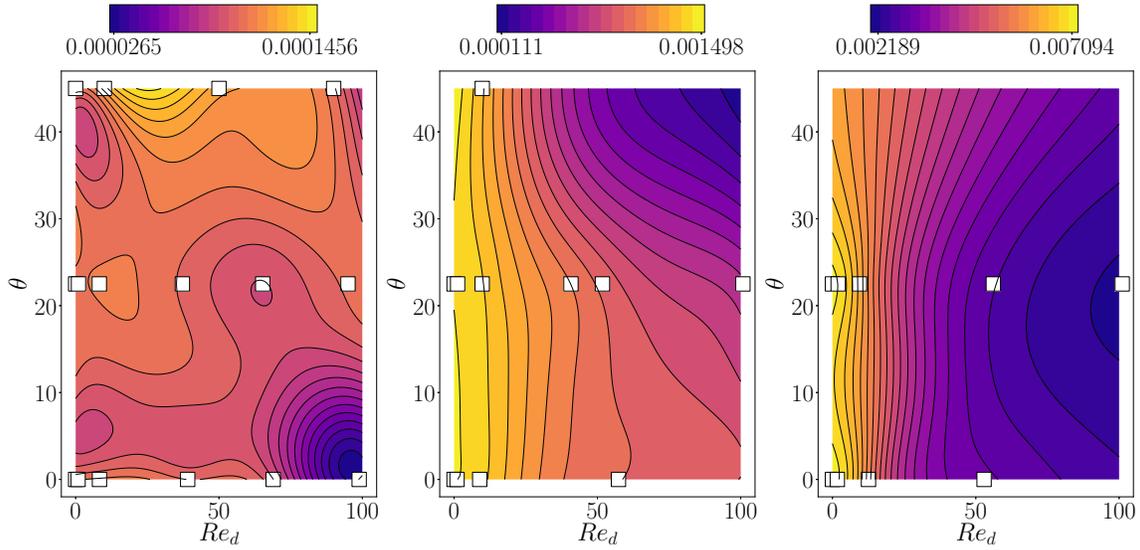
Figure 4.16: Response surfaces of H_{11} with $\phi = 0°$ for porosity $\varepsilon = 0.4, 0.6, 0.8$, from left to right.

a similar fashion and will not be shown for brevity. All the results of the metamodel are, however, available from the authors upon request.

In figure 4.16 the angle ϕ is fixed to zero, and the isolines display H_{11} as function of the angle θ and of the Reynolds number, Re_d, for three values of porosity. The white square symbols indicate the samples used to build the metamodel. The maximum value of each surface is always found for Re_d equal to zero and H_{11} typically decreases with Re_d, when the porosity is sufficiently large. As seen previously, for a porosity approximately greater or equal to 0.6 the variation of the apparent permeability with the angle θ is weak in this two-dimensional configuration. For the lowest porosity studied (left frame) the permeability has very small values and the isolines display an irregular behaviour; this is a feature common to all plots relative to the smaller value of ε, signaling that it is probably necessary, in this specific case, to insert additional sample points in building the response surfaces.

In figure 4.17 the parameter θ is set to $0°$ and the response surface is displayed in the $Re_d - \phi$ plane. As already indicated, the results confirm that an increase of the Reynolds number is generally associated to a decrease of the first diagonal component of the apparent permeability tensor. However, the H_{11} variations with respect to ϕ are more pronounced than those found with respect to θ and are due to a real three-dimensionalization of the flow. This conclusion remains to be verified in the lower porosity case (left frame) where the variations are very tiny and more irregular.

In figure 4.18 the Reynolds number is set to the inertial range value of 40 and the
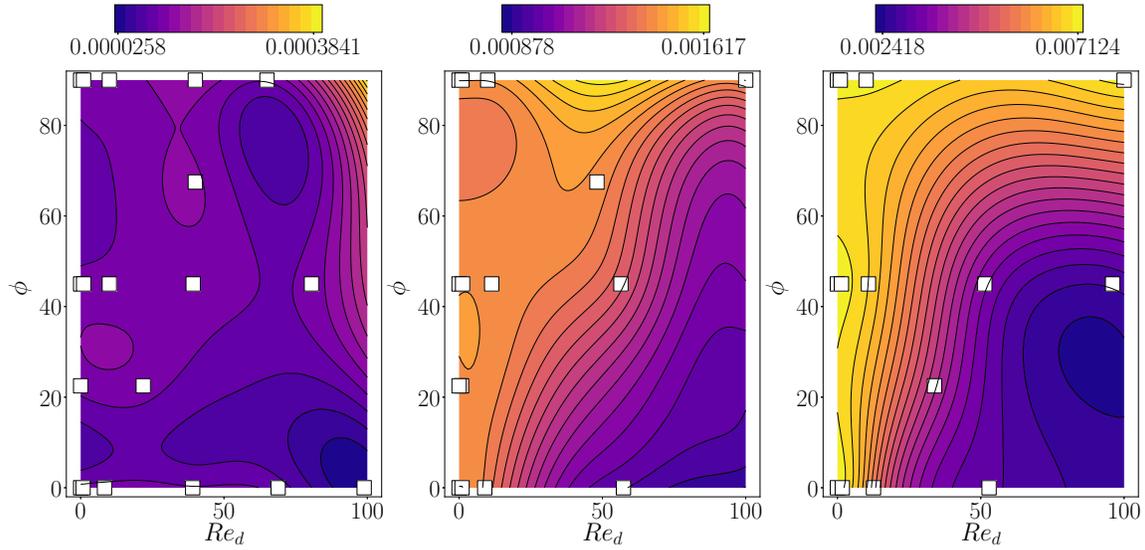
Figure 4.17: Response surfaces of H_{11} with $\theta = 0°$ for porosity $\varepsilon = 0.4, 0.6, 0.8$, from left to right.

response surface is displayed in the $\theta - \phi$ plane. For the two highest porosity values, 0.6 and 0.8, the results confirm that H_{11} has a much stronger dependence on ϕ than on θ, suggesting that the real test of permeability models must include three-dimensional effects. As seen earlier, the behaviour of the permeability when the porosity is low (left frame in the figure) is not intuitive, with a significant effect of the angle ϕ and a minor influence of θ. Again this occurs from the constraint provided to the flow by the inclusions, and from the occurrence of a large deviation γ in these cases.

The response surface is shown in the $Re_d - \varepsilon$ plane of figure 4.19 for three sets of $\theta - \phi$ angles. Here a significant effect of the porosity with respect to the Reynolds number is obervable. In fact the surface gradient is almost aligned with the porosity direction, i.e. a quasi- Reynolds independence is demonstrated in this plane, and the apparent permeability can change by one order of magnitude in the range of the analysed porosity.

Some relatively small Reynolds number effects are visible at porosity equal to 0.8, when the wake of the flow has more space to develop in the inertial regime. In the central figure the flow is aligned with the direction of the fibers and, as expected, it shows practically no dependence with respect to the Reynolds number.

The response surface analysis has confirmed the qualitative trends which had been reached earlier on the basis of a few selected flow cases, yielding at the same time much more detailed information on the behaviour of the apparent permeability with the parameters of the problem. The data base which has been built will be used in future work which will focus, via the VANS approach, on configurations for which neither the porosity nor the

99
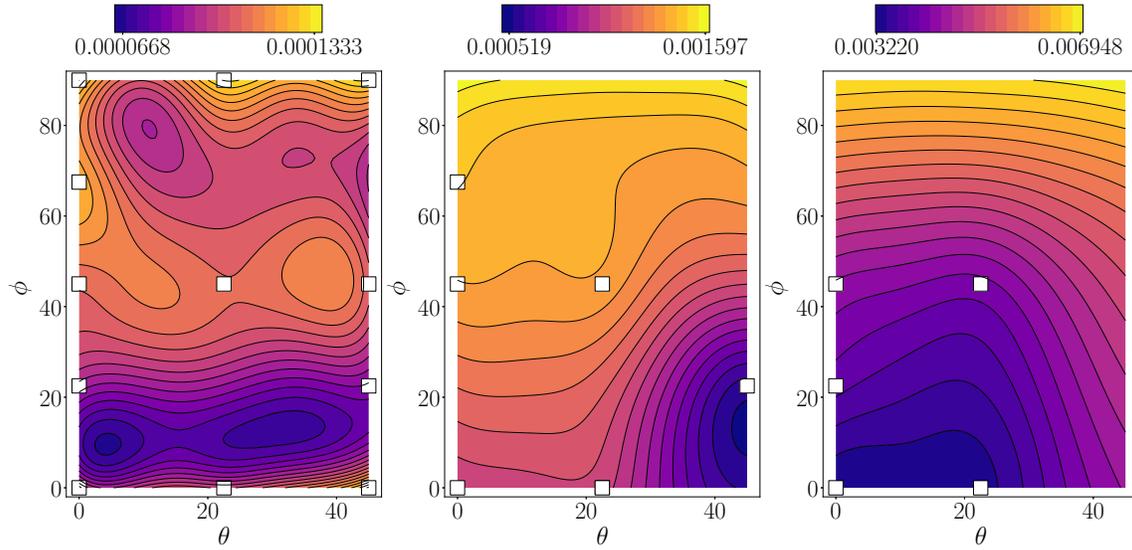
Figure 4.18: Response surfaces of H_{11} with $Re = 40$ for porosity $\varepsilon = 0.4, 0.6, 0.8$, from left to right.

local Reynolds number are constant in space or time.

For the sake of space, only the first diagonal component of the apparent permeability tensor has been discussed in detail; however, all components have been computed and the same conclusions can be drawn from the H_{22} or H_{33} component.

4.7 Concluding remarks

The components of the permeability tensor are essential ingredients for any solution of flow through anisotropic porous media. When the flow through the pores resents of significant acceleration effects, the permeability must be modified (it is then called *apparent*) by the presence of a second tensor, the Forchheimer tensor $\mathbf{F}$, defined by

$$\mathbf{F} = \mathbf{K}\mathbf{H}^{-1} - \mathbf{I}.$$

The permeability, $\mathbf{K}$, and the apparent permeability, $\mathbf{H}$, can be formally deduced by two closure problems which have been briefly recalled in section 4.2. The real obstacle to the solution of the problem for $\mathbf{H}$ is the need to know the microscopic velocity fields through the pores. We have solved for such fields in a unit cell (the REV), varying the forcing amplitude and direction, treating over one hundred different cases of flows through arrangements of parallel fibers. From this, we have thus been able to solve the linear system (4.2) for all the unknown elements of the intermediate tensor $\mathbf{M}$, from which, through averaging, we have
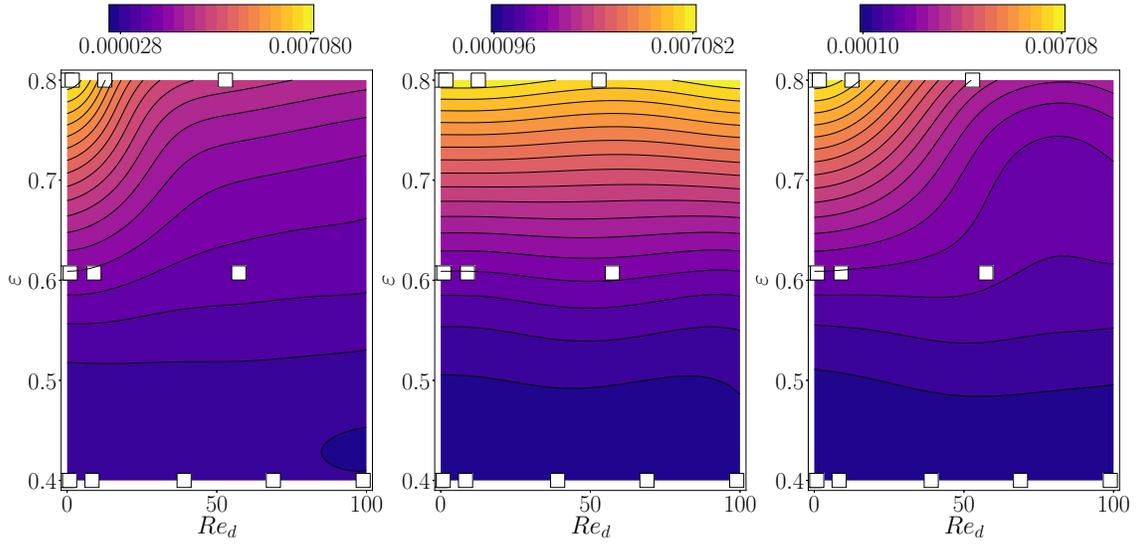
Figure 4.19: Response surface of H_{11}; in the left frame $\phi = \theta = 0$, in the centre frame $\phi = 90°$, $\theta = 0$ and on the right $\phi = 45°$, $\theta = 22.5°$.

computed the apparent permeability. Such a tensor is indispensable to evaluate accurately the drag force caused by the presence of the fibers, for a macroscopic solution of the flow on the basis of equations Whitaker [162] when inertial effects are present.

It has been found that the apparent permeability tensor is strongly diagonally dominant for whatever forcing direction and porosity, provided the local Reynolds number remains below a value approximately equal to 100; this results, which is a direct consequence of the transverse isotropy of the material which has been considered here, can be used to compute **H** rapidly, approximating it as a diagonal tensor.

Finally, a metamodel has been used to produce results so as to cover the whole space of parameters, and this has allowed the construction of a complete data base. This database can be used in simulations of porous media based on the VANS approach as we will show in the next chapter.

Chapter 5

VANS macroscopic applications

> *The first principle is that you must not fool yourself — and you are the easiest person to fool.*

> - 1974 Caltech commencement address, *Richard Feynman*

5.1 Introduction

In this chapter the macroscopic VANS equations are validated against a full microscopic DNS. Special attention is focused on the interface treatment using the penalization method. We also assess the effects of the permeability tensor metamodel within the algorithm. Computations are performed initially on the classical closed cavity configuration. The aim for the cavity problem is to validate the VANS approach and to show the importance of the interface treatment and the permeability metamodel. In the last part the Ercoftac periodic hill case is also tested. This open configuration aims to test the performance of porous coating as a device to reduce separated flow.

5.2 Closed cavity problem

The configuration chosen is the square closed cavity, depicted in figure 5.1. The cavity is square shaped with size L, the lateral and bottom walls are fixed and a constant velocity U^{top} is specified at the top side. On the front and back side we apply periodic boundary conditions since the three-dimensional simulation domain has a depth equal to ℓ. A rigid porous medium made by regularly arranged fibers is set at the bottom of the cavity, its vertical extension is equal to h. The *reference elementary volume* (REV) of the porous medium is a cubic cell of size ℓ with a cylinder, with diameter d, at its center. The porosity of the medium, ε, is equal to 0.8 and 50 fibers are assumed to be present in the cavity.

The configuration is summarized in the list below:
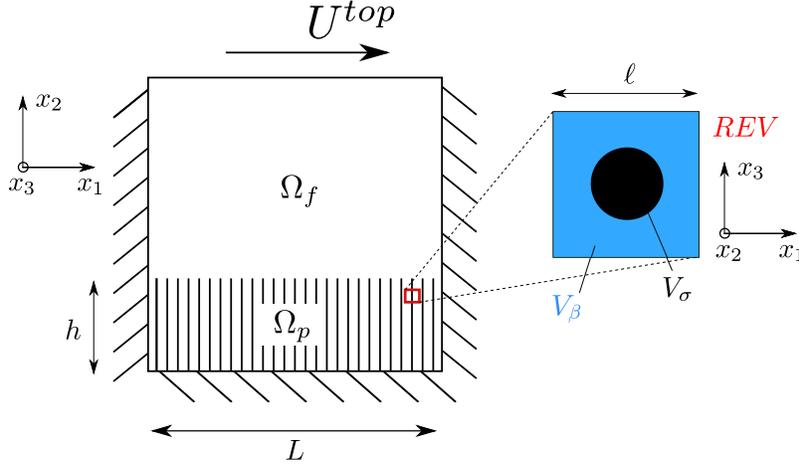
Figure 5.1: Schematics of the closed cavity 2D problem. The porous medium internal structure is depicted in the zoom on the right side in which the REV geometry is shown.

- L: side of the cavity, also the macroscopic length scale

- h: vertical extension of the fibers from the bottom of the cavity

- ℓ: side of the cubic REV, also the microscopic length scale

- d: diameter of the cylindrical fiber

- V_β: volume of the fluid inside the REV

- V_σ: volume of the solid inside the REV

- $\varepsilon = \dfrac{V_\beta}{V_\sigma + V_\beta} = \dfrac{\ell^3 - \ell\pi d^2/4}{\ell^3} = 1 - \pi\left(\dfrac{d}{2\ell}\right)^2$: porosity of the medium

- $\epsilon = \dfrac{\ell}{L}$: length scale ratio

- $Re = \dfrac{U^{top}L}{\nu_\beta}$: Reynolds number of the cavity

The overall domain has the size $L \times L \times \ell$ respectively in the x_1, x_2 and x_3 directions. The origin of our coordinate system is fixed at the bottom left corner of the cavity. This configuration and porous arrangement has been chosen to employ DNS data already available for this configuration (private communication with Zampogna and Bottaro [167]).

The length parameters for the specific case are:

- $h/L = 0.33$

- $\ell/L = 0.02$

- $\varepsilon = 0.8$

5.2.1 Microscopic approach with direct numerical simulations

In this approach the incompressible Navier-Stokes equations are solved in the three dimensional case (5.1). The problem is weakly three dimensional since only one REV along the x_3 axis is included and periodic boundary condition is imposed in this direction. This assumption seems fair since the Reynolds numbers tested are small and no 3D structures are expected in the flow. To complete the set of boundary conditions the no-slip condition is applied at the rigid walls and a prescribed horizontal velocity is imposed at the top wall (5.1). The subscript β means that the variables belong to the fluid phase, as usual. The mesh is fine enough to resolve the flow within the fibers and the spatial convergence is also ensured. The above setup is described by the set of equations:

$$
\begin{cases}
\dfrac{\partial \mathbf{v}_\beta}{\partial t} + \mathbf{v}_\beta \cdot \nabla \mathbf{v}_\beta = -\dfrac{1}{\rho_\beta} \nabla p_\beta + \nu_\beta \nabla^2 \mathbf{v}_\beta \\
\nabla \cdot \mathbf{v}_\beta = 0 \\
\mathbf{v}_\beta = 0 \qquad \text{on} \quad x_1 = 0, L \quad x_2 = 0 \\
\mathbf{v}_\beta = U^{top} \qquad \text{on} \quad x_2 = L \\
\mathbf{v}_\beta|_{x_3=0} = \mathbf{v}_\beta|_{x_3=\ell} \\
p_\beta|_{x_3=0} = p_\beta|_{x_3=\ell}
\end{cases}
\tag{5.1}
$$

Once the system (5.1) is solved, the microscopic fields (velocity and pressure) inside the porous medium are averaged with the operator (5.2) in order to get the homogenized macroscopic field $\langle \mathbf{v}_\beta \rangle^\beta$ and $\langle p_\beta \rangle^\beta$.

$$
\langle \psi_\beta \rangle^\beta = \frac{1}{V_\beta} \int_{V_\beta} \psi_\beta(\mathbf{x}) dV_\beta.
\tag{5.2}
$$

The operator (5.2) has been applied through the whole porous domain using a REV with dimension $\ell \times \ell \times \ell$. It means that the centroid of the REV, in which the average operation is performed, spans all the porous domain extension. It should be noted that in our case we have not taken into account any filter function inside the definition of the averaged operator (5.2) used to make tha average of the DNS fields. It should be noted that the averaging procedure gives a two dimensional averaged field as a result, the only non zero values are in the x_1 and x_2 directions. This is due to the symmetry of velocity

and pressure in the x_3 direction that returns zero averaged field as a result of the averaging operation (5.2).

5.2.2   Macroscopic approach through VANS

The same problem is solved using the VANS approach. The set of equations used are the incompressible Volume Averaged Navier-Stokes equations in the two dimensional case with a Darcy-Forchheimer closure (5.3). The derivation of this set of equation has been already discussed in chapter 2 and is presented here for completeness:

$$
\begin{cases}
\dfrac{\partial \langle \mathbf{v}_\beta \rangle^\beta}{\partial t} + \dfrac{1}{\varepsilon} \nabla \cdot \left[\varepsilon \langle \mathbf{v}_\beta \rangle^\beta \langle \mathbf{v}_\beta \rangle^\beta \right] = -\dfrac{1}{\rho_\beta} \nabla \langle p_\beta \rangle^\beta + \nu_\beta \nabla^2 \langle \mathbf{v}_\beta \rangle^\beta \\
\qquad\qquad\qquad\qquad - \nu_\beta \varepsilon \mathbf{H}^{-1} \langle \mathbf{v}_\beta \rangle^\beta + \dfrac{\nu_\beta}{\varepsilon} \nabla \varepsilon \cdot \nabla \langle \mathbf{v}_\beta \rangle^\beta + \dfrac{\nu_\beta}{\varepsilon} \langle \mathbf{v}_\beta \rangle^\beta \nabla^2 \varepsilon \\
\nabla \cdot \left(\varepsilon \langle \mathbf{v}_\beta \rangle^\beta \right) = 0 \\
\langle \mathbf{v}_\beta \rangle = 0 \qquad \text{at} \quad x_1 = 0, L \quad x_2 = 0 \\
\langle \mathbf{v}_\beta \rangle = U^{top} \qquad \text{at} \quad x_2 = L
\end{cases}
\tag{5.3}
$$

The boundary conditions are the same as the DNS approach except for the x_3 dimension that in this case is neglected since the homogenized problem is already two dimensional. The solution of system (5.3) gives directly the averaged velocity and pressure fields to be compared to the averaged DNS fields.

Interface treatment

The penalization method (or one domain approach) has been chosen to treat the interface of the porous medium. The method has been already discussed in section 2.5 of chapter 2 but here some technical aspect are further discussed. In order to use the so called penalization method the porosity field and the effective permeability have to be defined in all the domain. In the free fluid the porosity is, of course, unitary and the effective permeability infinite. With such a numerical values the Navier-Stokes system (5.1) is retrieved from the system (5.3) after some simplifications. In the deep porous medium the porosity is constant and set equal to 0.8. The effective permeability is also constant and the components of the tensor have been taken from a posteriori computation of the homogenized-DNS problem. This procedure involves the inversion of the Darcy system $\langle \mathbf{v}_\beta \rangle = \nu_\beta \varepsilon \mathbf{H}^{-1} \cdot \nabla \langle p_\beta \rangle^\beta$. The numerical values for $\mathbf{H}$ are represented in table 5.1.

The apparent permeability tensor **H** is also diagonal. This is consistent with the result in chapter 4 in low pore Reynolds number, as a matter of fact in the cavity, the pore Reynolds number is always below 5 for both cases tested.

It is difficult to define how to connect the different values for the free fluid and the porous media part through the interface. However, the exact profile for the porosity field can be computed knowing the geometry of the medium. In this case the porous medium is made of cylindrical fibers in a regular arrangement. The relationship between the porosity in the deep medium ε, the size of the REV ℓ and the cylinder diameter d is:

$$\left(\frac{d}{\ell}\right)^2 = \frac{4}{\pi}(1-\varepsilon)$$

With the above relationship it is possible to define the porosity as a function of the vertical coordinate $x_2 = y$:

$$\varepsilon(y) = \begin{cases} 1 & y \geqslant (y_{itf} + \ell/2) \\ \varepsilon + \dfrac{1-\varepsilon}{\ell}[y-(y_{itf}-\ell/2)] & (y_{itf}-\ell/2) < y < (y_{itf}+\ell/2) \\ \varepsilon & y \leqslant (y_{itf}-\ell/2) \end{cases} \qquad (5.4)$$

In the above expression the interface location y_{itf} is equal to h. The same expression has been used for the effective permeability field. In equation (5.5) the inverse of the effective permeability is used.

The H_{ii} term in equation (5.5) refers to the effective permeability components of the deep medium, reported in table 5.1.

$$H_{ii}^{-1}(y) = \begin{cases} 0 & y \geqslant (y_{itf}+\ell/2) \\ H_{ii}^{-1} - \dfrac{H_{ii}^{-1}}{\ell}[y-(y_{itf}-\ell/2)] & (y_{itf}-\ell/2) < y < (y_{itf}+\ell/2) \\ H_{ii}^{-1} & y \leqslant (y_{itf}-\ell/2) \end{cases} \qquad (5.5)$$

The data analyzed in chapter 4 suggests that the components of **H** are mostly driven by the porosity effect so it is fair to suppose that the same variability should be used for both the porosity and the permeability fields. This assumption justifies the choice of the same formulation for the interface treatment for the two different fields.

	$H_{11} = H_{22}$	H_{33}
$Re = 100$	$2.63 \cdot 10^{-2}$	$5.49 \cdot 10^{-2}$
$Re = 1000$	$2.65 \cdot 10^{-2}$	$5.63 \cdot 10^{-2}$

Table 5.1: Apparent permeability values from table 1 in Zampogna and Bottaro [167]

5.2.3   Cavity $Re = 100$ comparison

This section presents the comparison between the microscopic and macroscopic approaches for the cavity at $Re = 100$. Pictures 5.2 and 5.3 show the pressure gradient and the velocity fields for the two different approaches.

Each field is made non-dimensional using the macroscopic length and the velocity on the top of the cavity:

$$u^* = u/U^{top}, \qquad v^* = v/U^{top}$$
$$\frac{\partial p}{\partial x}^* = \frac{2\,L}{\rho_\beta (U^{top})^2}\,\frac{\partial p}{\partial x}, \qquad \frac{\partial p}{\partial y}^* = \frac{2\,L}{\rho_\beta (U^{top})^2}\,\frac{\partial p}{\partial y}$$

The DNS approach is used as reference case for the comparison. At Reynolds number equal to 100 a good agreement is found for both the velocities and pressure gradients fields.
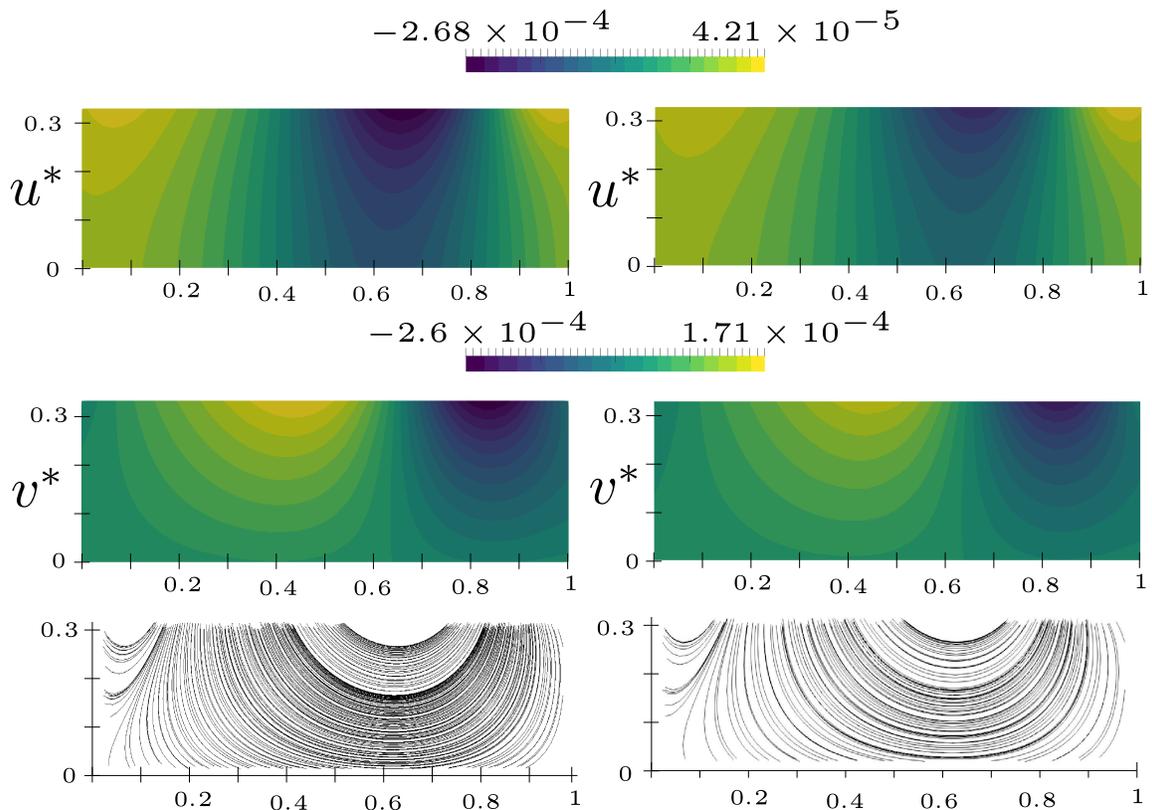
Figure 5.2: Left: VANS approach. Right: Homogenized DNS approach. The figures show, from top to bottom, the horizontal velocity the vertical velocity and the streamlines inside the porous domain Ω_p
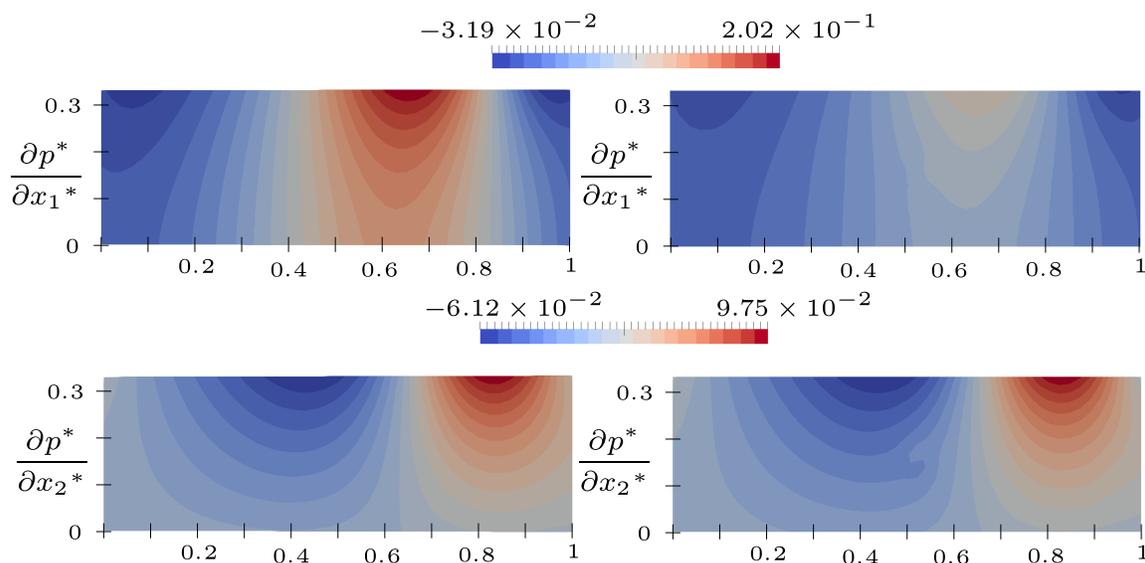
Figure 5.3: Left: VANS approach. Right: Homogenized DNS approach. The figures show, from top to bottom, the horizontal and the vertical component of the pressure gradient inside the porous domain Ω_p

The contours and the location of the local minima and maxima are the same for the two approaches. If we look at the numerical values, for some fields the relative errors are not negligible; however, they are in mean always below 10%. Also the streamlines inside the porous domain is in good agreement with the DNS data. Some differences between the two models have to expected since in the VANS approach the micro-scale flow behavior is modeled. This means that some of the details that the full DNS is able to retain, are lost in the macroscopic approach.

5.2.4 Cavity $Re = 1000$ comparison

The same case and comparison has been done also for a Reynolds number equal to $Re = 1000$. For this case the same conclusion as the previous case are confirmed. Some of the relative errors are even smaller compared to the previous Reynolds number case. This support the robustness of our model in this range of Reynolds numbers. These two solutions of the cavity problem shown that varying the permeability and the porosity in a linear manner through the interface is an acceptable choice when using the penalization method. Compared to previous case the flow field now presents two different recirculations inside the porous medium domain, increasing the complexity of the dynamics inside the porous medium. Looking at the zone around the porous interface in figures 5.6 and 5.7, the differences between the DNS and homogenized approach are clear. The DNS shows oscillations

in both the vertical and horizontal velocity components due to the presence of the fibers, on the contrary in the homogenized approach this local oscillations are smoothed out by the averaging operation. However, these oscillations have a very small amplitude and to make them visible the range of values plotted needs to be modified (bottom pictures of figures 5.6 and 5.7).
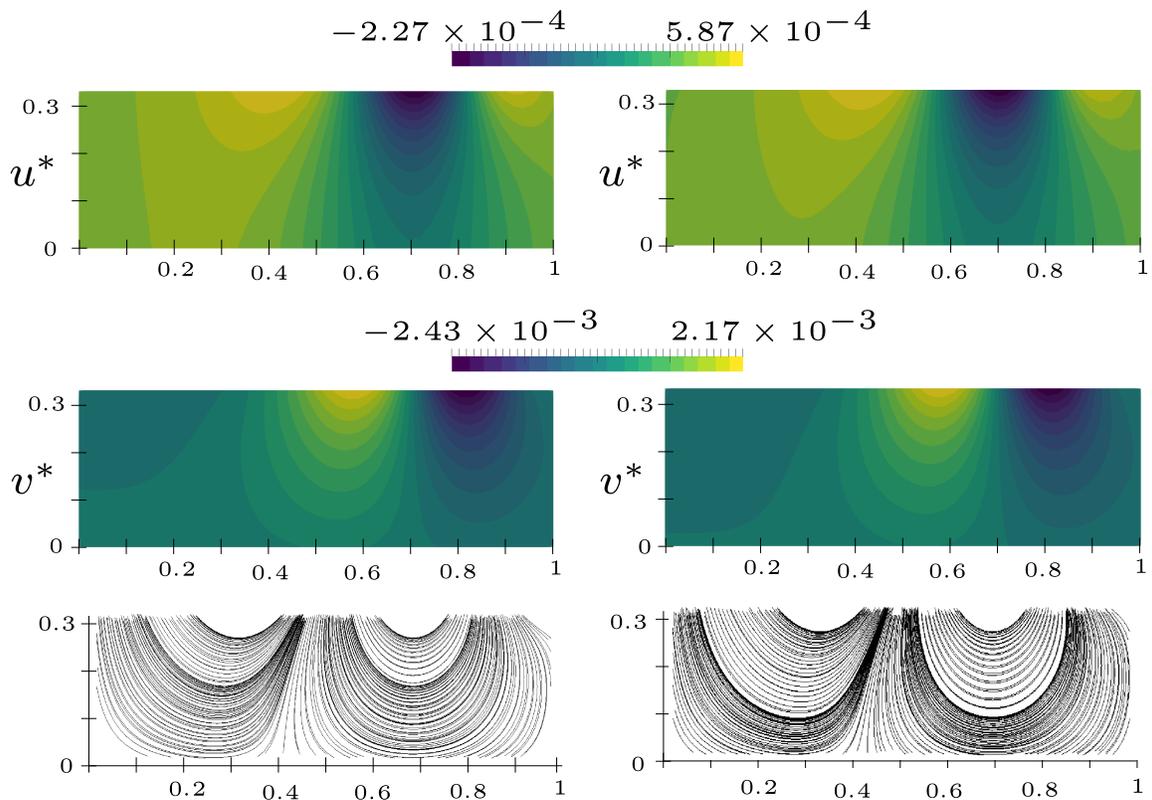
Figure 5.4: Left: VANS approach. Right: Homogenized DNS approach. The figures show, from top to bottom, the horizontal velocity the vertical velocity and the streamlines inside the porous domain Ω_p
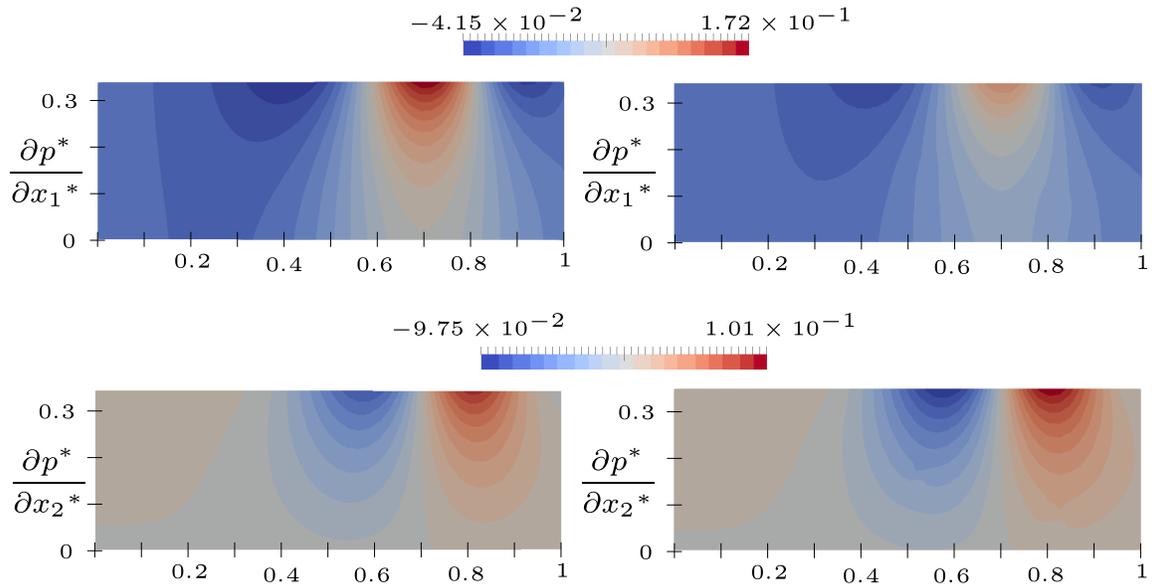
Figure 5.5: Left: VANS approach. Right: Homogenized DNS approach. The figures show, from top to bottom, the horizontal and the vertical component of the pressure gradient inside the porous domain Ω_p

5.2.5 Cavity $Re = 5000$ using H metamodel

In our previous simulations the metamodel for the effective permeability has not been applied. The metamodel in chapter 4 was built for a porous medium made of staggered cylinders. So it would not be applicable when the porous medium is made by regular arranged cylinders.

In order to test how the effective permeability variation would impact our model we show the solution for another test case. In the same cavity geometry as before the system (5.3) is solved with or without the kriging metamodel for the effective permeability.

We have observed that at low pore Reynolds number the effective permeability is practically not sensitive to variations of flow direction and/or magnitude[1]. For this reason the Reynolds number has been also increased to 5000, still in the stationary regime but near the transition limit (Yih-Ferng et al. [166]).

Figure 5.8 shows the velocity and permeability profiles for a sample cut made at the center of the cavity at $x = 0.5\,L$. It is clear that the macroscopic velocity is not affected by the different treatment of the permeability, as a matter of fact the two velocities can be superposed almost exactly. However, the inverse of the effective permeability component shows some differences. At the interface it is possible to see also how the trend of the

---

[1]see figures 4.10, 4.10 and 4.10 in chapter 4.
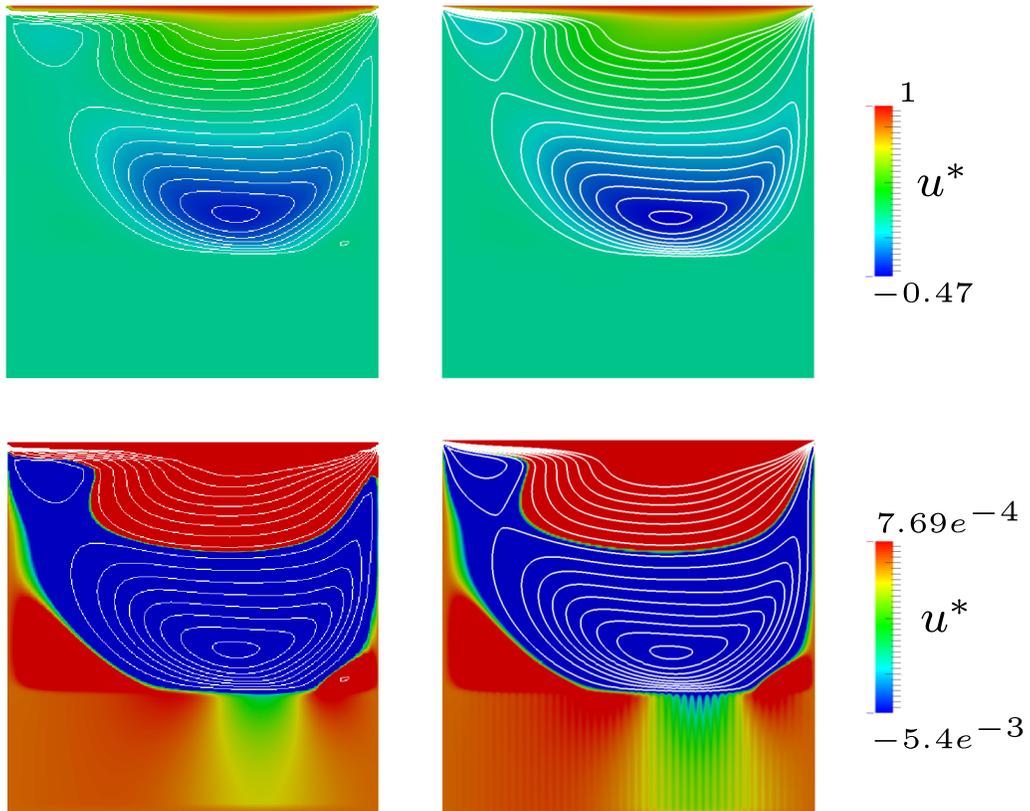
Figure 5.6: Left: VANS approach. Right: Homogenized DNS approach. The figures show, the horizontal velocity component in the whole domain. In the bottom figures the range of values plotted has been reduced to better show the flow structure inside the fibers in the DNS case.
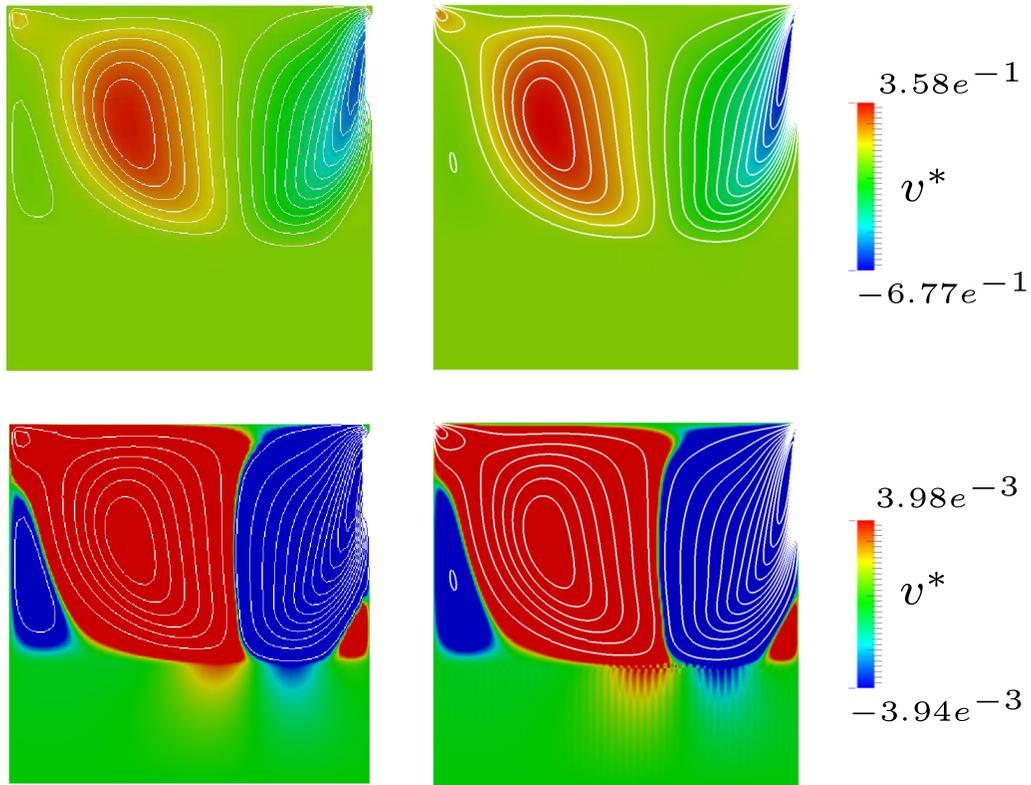
Figure 5.7: Left: VANS approach. Right: Homogenized DNS approach. The figures show, the vertical velocity component in the whole domain. In the bottom figures the range of values plotted has been reduced to better show the flow structure inside the fibers in the DNS case.
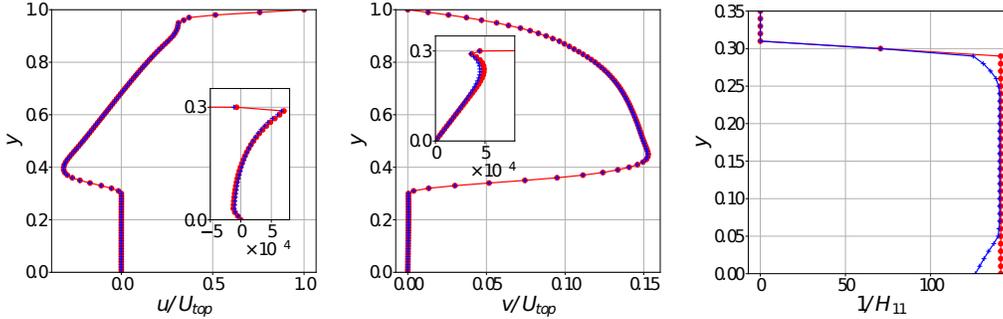
Figure 5.8: Left: horizontal velocity component. Center: vertical velocity component. Right: Effective permeability 11 component. The three fields have been sampled at the center of the cavity, $x_1 = 0.5\,L$. The blue line represents the solution for the system (5.3) with the kriging metamodel for the effective permeability, the red line is the solution of the same system with the model switched off.

two different treatments look like at the interface. The permeability starts to increase at a deeper vertical position than the case without metamodel. This is caused by the vertical angle ϕ that is near $90°$ at that point because of the fluid penetration. The analysis made in chapter 4 concludes that the permeability increases when the angle ϕ increases. However the value of the permeability deep in the medium is almost the same. In any case even if there are some differences in the permeability profiles it seems not to affect the average velocities.

The fact that with the kriging metamodel the same linear profile as equation (5.5) is retrieved is another confirmation that the linear variation of the permeability is acceptable.

5.3   Separated flow between hills

In chapter 1 we have presented some flow examples where a porous media layer in the leeward side of a bluff body can reduce the separation extension. In order to test the effectiveness of our model to make predictions in this sense, the flow over periodically arranged hills has been chosen as test problem. This configuration has already been investigated experimentally and numerically and is a classical CFD problem, now standardized by the ERCOFTAC committee. It is used as a benchmark case to investigate the ability of DNS, RANS and LES models to resolve separation from a curved geometry. The flow field features a large separation bubble caused by the curved surface of the hill and a natural reattachment in the flat part between the two hills crests. The flow is assumed to be periodic and two dimensional, at the Reynolds number tested. Numerous DNS and LES works can be found in the literature with Reynolds numbers up to 10000 (Chang et al. [37], Breuer et al. [22] [23], Almeida et al. [4] and Temmerman and Leschziner [150]). This problem has

been studied with two main objectives: to test the modeling and simulation issue related to our VANS solver and the physical capacity to reproduce the flow field behavior. Our idea is to extend the hill profile with a porous media layer and assess how the separation bubble is modified by the layer presence. We have tested a small Reynolds number case in the laminar regime. The problem has been chosen especially for the possibility to future extend the study towards higher Reynolds numbers since a lot of data can be found in the literature to validate the results.

5.3.1   Geometry and conditions

The geometry of the problem is depicted in figure 5.9. It is two dimensional since the Reynolds number considered is in the laminar regime and the flow does not present any three dimensional characteristics in this range. The dimension of the hill crest and extensions are also showed in the same pictures being rendered adimensional with the hill crest height. The chosen dimensions of our setup are: $L_x = 9.0$, $L_y = 3.036$ and $h = 1$ where x, y, z are the streamwise, wall-normal and spanwise direction, respectively. We solve the flow inside of a single streamwise periodic segment and thus cover solely one complete hill region from crest to crest. Between one hill and the next one there is a flat plate region of extension $5h$. The pressure-induced separation takes place from the first hill curved surface and reattachment is observed at the flat plate part between the two hills.

The hills profile is described by a polynomial parametric curve function of the streamwise direction $y_{hill} = f(x)$. The specific coefficients and definition can be found in Almeida et al. [4]. This geometry is also named **base** case in the following text.

The problem is discretized using the finite volume method implemented in OpenFoam and the mesh used is shown in figure 5.9. The mesh is purely made of hexahedral cells and counts 25000 elements in the two dimensional version. It is possible to download it at `https://turbmodels.larc.nasa.gov/Other_LES_Data/2dhill_periodic.html`. The resolution has been already validated in DNS and LES computations so it has not been further investigated here.
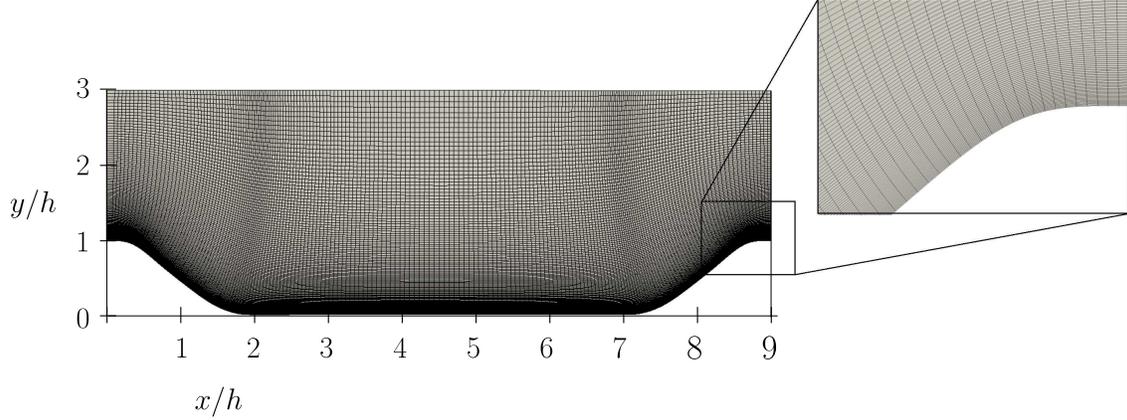
Figure 5.9: Domain of the problem and mesh used to discretize it. On the right side there is an enlargement of the zone on the hill curvature.

The inlet and the outlet patches are connected with a periodic boundary condition; at the hill and flat plate surface the no-slip condition is imposed and finally at the top of the domain a free slip condition is used. The numerical setup for the numerical scheme and linear solvers is the same as the DNS simulations in chapter 4, paragraph 4.3.2.

The equations solved are a slightly modified version of the VANS system (5.3) in which the constant macroscopic pressure gradient ($\mathbf{g}$) is introduced as a source term in the momentum equation:

$$
\begin{cases}
\dfrac{\partial \langle \mathbf{v}_\beta \rangle^\beta}{\partial t} + \dfrac{1}{\varepsilon} \nabla \cdot \left[\varepsilon \langle \mathbf{v}_\beta \rangle^\beta \langle \mathbf{v}_\beta \rangle^\beta \right] = -\dfrac{1}{\rho_\beta} \nabla \langle p_\beta \rangle^\beta + \nu_\beta \nabla^2 \langle \mathbf{v}_\beta \rangle^\beta \\
\qquad\qquad\qquad\qquad - \nu_\beta \varepsilon \mathbf{H}^{-1} \langle \mathbf{v}_\beta \rangle^\beta + \dfrac{\nu_\beta}{\varepsilon} \nabla \varepsilon \cdot \nabla \langle \mathbf{v}_\beta \rangle^\beta + \dfrac{\nu_\beta}{\varepsilon} \langle \mathbf{v}_\beta \rangle^\beta \nabla^2 \varepsilon - \mathbf{g} \\
\nabla \cdot \left(\varepsilon \langle \mathbf{v}_\beta \rangle^\beta \right) = 0 \\
\langle \mathbf{v}_\beta \rangle = 0 \qquad \text{at hill wall} \\
\dfrac{\partial u}{\partial y} = 0 \qquad \text{at } y = 3.035\,h \\
\langle \mathbf{v}_\beta \rangle |_{x_1=0} = \langle \mathbf{v}_\beta \rangle |_{x_1=9h} \\
\langle \mathbf{v}_\beta \rangle |_{x_1=0} = \langle \mathbf{v}_\beta \rangle |_{x_1=9h}
\end{cases}
\tag{5.6}
$$

In the system (5.6) the flow is driven by the source term $\mathbf{g}$ and the Reynolds number is computed a posteriori in the following manner:

$$
R_e = \frac{U_b h}{\nu},
$$

where U_b is the velocity in the top left corner of the domain, just above the first hill.

115

The treatment for the porosity is the same as equation (5.4) where in this case the interface height y_{itf} is described by two different profiles. The first one, called **external**, is the same hill profile translated to the right by a length equal to $0.2\,h$ in the streamwise direction. This setup is used to test the case of a porous media layer on the external part of the hill. In this case the hill geometry is modified.

In the second case the interface profile y_{itf} is exactly the hill profile at the same position and the solid part of the hill is translated in the upstream direction by $0.2\,h$. In this setup, denoted **internal**, the porous media layer has been inserted on the "interior" of the hill leeward side. It means that the total geometrical extension of the hill plus the porous media layer is the same as the base case described by y_{hill}.

The porous media layer has the same geometry of the one described in 4, a series of cylinders in staggered arrangement. The cylinders are then arranged on the leeward side of the hill and they are aligned with the wall normal direction. Although their extension is not uniform, the line that goes through all the cylinders lid describe the curves y_{itf} **external** and **internal**.

The two different porosity field arrangements are depicted in figure 5.10. Where the porosity deep inside the medium, shown in green, is equal to 0.8 and the exterior porosity field is equal to 1 and is shown in purple.
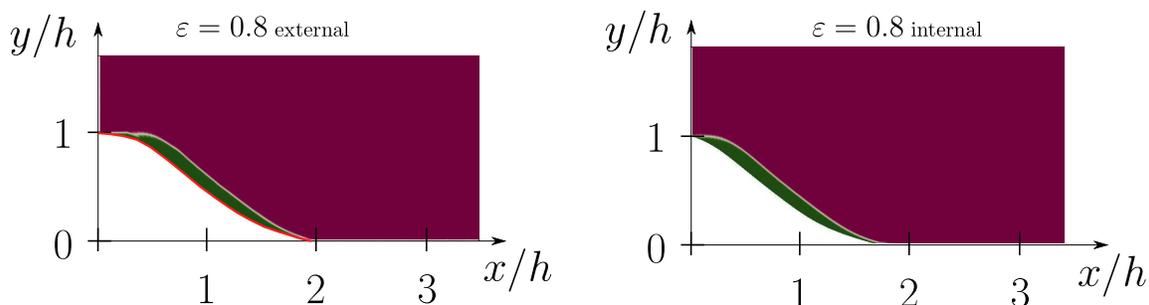
Figure 5.10: Porosity field in the leeward side of the first hill for the two different cases *external* and *internal*. The porosity in the deep medium is equal to 0.8 and is colored in green, instead the porosity in the free fluid is equal to 1 and it is colored in purple. On the left case, the *external* one, the red line describes the hill profile of the base case and the white line describes the porous media interface. For the *internal* case on the right the base hill profile and the porous media interface are the same one, and they are depicted in white.

On figure 5.10 the left picture shows the case named *external*, the red line indicates the hill profile in the base case and the porous media layer is put on top of it and the white line indicates the porous media interface y_{itf}. The right picture in figure 5.10 instead shows the configuration in the case named *internal*. For this case the porous media interface line y_{itf} is the same as the hill profile in the base case and is depicted in white.

To summarize the two different cases differ for the position on the porous media interface that is equal to the hill profile translated in the positive streamwise direction (case *external*) or in the negative streamwise direction (case *internal*). The translation has the same extension of $0.2\,h$ for each case.

The interface has also been treated with the linear smoothing function (5.4).

The permeability tensor components are then evaluated with the kriging metamodel in the zone where the porosity field is different from one.

5.3.2   Comparison between smooth and porous leeward side of the hill

The above geometrical setup has been studied in the stable laminar regime. In this case the source term is equal to $\mathbf{g} = (0.5\,10^{-8}, \quad 0, \quad 0)$ that results in a Reynolds number equal to 83. For all the cases the recirculation bubble has been measured in its vertical and horizontal extension. The horizontal extension L_R is defined as the first streamwise point in which a sampled velocity profile shows only positive streamwise velocities. The vertical extension has been measured at $x = 4.5$ that is the mean extension of the domain. Table 5.2 collects these results. Looking at the results the porous media has a negative effect in both L_R and $h_{x=4.5}$. For the case *external* the geometry of the hill is modified by the porous medium and the leeward side is pushed downstream, so it is not surprising that the recirculation extension is pushed downstream. A similar negative effects can be found also for the *internal*. This is in line with some observation made by Jimenez et al. [83] and Gomez-de Segura et al. [68] in which they argue that some configuration of the porous surfaces characteristic (porosity and permeability) can produce negatives effects. The last case analyses the flow for a completely permeable hill obstacle, this means that the fluid can pass through the overall hill geometry. Also in this case the length and the height of the recirculation is increased, with similar values as the previous cases.

case	L_R	$h_{x=4.5}$
impermeable wall	5.6	0.27
external	5.95	0.33
internal	5.8	0.31
completely permeable	5.7	0.3

Table 5.2: Recirculation bubble streamwise extension L_R and vertical extension at $x = 4.5$ for the three porous media configurations.

The streamlines in figure 5.12 show the shape of the recirculation bubble for the four cases. It can be seen that they look very similar and as a matter of fact the differences described in table 5.2 are within 5% from the base case without the porous layer. It can be noted that for the completely permeable hill obstacle the flow field show a complex behavior inside the porous domain. The streamlines at the inlet are almost horizontal because the

fluid is forced to flow in this direction but it soon deviates upwards due to the permeability of the fibrous porous media that is higher in the vertical direction. In figure 5.11 the local velocity fields are analyzed. The sampled velocities at $x = 1$ seems very different because the geometry in that point is not the same. If we look at the horizontal velocity gradients, they are similar. Some differences can be observed for the vertical velocities. The *internal* case presents smaller vertical velocities than the other two cases at $x = 1$, close to the detachment point. The situation is inverted further downstream at $x = 2$ and the three profiles collapse onto one another at $x = 3$. This different local behaviors can be used for example in situations were the vertical exchange of momentum has to enhanced for examples in aquatics plant applications where the nutrient exchange has to be optimized.
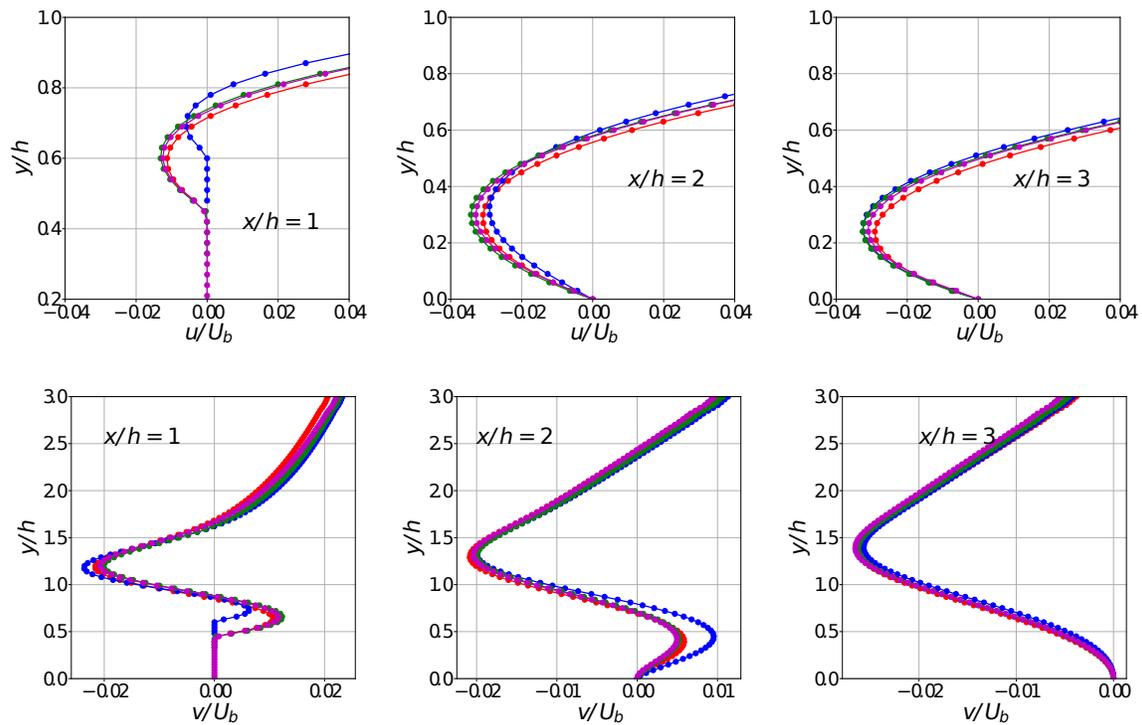
Figure 5.11: The top three figures show the horizontal velocity profile for the sampled cut at $x = 1$, $x = 2$ and $x = 3$ respectively from left to right. The bottom figures follow the same patterns but instead shows the vertical velocity profile. The red line is the **impermeable wall** case the blue line is the **external case**, the green line is the **internal** case and the magenta line is the **completely porous** case.
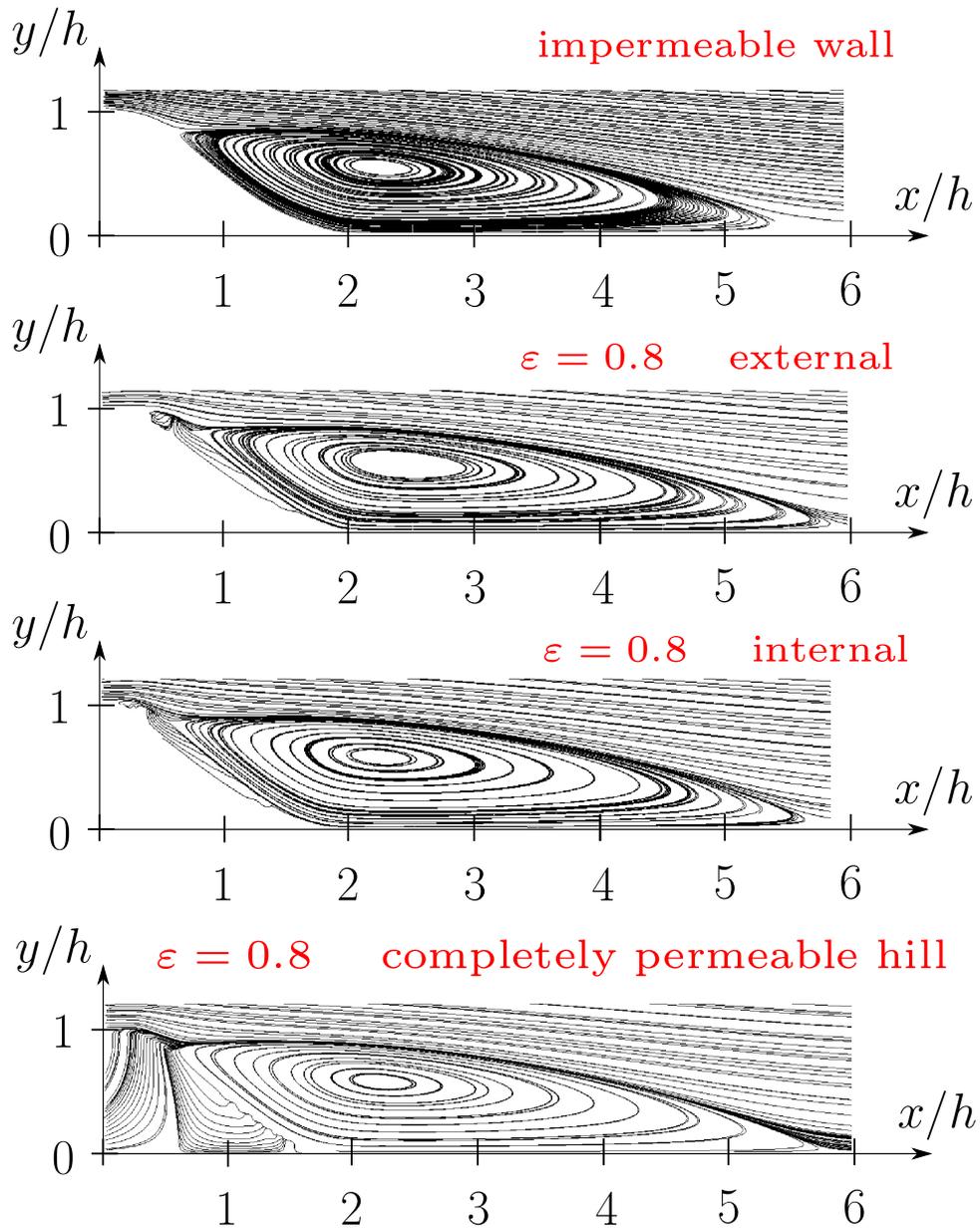
Figure 5.12: Streamlines for the three cases tested. The top picture shows the case without the porous medium. The two central pictures show the cases where the porous media layer is put on the external and internal part of the hill base profile. The bottom picture shows the streamlines for a completely porous hill obstacle.

5.4 Conclusions

In the chapter we have shown how the VANS equations derived in chapter 2 can be used to describe the averaged macroscopic field for rigid porous medium. We have also shown how the interface should be treated in order to retrieve good results. Direct comparison with DNS data show that the linear smoothing of the porosity field and of the effective permeability field are necessary. We have also shown that using the metamodel developed for **H** produces the same smoothing for the interface. However it should be noted that the definition of the interface profile of the porosity and permeability if directly dependent of the side of the REV chosen, in our case, ℓ. In our case the choice is dictated from the regular and ordered arrangement of the porous structure but, other choices are possible and this modifications will modify the slope of the interface functions. Finally the periodic hill application demonstrate that our homogenized solver can be used easily as a tool to test and measure porous coating and their effectiveness. For the porous characteristics used in our study it has been found that the porous medium has negative effects for separation. But our focus was on the validation and easiness-to-use of our macroscopic model, further investigations are required to understand the physics under this negative effect. With this tool it is now possible to extensively study porous media coatings in order to find the optimal characteristics with respect to various objectives.

Chapter 6

Conclusions, recommendations and discussions

The question of whether Machines Can Think... is about as relevant as the question of whether Submarines Can Swim.

- , Edsger Dijkstra

6.1 Main conclusions

In chapter 1 we have reviewed the latest advances and open questions present in the literature. The same chapter is an attempt to produce a new and improved basis from which many researchers could find and/or explore new research paths and ideas. In this final chapter we list the main results and conclusions that can be drawn from the present work.

The volume average method has been detailed in its key assumptions. The mathematical procedure needed to find the macroscopic equations, and the closure problem, has also been presented. Also some of the most notable new contributions to the method have been included in the discussion.

The sensitivity analysis shows that the VANS approach is the less sensitive one with respect to variations in the base flow. Also, the stability results agree reasonably with the experimental results. One of the possible drawbacks in the use of the VANS model is the necessity to compute the effective permeability tensor $\mathbf{H}$. The computational cost and the difficulties to compute the components of the permeability tensor are the main reason that have taken toward the development of a metamodel for the tensor $\mathbf{H}$ in chapter 4.

Opposed to the results in the work of Lasseux et al. [93] for rectangular fibers, our computed effective permeability tensor for circular fibers is, with a good approximation, diagonal. It means that the geometrical shape of the porous structure is very important for

the characterization of the tensor structure. A possible generalization of different porous structures is shown in Pauthenet et al. [124] even though further investigations on the non diagonal terms are needed.

We have also shown that the 3D effects can be very important in changing the permeability tensor components. In our data analysis, in chapter 4, we have shown that the angle ϕ^1 has a large influence in the tensor $\mathbf{H}$ components, especially in the inertia regime. The same angle ϕ makes the flow three dimensional and it bends the fluid path along the fiber axis. This process translates into a non-zero deviation angle γ in the fiber axis direction.

In chapter 4 [98] we have shown that the $\mathbf{H}$ metamodel has been developed up to a Reynolds number equal to 100. This limit has been derived from the data and it was not fixed a priori. To estimate this limit we have checked the direct comparison of F^m and F^M since it is a fair estimation of the correctness of the hypothesis behind our closure model. For the geometry and range of porosities tested, the correct limit is around Reynolds number 100. After this limit the error between the two quantities starts to be appreciable and so the closure problem (2.49) is no more correct. We suppose that at higher Reynolds numbers the linear correlation hypothesis between the average fields and the perturbations (equations (2.39) and (2.40)) does not hold. This chapter has been the basis for an article that has been already submitted and is now under review.

The interface treatment, based on the penalization method, has been investigated in chapter 5 [99]. It has been shown that the double linear smoothing of porosity and permeability has a positive effect on the correctness of the homogenized model. We have also shown that linear porosity profile derives directly from the geometry of the porous media and it is exact. On the contrary the linear smoothing for the permeability tensor is purely heuristic, but it can be supported by the fact that the porosity effects are largely the most important effect in the variability of $\mathbf{H}$. So, it is possible to argue that the two fields should have the same interface treatment. Another confirmation for this fact comes from the metamodel that, if left "free", it returns the linear profile of permeability at the interface without imposing it a priori. A paper is actually under preparation on the topics described in this chapter.

The VANS approach has been adopted in cases that naturally develop separation. The inclusion of a porous media layer has been tested and the solver has shown good computational performance without convergence problems. However, the physics of the separation is not much modified by the porous layer, as a matter of fact the recirculation bubble size remains almost the same. This results suggest that the laminar suppression mechanism could be not as effective as the turbulent one (already observed in literature). In any case, more simulations with different problem geometries are needed to generalize the results.

The OpenFoam implementation of the macroscopic solver based on the VANS equations can be downloaded from github from the address: `https://github.com/appanacca/`

---

[1]the angle between the forcing term in the momentum equations and the fiber axis.

`porous_solvers_OF`. The code listing is not directly shown in the manuscript since detailing the solver implementation would have required to explain and describes in details many OpenFoam library technicalities. These details have been already addressed in multiple sources (Jasak [81], Moukalled et al. [114] and Maric et al. [100]) and they are out of the scope of this work. To someone not new to OpenFoam programming the comments inside the code listing are sufficient to clarify the technical points.

6.1.1 Possible future research extensions

The database from which we have built our metamodel for the tensor **H** can be extended. For example, we could easily include more data points to make the model more reliable. Another interesting part could be the extension to other fibers geometry section or even other completely different porous media geometries (spheres, rocks ...). The database could also be extended to moving porous media, the input parameters could include some of the typical dynamical parameters like the mass ratio or the stiffness of the fibers. New metamodelling approaches could also be explored. Especially, when the database grows, *deep neural networks* could perform better than Kriging.

The validation of the interface treatment requires more data from DNS simulations or experiments in similar configurations. The availability of high resolution data is still a missing piece in the field.

The application of the macroscopic model to separated flow is only a starting point. We have shown that our model is able to provide fairly correct homogenized flow fields at a low computational cost. However, the capacity of a porous media layer to suppress the separation is still questioned, at least with the parameters used. This means that the optimal parameters are still to be found. An optimization procedure using the adjoint equation could solve this problem, now that we have clarified the penalization approach used in the VANS equations.

Another possible extension to the metamodel could be the implementation of the macroscopic approach for elastic porous media. Since the VANS solver is already been implemented this extension, for example by using a Bernoulli beam, should be fairly easy.

Appendix A: Kriging metamodel

Introduction

The kriging metamodel technique has already been introduced in chapter 4 however; to complete the description of the method, the numerical procedure and some implementation examples are presented in this appendix.

The kriging method was invented to get prediction of missing geostatics data (Krige [88]). However, this methodology has been further generalized and applied extensively to build metamodels for a large variety of applications. The method can treat highly non linear output of an experiment and can be used to either interpolate or extrapolate responses from a sample set.

In this discussion $\hat{f}(\boldsymbol{\chi})$ is a model for the true function $f(\boldsymbol{\chi})$ and $\hat{y}$ is the model prediction of the true response, $y = f(\boldsymbol{\chi})$, that is evaluated at the point $\boldsymbol{\chi}$.

After the exploration of the design possibilities the database produced is usually organized in a set $(\mathbf{x_i}, y(\mathbf{x_i}))$ $i = 1, ..., n$ where

- $\mathbf{x_i}$ is the $i - th$ vector element containing the k input parameters for the $i - th$ experiment realization;

- y_i is the scalar response of the experiment for the vector of inputs $\mathbf{x_i}$ [2];

- χ is the new input vector for which we seek the approximate output $\hat{y} = \hat{f}(\boldsymbol{\chi})$.

Mathematical modelling

We define with n the number of points in the sample design set and with k the number of inputs of the experiment; the $n \times k$ matrix containing all the inputs is indicated with $\mathbf{X}$ and the $n \times 1$ vector containing all the responses is indicated as $\mathbf{Y}$.

The kriging response for a new input point $\boldsymbol{\chi}$ is given by the linear *predictor*:

$$\hat{y} = \hat{f}(\boldsymbol{\chi}) = \sum_{i=1}^{N} \lambda_i(\boldsymbol{\chi}) f(\mathbf{x_i}) = \sum_{i=1}^{N} \lambda_i(\boldsymbol{\chi}) y_i, \qquad (6.1)$$

---

[2] y_i is always a scalar because even in case of multiple outputs for an experiment they are supposed to be uncorrelated. It means that if we had p elements in each $\mathbf{y_i}$ we would have to build p metamodels.

$\hat{y}$ is considered to be a new realization of the random Gaussian process that has generated the set of responses $\mathbf{Y}$. The weights λ_i are the solutions of a linear system obtained by minimizing the variance of the error between the predictor and the random process. The best *linear unbiased predictor* BLUP is obtained finding the weights λ_i that minimize:

$$MSE[\hat{y}(\chi)] = E\left[\left(\hat{f}(\chi) - f(\chi)\right)^2\right] = E\left[\left(\boldsymbol{\lambda}^T(\chi)\mathbf{Y} - y(\chi)\right)^2\right], \qquad (6.2)$$

under the unbiasedness condition:

$$E\left[\hat{f}(\chi) - f(\chi)\right] = E\left[\boldsymbol{\lambda}^T(\chi)\mathbf{Y} - \mathbf{y}(\chi)\right] = 0. \qquad (6.3)$$

This relation means that the predictor and the Gaussian process have the same mean value for every new point χ. The equation (6.3) is further developed yielding:

$$E\left[\hat{f}(\chi) - f(\chi)\right] = \boldsymbol{\lambda}^T\chi E\left[f(\mathbf{X})\right] - E\left[f(\chi)\right] = \sum_{i=1}^{n}\lambda_i(\chi)\mu(\mathbf{x_i}) - \mu(\chi) = 0, \qquad (6.4)$$

where $\mu(\chi)$ is the mean value of the true function at the point χ; instead $\mu(\mathbf{x_i})$ is the mean of all the realizations collected for the database.

Different types of kriging approximation exist accordingly to how $\mu(\chi)$ is evaluated:

- **simple kriging** assume that the trend has null value: $\mu(\chi) = 0$;

- **ordinary kriging** assume that the trend is an unknown constant: $\mu(\chi) = \mu$;

- **universal kriging** assumes that the trend is the solution of a generalized *least squares model* in which it is possible to decide the order $(n_\beta)^3$ of the chosen base: $\mu(\chi) = \mathbf{g}^T(\chi)\boldsymbol{\beta}$, where $\mathbf{g}(\chi)$ is the base evaluation at the point χ and the vector $\boldsymbol{\beta}$ contains the n_β coefficients of the model.

The unbiased condition (6.4) can be so rewritten, without loss of generality:

$$\boldsymbol{\lambda}^T(\chi)\mathbf{G}(\mathbf{X})\boldsymbol{\beta} - \mathbf{g}^T(\chi)\boldsymbol{\beta} = 0 \implies \boldsymbol{\lambda}^T(\chi)\mathbf{G}(\mathbf{X}) = \mathbf{g}^T(\chi), \qquad (6.5)$$

where $\mathbf{G}(\mathbf{X})$ is the $n \times n_\beta$ matrix containing the evaluation of the least squared basis functions at all points in $\mathbf{X}$.

---

[3]This means that, for example, taking $n_\beta = 2$ the least squared model is quadratic.

Also the relation (6.2) can be manipulated:

$$
\begin{aligned}
E\left[\left(\hat{f}(\boldsymbol{\chi}) - f(\boldsymbol{\chi})\right)^2\right] &= var(\hat{f}(\boldsymbol{\chi}) - f(\boldsymbol{\chi})) \\
&= var(\hat{f}(\boldsymbol{\chi})) + var(f(\boldsymbol{\chi})) - 2\ cov(\hat{f}(\boldsymbol{\chi}), f(\boldsymbol{\chi})) \\
&= var(\sum_{i=1}^{n}\lambda_i(\boldsymbol{\chi})f(\mathbf{x_i})) + var(f(\boldsymbol{\chi})) - 2\ cov(\sum_{i=1}^{n}\lambda_i(\boldsymbol{\chi})f(\mathbf{x_i}), f(\boldsymbol{\chi})) \\
&= \sum_{i=1}^{n}\sum_{j=1}^{n}\lambda_i(\boldsymbol{\chi})\lambda_j(\boldsymbol{\chi})\ cov(f(\mathbf{x_i}), f(\mathbf{x_j})) + var(f(\boldsymbol{\chi})) \\
&\qquad\qquad -2\sum_{i=1}^{n}\lambda_i(\boldsymbol{\chi})\ cov(f(\mathbf{x_i}), f(\boldsymbol{\chi})) \\
&= \sum_{i=1}^{n}\sum_{j=1}^{n}\lambda_i(\boldsymbol{\chi})\lambda_j(\boldsymbol{\chi})\ cov(\mathbf{x_i}, \mathbf{x_j}) + var(f(\boldsymbol{\chi})) \\
&\qquad\qquad -2\sum_{i=1}^{n}\lambda_i(\boldsymbol{\chi})\ cov(\mathbf{x_i}, \boldsymbol{\chi}), \tag{6.6}
\end{aligned}
$$

where $\mathbf{c} = cov(\mathbf{X}, \boldsymbol{\chi})$ is the vector containing the estimated covariance between each point in the input set $\mathbf{X}$ and the point $\boldsymbol{\chi}$ for which we search the estimator. Similarly, $\mathbf{C}_{ij} = cov(\mathbf{x_i}, \mathbf{x_j})$ represents the elements in the $n \times n$ matrix containing the correlation estimates between each point in $\mathbf{X}$. Possible estimations for the two covariance matrixies are listed in the next section.

The derivative of the relation (6.6) with respect to $\boldsymbol{\lambda}$ is posed equal to zero in order to minimize the kriging error, yielding the final relation:

$$
\boldsymbol{\lambda}^T(\boldsymbol{\chi})\mathbf{C} = \mathbf{c}. \tag{6.7}
$$

Introducing the Lagrangian multiplier ϕ for the unbiased constraint it is possible to build the partitioned matrix for the kriging metamodel:

$$
\begin{pmatrix} \mathbf{0} & \mathbf{G}^T \\ \mathbf{G} & \mathbf{C} \end{pmatrix} \begin{pmatrix} \phi \\ \boldsymbol{\lambda} \end{pmatrix} = \begin{pmatrix} \mathbf{g} \\ \mathbf{c} \end{pmatrix}. \tag{6.8}
$$

Then, by inverting the partitioned matrix the kriging predictor can be written as:

$$
\hat{y}(\boldsymbol{\chi}) = \mathbf{g}^T(\boldsymbol{\chi})\boldsymbol{\beta} + \mathbf{c}^T(\boldsymbol{\chi})\mathbf{R}^{-1}\left(\mathbf{Y} - \mathbf{G}\boldsymbol{\beta}\right). \tag{6.9}
$$

The first term $\mathbf{g}(\boldsymbol{\chi})^T\boldsymbol{\beta}$ is usually called *trend function* and the second term is the *Gaussian error model*. As a matter of fact, $(\mathbf{Y} - \mathbf{G}\boldsymbol{\beta})$ is the known vector of differences between the true outputs and the trend function at all the points $\mathbf{X}$ in the database.

126

One of the kriging metamodel benefits is that the model is exact at the data points. However, if it is known that the experimental realization used in the database presents some reliability issue and/or have noise[4], there is a technique that permits to take into account these effect. Adding a *nugget* (η) to all entries on the covariance matrix $\mathbf{C}^* = \mathbf{C} + \eta\mathbf{I}$ the metamodel is no more exact at the data points. The same technique is used to increase the conditioning number of the portioned system when dealing with numerical problems.

Covariance matrix choice

In order to give some indication on the choice of the proper covariance function let us first introduce the *semivariogram* concept. The semivariogram γ between two generics points, in the design space $\mathbf{x_1}, \mathbf{x_2}$, is defined as:

$$
\begin{aligned}
\gamma(\mathbf{x_1}, \mathbf{x_1}) &= \frac{1}{2}E\left[(f(\mathbf{x_1}) - \mu(\mathbf{x_1}) - f(\mathbf{x_2}) + \mu(\mathbf{x_2}))^2\right] \quad (6.10) \\
&= \frac{1}{2}var(f(\mathbf{x_1}) - f(\mathbf{x_2})) \\
&= \frac{1}{2}var(f(\mathbf{x_1})) + \frac{1}{2}var(f(\mathbf{x_2})) - cov(\mathbf{x_1}, \mathbf{x_2}) \quad (6.11)
\end{aligned}
$$

The semivariogram for each datapoint in the database can be directly computed from the equation (6.10) and afterwards the relation (6.11) can be used to fit the semivariogram data with the covariance function.

Lets us clarify the last statements with an example. We chose to replicate the example present in Cavazzuti [36] in which the author proposes an experiment that depends on two variables x_1 and x_2 and 10 realizations. The experiment database is shown in figure 6.1.

The semivariogram functions, as a function of the Eucledian distance between the two points $h_{ij} = |\mathbf{x}_i - \mathbf{x}_j|$, has been computed using equation (6.10) and is represented in figure 6.2 on the left. The points in the semivariogram are then averaged over a distance step whose width is equal to 0.25 and the points are shown on the right of figure 6.2. The correlation function should be chosen to be the best fit for the averaged semivariogram. This means that in theory, depending on the dataset, one could formulate a personalized covariance model.

What is done in practice is that some parametric families of correlation functions have been proposed in the literature; for example the *power exponential* correlation function reads:

$$
c(\mathbf{x}_i, \mathbf{x}_j) = \sigma^2 \exp\left(-\sum_{j=1}^{k} \theta_k |x_{i,k} - x_{j,k}|^\nu\right). \quad (6.12)
$$

The kriging predictor surfaces can show different behaviors for different selections of the above three parameters (σ, ν and $\boldsymbol{\theta}$) and their setting is thus crucial. The coefficient σ is an

---

[4]common in experimental data.

127
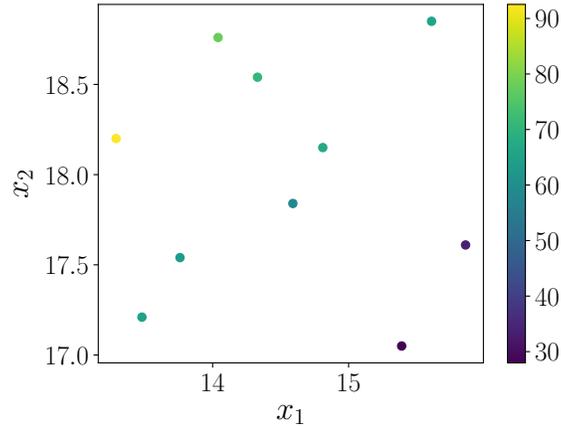
Figure 6.1: Experiment data points for the 10 realizations available. The color map represent the output realizations $\mathbf{Y}$ of the experiment $f(\mathbf{X})$.

amplitude parameter for the correlation function. It determines variations of the function $\hat{f}$ from its mean. Small values of σ characterize functions that stay close to their mean value, larger values allow more variations. It basically controls the gradient steepness around the data points. The exponent ν of the model has similar effects. The vector $\boldsymbol{\theta} = (\theta_{x_1}, \theta_{x_2})$ is a length scale parameter for the distance $|\mathbf{x_i} - \mathbf{x_j}|$; describes how smooth a function is. Small length scale values mean that function values can change quickly generating narrow bumps near the data points. Large values characterize functions that change only slowly but it will make the surface explode outside the convex hull described by the data points. It is possible to specify different length scales in different directions, in this manner the metamodel can include anisotropic effect for each variable of the experiment. This model has been fitted in the previous semivariogram choosing $\nu = 2$, $\theta = 1.895$ and $\sigma = 38.44$ and it is depicted in the right figure 6.2 using a red line. Is possible to see that this model fits well the data points for this experiment.

Another popular model for the covariance function is the *Matérn model*[5] that reads:

$$c(\mathbf{x}_i, \mathbf{x}_j) = \sigma^2 \frac{2^{1-\nu}}{\Gamma(\nu)} \sum_{j=1}^{k} \left[\left(\frac{\sqrt{2\nu} |x_{i,k} - x_{j,k}|}{\theta_k} \right)^{\nu} \mathcal{K}_\nu \left(\frac{\sqrt{2\nu} |x_{i,k} - x_{j,k}|}{\theta_k} \right) \right], \qquad (6.13)$$

where $\mathcal{K}_\nu(.)$ is a modified Bessel function and $\Gamma(.)$ is the gamma function. The parameters that can be used to tune the metamodel are the amplitude parameter σ, the exponent ν and the scale vector $\boldsymbol{\theta}$ with the same meaning as in the previous correlation function.

To summarize, when choosing the correlation it should be kept in mind:

- to well approximate the trend of the averaged semivariogram,

---

[5]the one used in chapter 4.
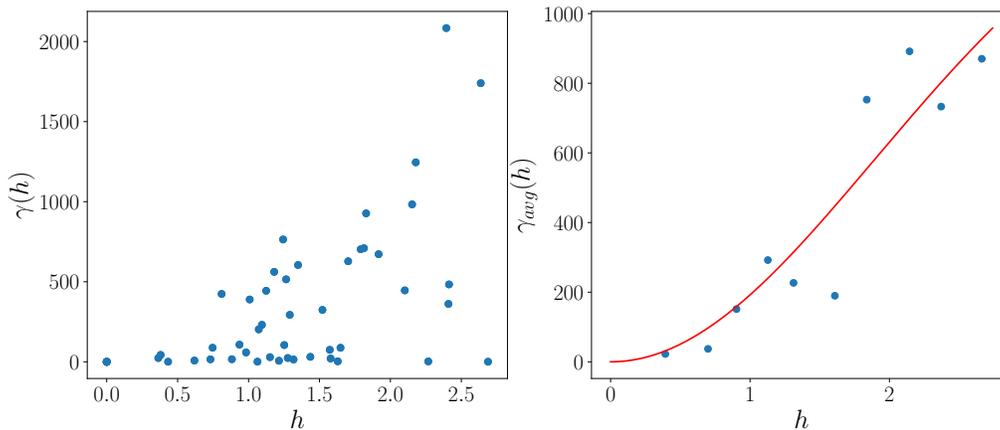
Figure 6.2: Left: Semivariogram versus the Euclidean distance computed for each data point against the other. Right: The blue dots represents the same semivarigram on the left but averaged over a step distance equal to 0.25. The red line corresponds to the semivariogram computed using relation (6.11) with the covariance model *power exponential* with parameters $\nu = 2$, $\theta = 1.895$ and $\sigma = 38.44$.

- the scale parameter $\boldsymbol{\theta}$ highly changes the presence of spurious minima and maxima in the metamodel. The others parameters ν, σ and η control the gradient and the exactness of the model around the data points.

Some examples of the response surface built with the above parameters are presented in the next section, along with the actual implementation.

Implementation example

An example of the implementation of kriging algorithm is presented in the following. To build the model we use the open source library openTURNS (Baudin et al. [13]) using its Python application programming interface[6]. This interface has been chosen because it is very expressive even to non programmers. The code is shown in the listing below where each line is commented and is self explanatory. From line 1 through 22 the experiment database is created, in line 24 the trend function model is set constant but line 26 and 28 show how to set linear and quadratic least square trends. The covariance model is set in line 31, and from line 35 to 42 the algorithm metamodel tree is built and executed. At the end it is possible to get a callable function on the desired new point, line 44-47.

```python
import numpy as np # import the generic vector library
import openturns as ot # import the openTURNS library
```

[6]although the crunching number computation is performed under the hood with C++.

```python
 3
 4          # define the k input varibles as a n dimensional array
 5          x1 = np.array([14.04, 14.33, 15.39, 13.76, 14.59,
 6                                  13.48, 15.86, 15.61, 13.29, 14.81])
 7          x2 = np.array([18.76, 18.54, 17.05, 17.54, 17.84,
 8                          17.21, 17.61, 18.85, 18.20, 18.15])
 9
10          # transform the inputs as a n by k array
11          x = np.column_stack((x1, x2))
12
13          # define the outputs as  a n by 1 array
14          y = np.array([[10],[2 ],[4],[-2],[9],[3] ,[0], [-1]])
15
16          # tranform the array in OT samples
17          X = ot.Sample(x)
18          Y = ot.Sample(y)
19
20          # explicit define the number of input i.e the k number
21          dimension = len(x[0])
22
23          # define the constant trend function
24          basis = ot.ConstantBasisFactory(dimension).build()
25          # or the linear trend
26          # basis = ot.LinearBasisFactory(dimension).build()
27          # or the quadratic trend
28          # basis = ot.QuadraticBasisFactory(dimension).build()
29
30          # select the covariance model squared exponential (sigma, theta)
31          covarianceModel = ot.SquaredExponential([38.44], [1.895])
32          # or define the Matern model
33          # covarianceModel = ot.MaternModel()
34
35          algo = ot.krigingAlgorithm(X, Y, covarianceModel, basis) # build the metamodel
36
37          # eta = 0.2
38          # algo.setNoise([eta]*len(y)) # set the optional nugget
39
40          algo.run() # run the metamodel tree computation
41          result = algo.getResult() # return a container for the results
42          metamodel = result.getMetaModel() # get a callable function
43
```

```
44          # set the new point to compute
45          chi = np.array([13, 17])
46          # get the metamodel prediction for the point chi
47          y_chi = np.array(metamodel(chi))
```
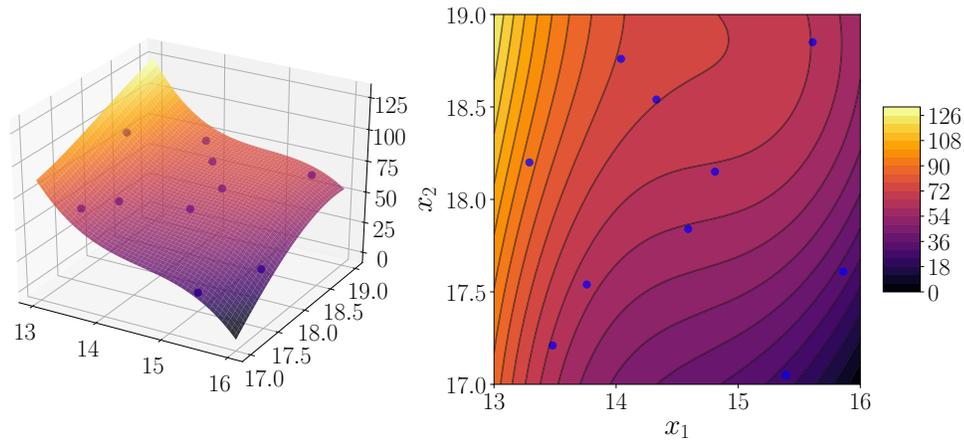
Figure 6.3: kriging metamodel surface for using a constant trend function and the *power exponential* covariance model with parameters $\nu = 2$, $\theta = 1.895$ and $\sigma = 38.44$.

It is possible to pass directly a vector of new points to the function *metamodel* in line 44. Figures 6.3, 6.4 and 6.5 show some metamodel surfaces with different parameters setup.

It is possible to see that changing the parameters of the kriging metamodel the shape of the response function can change, and some very bad choice of the parameters can lead to very exotic shapes, like in figure 6.5. In any case it is possible to test the robustness of a certain setup using an error estimate like the one proposed in chapter 4. In practical applications the choice of the optimal parameters is usually left to the experience of the user.

Final remarks

Further detail on theoretical and computational aspects can be found in Cavazzuti [36], Adams et al. [2], Sacks et al. [138] and Baudin et al. [13]. The above code snippet is public, in the GitHub repository of the author can be found at the address: `https://github.com/appanacca/kriging_book.git`. The OpenTRUNS library implementation is available at the previous repository link. In addition an equivalent ordinary kriging implementation, starting from scratch, can be downloaded. More generally whenever a reduced order model has to be built with a not extremely large amount of data the Kriging metamodelling should be a solution to investigate seriously.
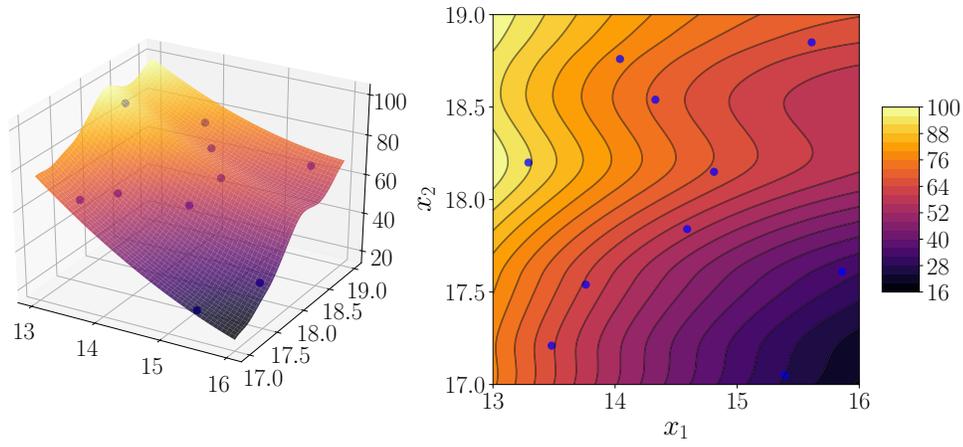
Figure 6.4: kriging metamodel surface for using a quadratic trend function and the *Matern* covariance model with parameters $\nu = 1.5$, $\theta = 10$ and $\sigma = 1$.
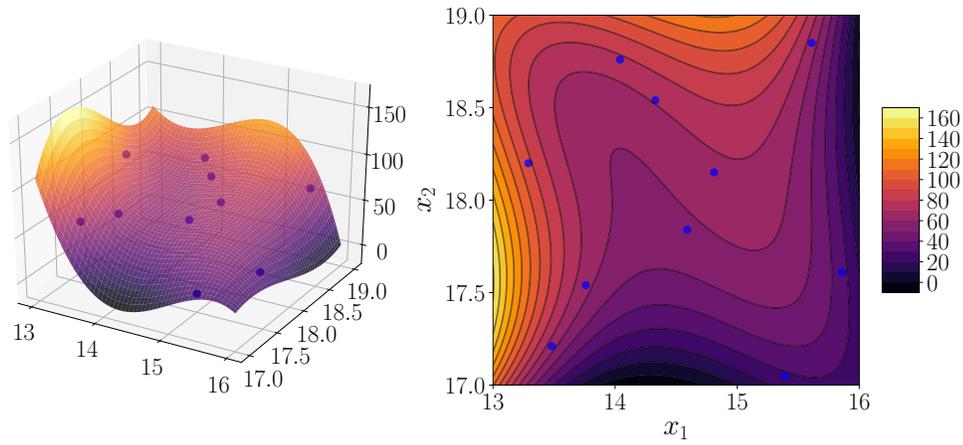
Figure 6.5: kriging metamodel surface for using a linear trend function and the *power exponential* covariance model with parameters $\nu = 2$, $\theta = 0.8$ and $\sigma = 10$.

Bibliography

[1] J.D. Ackerman and A. Okubo. Reduced mixing in a marine macrophyte canopy. *Functional Ecology*, pages 305–309, 1993.

[2] B.M. Adams, L.E. Bauman, W.J. Bohnhoff, K.R. Dalbey, M.S. Ebeida, J.P. Eddy, M.S. Eldred, P.D. Hough, K.T. Hu, J.D. Jakeman, J.A. Stephens, L.P. Swiler, D.M. Vigil, , and T.M. Wildey. Dakota, a multilevel parallel object-oriented framework for design optimization, parameter estimation, uncertainty quantification, and sensitivity analysis: Version 6.0 Theory Manual. Technical report, Sandia National Laboratories, SAND2014-4253, 2014.

[3] M. Agnaou, D. Lasseux, and A. Ahmadi. From steady to unsteady laminar flow in model porous structures: an investigation of the first Hopf bifurcation. *Computers & Fluids*, 136:67–82, 2016.

[4] G.P. Almeida, D.F.G. Durao, and M.V. Heitor. Wake flows behind two-dimensional model hills. *Experimental Thermal and Fluid Science*, 7(1):87–101, 1993.

[5] J. Alvarado, J. Comtet, E. De Langre, and A.E. Hosoi. Nonlinear flow response of soft hair beds. *Nature Physics*, 13:1014–1019, 2017.

[6] P. Angot, B. Goyeau, and J.A. Ochoa-Tapia. Asymptotic modeling of transport phenomena at the interface between a fluid and a porous layer: Jump conditions. *Physical Review E*, 95(6):063302, 2017.

[7] T. Asaeda, T. Fujino, and J. Manatunge. Morphological adaptations of emergent plants to water flow: a case study with typha angustifolia, zizania latifolia and phragmites australis. *Freshwater Biology*, 50(12):1991–2001, 2005.

[8] J.L. Auriault. Effective macroscopic description for heat conduction in periodic composites. *International Journal of Heat and Mass Transfer*, 26(6):861–869, 1983.

[9] J.L. Auriault and E. Sanchez-Palencia. Etude du comportement macroscopique d'un milieu poreux saturé déformable. *Journal de mécanique*, 16(4):575–603, 1977.

[10] J. Barrere, O. Gipouloux, and S. Whitaker. On the closure problem for darcy's law. *Transport in Porous Media*, 7(3):209–222, 1992.

[11] S. Barsu, D. Doppler, J.J.S. Jerome, N. Rivière, and M. Lance. Drag measurements in laterally confined 2d canopies: Reconfiguration and sheltering effect. *Physics of Fluids*, 28(10):107101, 2016.

[12] I. Battiato and S. Rubol. Single-parameter model of vegetated aquatic flows. *Water Resources Research*, 50(8):6358–6369, 2014.

[13] M. Baudin, A. Dutfoy, B. Iooss, and A.L. Popelin. *OpenTURNS: An industrial software for uncertainty quantification in simulation.* Springer International Publishing, 2016. ISBN 978-3-319-11259-6. doi: 10.1007/978-3-319-11259-6_64-1. URL `http://dx.doi.org/10.1007/978-3-319-11259-6_64-1`.

[14] G.S. Beavers and D.D. Joseph. Boundary conditions at a naturally permeable wall. *Journal of Fluid Mechanics*, 30(1):197–207, 1967.

[15] D.W. Bechert, M. Bruse, W. Hage, and R. Meyer. Biological surfaces and their technological application—laboratory and flight experiments on drag reduction and separation control. *AIAA paper*, 1960, 1997.

[16] D.W. Bechert, M. Bruse, W. Van der Hage, J.G.Th. Van der Hoeven, and G. Hoppe. Experiments on drag-reducing surfaces and their optimization with an adjustable geometry. *Journal of Fluid Mechanics*, 338:59–87, 1997.

[17] S.E. Belcher, I.N. Harman, and J.J. Finnigan. The wind in the willows: flows in forest canopies in complex terrain. *Annual Review of Fluid Mechanics*, 44:479–504, 2012.

[18] S. Bhattacharyya and A.K. Singh. Reduction in drag and vortex shedding frequency through porous sheath around a circular cylinder. *International Journal for Numerical Methods in Fluids*, 65(6):683–698, 2011.

[19] B. Bhushan. *Biomimetics: bioinspired hierarchical-structured surfaces for green science and technology.* Springer, 2016.

[20] A. Boomsma and F. Sotiropoulos. Direct numerical simulation of sharkskin denticles in turbulent channel flow. *Physics of Fluids*, 28(3):035106, 2016.

[21] A. Bottaro, P. Corbett, and P. Luchini. The effect of base flow variation on flow stability. *Journal of Fluid Mechanics*, 476:293–302, 2003.

[22] M. Breuer, B. Jaffrézic, S. Šaric, S. Jakirlic, G. Deng, O. Chikhaoui, J. Fröhlich, D. von Terzi, M. Manhart, and N. Peller. Issues in hybrid les–rans and coarse grid les of separated flows. In *EUROMECH colloquium*, volume 469, pages 6–8, 2005.

[23] M. Breuer, N. Peller, C. Rapp, and M. Manhart. Flow over periodic hills–numerical and experimental study in a wide range of reynolds numbers. *Computers & Fluids*, 38(2):433–457, 2009.

[24] W.P. Breugem, B.J. Boersma, and R.E. Uittenbogaard. The influence of wall permeability on turbulent channel flow. *Journal of Fluid Mechanics*, 562:35–72, 2006.

[25] W. Brevis, M. García-Villalba, and Y. Niño. Experimental and large eddy simulation study of the flow developed by a sequence of lateral obstacles. *Environmental Fluid Mechanics*, 14(4):873–893, 2014.

[26] H.C. Brinkman. A calculation of the viscous force exerted by a flowing fluid on a dense swarm of particles. *Applied Scientific Research*, 1(1):27–34, 1949.

[27] C.H. Bruneau and I. Mortazavi. Passive control of the flow around a square cylinder using porous media. *International Journal for Numerical Methods in Fluids*, 46(4): 415–433, 2004.

[28] C.H. Bruneau and I. Mortazavi. Numerical modelling and passive flow control using porous media. *Computers & Fluids*, 37(5):488–498, 2008.

[29] C.H. Bruneau, E. Creusé, D. Depeyras, P. Gilliéron, and I. Mortazavi. Coupling active and passive techniques to control the flow past the square back ahmed body. *Computers & Fluids*, 39(10):1875–1892, 2010.

[30] D.M. Bushnell, J.N. Hefner, and R.L. Ash. Effect of compliant wall motion on turbulent boundary layers. *Physics of Fluids*, 20(10):S31–S48, 1977.

[31] J.P. Caltagirone. Sur l'intéraction fluide-milieu poreux; application au calcul des efforts exercés sur un obstacle par un fluide visqueux. *Comptes rendus de l'Académie des sciences. Série II, Mécanique, physique, chimie, astronomie*, 318(5):571–577, 1994.

[32] C. Canuto, M.Y. Hussaini, A. Quarteroni, and T.A. Zang. Spectral methods in fluid dynamics. Technical report, Springer, 1988.

[33] R.G. Carbonell and S. Whitaker. Heat and mass transfer in porous media. *Fundamentals of transport phenomena in porous media*, 82:121–198, 1984.

[34] P.C. Carman. Fluid Flow Through Granular Beds. *Transactions - Institution of Chemical Engineeres*, 15:150–166, 1937.

[35] P.W. Carpenter. Status of transition delay using compliant walls. *Viscous drag reduction in boundary layers*, 123:79–113, 1990.

[36] M. Cavazzuti. *Optimization methods: from theory to design scientific and technological aspects in mechanics.* Springer Science & Business Media, 2012.

[37] P.H. Chang, C.C. Liao, H.W. Hsu, S.H. Liu, and C.A. Lin. Simulations of laminar and turbulent flows over periodic hills with immersed boundary method. *Computers & Fluids*, 92:233–243, 2014.

[38] R. Chen, I. Teruaki, N. Toshiyuki, and L. Hao. Owl-inspired leading-edge serrations play a crucial role in aerodynamic force production and sound suppression. *Bioinspiration & Biomimetics*, 12(4):046008, 2017.

[39] H. Choi, P. Moin, and J. Kim. Direct numerical simulation of turbulent flow over riblets. *Journal of Fluid Mechanics*, 255:503–539, 1993.

[40] F. Cimolin and M. Discacciati. Navier–stokes/forchheimer models for filtration through porous media. *Applied Numerical Mathematics*, 72:205–224, 2013.

[41] W.O. Criminale, T.L. Jackson, and R.D. Joslin. *Theory and computation of hydrodynamic stability.* Cambridge University Press, 2003.

[42] H. Darcy. *Les fontaines publiques de la ville de Dijon.* Victor Dalmont, 1856.

[43] Y. Davit and M. Quintard. Technical notes on volume averaging in porous media i: How to choose a spatial averaging operator for periodic and quasiperiodic structures. *Transport in Porous Media*, 119(3):555–584, 2017.

[44] Y. Davit, C.G. Bell, H.M Byrne, L.A.C. Chapman, L.S. Kimpton, G.E. Lang, K.H.L. Leonard, J.M. Oliver, N.C. Pearson, and R.J. Shipley. Homogenization via formal multiscale asymptotics and volume averaging: How do the two techniques compare? *Advances in Water Resources*, 62:178–206, 2013.

[45] E. De Langre. Effects of wind on plants. *Annu. Rev. Fluid Mech.*, 40:141–168, 2008.

[46] B. Dean and B. Bhushan. Shark-skin surfaces for fluid-drag reduction in turbulent flow: a review. *Philosophical Transactions of the Royal Society of London A: Mathematical, Physical and Engineering Sciences*, 368(1929):4775–4806, 2010.

[47] A. Duda, Z. Koza, and M. Matyka. Hydraulic tortuosity in arbitrary porous media flow. *Physical Review E*, 84(3):036319, 2011.

[48] S. Dupont, F. Gosselin, C. Py, E. De Langre, P. Hemon, and Y. Brunet. Modelling waving crops using large-eddy simulation: comparison with experiments and a linear stability analysis. *Journal of Fluid Mechanics*, 652:5–44, 2010.

[49] J.E. Eckman. The role of hydrodynamics in recruitment, growth, and survival of argopecten irradians (l.) and anomia simplex (d'orbigny) within eelgrass meadows. *Journal of Experimental Marine Biology and Ecology*, 106(2):165–191, 1987.

[50] D.A. Edwards, M. Shapiro, P. Bar-Yoseph, and M. Shapira. The influence of Reynolds number upon the apparent permeability of spatially periodic arrays of cylinders. *Physics of Fluids A: Fluid Dynamics*, 2(1):45–55, 1990.

[51] M. Ehrhardt. An introduction to fluid-porous interface coupling. Technical report, 2010.

[52] S. Ergun and A.A. Orning. Fluid flow through randomly packed columns and fluidized beds. *Industrial & Engineering Chemistry*, 41(6):1179–1184, 1949.

[53] J. Favier, A. Dauptain, D. Basso, and A. Bottaro. Passive separation control using a self-adaptive hairy coating. *Journal of Fluid Mechanics*, 627:451–483, 2009.

[54] J. Favier, C. Li, L. Kamps, A. Revell, J. O'Connor, and C. Brücker. The pelskin project—part i: fluid–structure interaction for a row of flexible flaps: a reference study in oscillating channel flow. *Meccanica*, 52(8):1767–1780, 2017.

[55] J. Finnigan. Turbulence in plant canopies. *Annual Review of Fluid Mechanics*, 32 (1):519–571, 2000.

[56] M. Firdaouss, J.L. Guermond, and P. Le Quéré. Nonlinear corrections to darcy's law at low reynolds numbers. *Journal of Fluid Mechanics*, 343:331–350, 1997.

[57] M. Firdaouss, J.L. Guermond, and D. Lafarge. Some remarks on the acoustic parameters of sharp-edged porous media. *International journal of engineering science*, 36(9):1035–1046, 1998.

[58] P.H. Forchheimer. Wasserbewegung durch boden. *Zeitz. Ver. Duetch Ing.*, 45:1782–1788, 1901.

[59] M.C. Gambi, A.R.M. Nowell, and P.A. Jumars. Flume observations on flow dynamics in zostera marina (eelgrass) beds. *Marine ecology progress series*, pages 159–169, 1990.

[60] R. Garcia Mayoral and N. Abderrahaman-Elena. Analysis of anisotropically permeable surfaces for turbulent drag reduction. *Physical Review Fluids*, 2017.

[61] R. García-Mayoral and J. Jiménez. Drag reduction by riblets. *Philosophical Transactions of the Royal Society of London A: Mathematical, Physical and Engineering Sciences*, 369(1940):1412–1427, 2011.

[62] R. García-Mayoral and J. Jiménez. Hydrodynamic stability and breakdown of the viscous regime over riblets. *Journal of Fluid Mechanics*, 678:317–347, 2011.

[63] M. Ghisalberti. Obstructed shear flows: similarities across systems and scales. *Journal of Fluid Mechanics*, 641:51–61, 2009.

[64] M. Ghisalberti and H. Nepf. Mixing layers and coherent structures in vegetated aquatic flows. *Journal of Geophysical Research: Oceans*, 107(C2), 2002.

[65] M. Ghisalberti and H. Nepf. The limited growth of vegetated shear layers. *Water Resources Research*, 40(7), 2004.

[66] M. Ghisalberti and H. Nepf. Mass transport in vegetated shear flows. *Environmental Fluid Mechanics*, 5(6):527–551, 2005.

[67] A.A. Giunta, S.F. Wojtkiewicz, and M.S. Eldred. Overview of modern design of experiments methods for computational simulations. In *Proceedings of the 41st AIAA aerospace sciences meeting and exhibit, AIAA-2003-0649*, 2003.

[68] G. Gomez-de Segura, A. Sharma, and R. Garcia-Mayoral. Turbulent drag reduction by anisotropic permeable coatings. In 10th *International Symposium on Turbulence and Shear Flow Phenomena*, 2017.

[69] F. Gosselin and E. De Langre. Destabilising effects of plant flexibility in air and aquatic vegetation canopy flows. *European Journal of Mechanics-B/Fluids*, 28(2): 271–282, 2009.

[70] Frédérick P Gosselin and Emmanuel De Langre. Drag reduction by reconfiguration of a poroelastic system. *Journal of Fluids and Structures*, 27(7):1111–1123, 2011.

[71] W.G. Gray. A derivation of the equations for multi-phase transport. *Chemical Engineering Science*, 30(2):229–233, 1975.

[72] L. Grizzetti, M. Quadrio, and L. Cortelezzi. Studio sperimentale della scia di un corpo tozzo in presenza di inserti di materiale poroso. Master's thesis, Politecnico di Milano: Dipartimento Ingegneria Aerospaziale, 2015.

[73] R.E. Grizzle, F.T. Short, C.R. Newell, H. Hoven, and L. Kindblom. Hydrodynamically induced synchronous waving of seagrasses:'monami'and its possible effects on larval mussel settlement. *Journal of Experimental Marine Biology and Ecology*, 206 (1-2):165–177, 1996.

[74] A.M. Hamed, M.J. Sadowski, H. Nepf, and L.P. Chamorro. Impact of height heterogeneity on canopy turbulence. *Journal of Fluid Mechanics*, 813:1176–1196, 2017.

[75] A.F. Heenan and J.F. Morrison. Passive control of pressure fluctuations generated by separated flow. *AIAA journal*, 36(6):1014–1022, 1998.

[76] M.Y. Hussaini and T.A. Zang. Spectral methods in fluid dynamics. *Annual Review of Fluid Mechanics*, 19(1):339–367, 1987.

[77] J. Hussong, W.P. Breugem, and J. Westerweel. A continuum model for flow induced by metachronal coordination between beating cilia. *Journal of Fluid Mechanics*, 684: 137–162, 2011.

[78] S. Ikeda and M. Kanazawa. Three-dimensional organized vortices above flexible water plants. *Journal of Hydraulic Engineering*, 122(11):634–640, 1996.

[79] E. Inoue. Studies of the phenomena of waving plants ("honami") caused by wind. *Journal of Agricultural Meteorology*, 11(3):87–90, 1955.

[80] M. Itoh, S. Tamano, R. Iguchi, K. Yokota, N. Akino, R. Hino, and S. Kubo. Turbulent drag reduction by the seal fur surface. *Physics of Fluids*, 18(6):065102, 2006.

[81] H. Jasak. *Error Analysis and Estimation for the Finite Volume Method with Applications to Fluid Flows, 1996*. PhD thesis, Ph. D. Thesis, University of London Imperial College, 1996.

[82] J.W. Jaworski and N. Peake. Aerodynamic noise from a poroelastic edge with implications for the silent flight of owls. *Journal of Fluid Mechanics*, 723:456–479, 2013.

[83] J. Jimenez, M. Uhlmann, A. Pinelli, and G. Kawahara. Turbulent shear flow over active and passive porous surfaces. *Journal of Fluid Mechanics*, 442:89–117, 2001.

[84] M.P. Juniper, A. Hanifi, and V. Theofilis. Modal stability theory: Lecture notes from the flow-nordita summer school on advanced instability methods for complex flows, stockholm, sweden, 2013. *Applied Mechanics Reviews*, 66(2):024804, 2014.

[85] K. Klausmann and B. Ruck. Drag reduction of circular cylinders by porous coating on the leeward side. *Journal of Fluid Mechanics*, 813:382–411, 2017.

[86] J.P.C. Kleijnen. Regression and kriging metamodels with their experimental designs in simulation: A review. *European Journal of Operational Research*, 256(1):1 – 16, 2017. ISSN 0377-2217.

[87] J. Kozeny. Über grundwasserbewegung. *Wasserkraft und Wasserwirtschaft*, 22(5): 67–70, 1927.

[88] D.G. Krige. A statistical approach to some basic mine valuation problems on the witwatersrand. *Journal of the Southern African Institute of Mining and Metallurgy*, 52(6):119–139, 1951.

[89] U. Lācis and S. Bagheri. A framework for computing effective boundary conditions at the interface between free fluid and a porous medium. *Journal of Fluid Mechanics*, 812:866–889, 2017.

[90] U. Lācis, G.A. Zampogna, and S. Bagheri. A computational continuum model of poroelastic beds. In *Proc. R. Soc. A*, volume 473, page 20160932. The Royal Society, 2017.

[91] D. Lafarge, M. Henry, M. Firdaouss, and J.L. Guermond. Sound propagation in gas-filled rigid-framed porous media: General theory and new experimental and numerical data. *The Journal of the Acoustical Society of America*, 103(5):2882–2882, 1998.

[92] A. Lang, M. Bradshaw, J. Smith, J. Wheelus, P. Motta, M. Habegger, and R. Hueter. Movable shark scales act as a passive dynamic micro-roughness to control flow separation. *Bioinspiration & Biomimetics*, 9:036017, 07 2014.

[93] D. Lasseux, A. Arani Abbasian, and A. Ahmadi. On the stationary macroscopic inertial effects for one phase flow in ordered and disordered porous media. *Physics of Fluids (1994-present)*, 23(7):073103, 2011.

[94] M. Le Bars and M.G. Worster. Interfacial conditions between a pure fluid and a porous medium: implications for binary alloy solidification. *Journal of Fluid Mechanics*, 550:149–173, 2006.

[95] G.M. Lilley. A study of the silent flight of the owl. *AIAA paper*, 2340(1998):l–6, 1998.

[96] P. Luchini, F. Manzo, and A. Pozzi. Resistance of a grooved surface to parallel flow and cross-flow. *Journal of Fluid Mechanics*, 228:87–109, 1991.

[97] N. Luminari, C. Airiau, and A. Bottaro. Drag-model sensitivity of kelvin-helmholtz waves in canopy flows. *Physics of Fluids*, 28(12):124103, 2016.

[98] N. Luminari, C. Airiau, and A. Bottaro. Effects of porosity and inertia on the apparent permeability tensor in fibrous porous media. *International Journal of Multiphase Flow*, submitted, 2018.

[99] N. Luminari, G. Zampogna, C. Airiau, and A. Bottaro. A penalization method to handle the interface between a free-fluid region and a fibrous porous medium. *Journal of Porous Media*, submitted, 2018.

[100] T. Maric, J. Hopken, and K. Mooney. *The OpenFOAM technology primer, edition.* 2014.

[101] T.I. Marjoribanks, R.J. Hardy, S.N. Lane, and D.R. Parsons. Does the canopy mixing layer model apply to highly flexible aquatic vegetation? insights from numerical modelling. *Environmental Fluid Mechanics*, 17(2):277–301, 2017.

[102] C.M. Marle. On macroscopic equations governing multiphase flow with diffusion and chemical reactions in porous media. *International Journal of Engineering Science*, 20(5):643–662, 1982.

[103] S. Martin and B. Bhushan. Discovery of riblets in a bird beak (rynchops) for low fluid drag. *Philosophical Transactions of the Royal Society of London A: Mathematical, Physical and Engineering Sciences*, 374(2073), 2016. ISSN 1364-503X. doi: 10.1098/rsta.2016.0134.

[104] M. Maza, J.L. Lara, and I.J. Losada. A coupled model of submerged vegetation under oscillatory flow using navier–stokes equations. *Coastal Engineering*, 80:16–34, 2013.

[105] M. Maza, J.L. Lara, and I.J. Losada. Tsunami wave interaction with mangrove forests: A 3-d numerical approach. *Coastal Engineering*, 98:33–54, 2015.

[106] D. McLean. *Understanding aerodynamics: arguing from the real physics.* John Wiley & Sons, 2012.

[107] C.C. Mei and J.L. Auriault. The effect of weak inertia on flow through a porous medium. *Journal of Fluid Mechanics*, 222:647–663, 1991.

[108] C.C. Mei and B. Vernescu. *Homogenization methods for multiscale mechanics.* World scientific, 2010.

[109] A. Mikelic and W. Jäger. On the interface boundary condition of beavers, joseph, and saffman. *SIAM Journal on Applied Mathematics*, 60(4):1111–1127, 2000.

[110] C. Mimeau, I. Mortazavi, and G.H. Cottet. Passive control of the flow around a hemisphere using porous media. *European Journal of Mechanics-B/Fluids*, 65:213–226, 2017.

[111] M. Minale. Momentum transfer within a porous medium. ii. stress boundary condition. *Physics of Fluids*, 26(12):123102, 2014.

[112] A. Monti, M. Omidyeganeh, and A. Pinelli. Large-eddy-simulation of a flow over a submerged rigid canopy. *Bulletin of the American Physical Society*, 2017.

[113] P. Motta, M. Habegger, A. Lang, R. Hueter, and J. Davis. Scale morphology and flexibility in the shortfin mako isurus oxyrinchus and the blacktip shark carcharhinus limbatus. *Journal of morphology*, 273, 10 2012.

[114] F. Moukalled, L. Mangani, and M. Darwish. *The finite volume method in computational fluid dynamics.* Springer, 2016.

[115] H. Naito and K. Fukagata. Numerical simulation of flow around a circular cylinder having porous surface. *Physics of Fluids*, 24(11):117102, 2012.

[116] H. Nepf. Drag, turbulence, and diffusion in flow through emergent vegetation. *Water resources research*, 35(2):479–489, 1999.

[117] H. Nepf. Flow and transport in regions with aquatic vegetation. *Annual Review of Fluid Mechanics*, 44:123–142, 2012.

[118] J.A. Ochoa-Tapia and S. Whitaker. Momentum transfer at the boundary between a porous medium and a homogeneous fluid—i. theoretical development. *International Journal of Heat and Mass Transfer*, 38(14):2635–2646, 1995.

[119] J.A. Ochoa-Tapia, F.J. Valdés-Parada, B. Goyeau, and D. Lasseux. Fluid motion in the fluid/porous medium inter-region. *Revista Mexicana de Ingeniería Química*, 16 (3):923–938, 2017.

[120] J. Oeffner and G.V. Lauder. The hydrodynamic function of shark skin and two biomimetic applications. *Journal of Experimental Biology*, 215(5):785–795, 2012. ISSN 0022-0949. doi: 10.1242/jeb.063040.

[121] S. Ortiz, J.M. Chomaz, and T. Loiseleux. Spatial holmboe instability. *Physics of Fluids*, 14(8):2585–2597, 2002.

[122] C.T. Paéz-García, F.J. Valdés-Parada, and D. Lasseux. Macroscopic momentum and mechanical energy equations for incompressible single-phase flow in porous media. *Physical Review E*, 95(2):023101, 2017.

[123] S. Patil and V.P. Singh. Characteristics of monami wave in submerged vegetated flow. *Journal of Hydrologic Engineering*, 15(3):171–181, 2010.

[124] M. Pauthenet, Y. Davit, M. Quintard, and A. Bottaro. Topological scaling for inertial transition in porous media. *submitted*, 2017.

[125] D.J.L. Penha, Be.J. Geurts, S. Stolz, and M. Nordlund. Computing the apparent permeability of an array of staggered square rods using volume-penalization. *Computers & Fluids*, 51(1):157–173, 2011.

[126] A. Pinelli, M. Omidyeganeh, C. Brücker, A. Revell, A. Sarkar, and E. Alinovi. The pelskin project: part iv—control of bluff body wakes using hairy filaments. *Meccanica*, 52(7):1503–1514, 2017.

[127] C. Py, E. De Langre, and B. Moulia. The mixing layer instability of wind over a flexible crop canopy. *Comptes Rendus Mécanique*, 332(8):613–618, 2004.

[128] C. Py, E. De Langre, and B. Moulia. A frequency lock-in mechanism in the interaction between wind and crop canopies. *Journal of Fluid Mechanics*, 568:425–449, 2006.

[129] M. Quintard and S. Whitaker. Transport in ordered and disordered porous media i: The cellular average and the use of weighting functions. *Transport in Porous Media*, 14(2):163–177, 1994.

[130] M. Quintard and S. Whitaker. Transport in ordered and disordered porous media ii: Generalized volume averaging. *Transport in Porous Media*, 14(2):179–206, 1994.

[131] M. Quintard and S. Whitaker. Transport in ordered and disordered porous media iii: Closure and comparison between theory and experiment. *Transport in Porous Media*, 15(1):31–49, 1994.

[132] M. Quintard and S. Whitaker. Transport in ordered and disordered porous media iv: Computer generated porous media for three-dimensional systems. *Transport in Porous Media*, 15(1):51–70, 1994.

[133] M. Quintard and S. Whitaker. Transport in ordered and disordered porous media v: Geometrical results for two-dimensional systems. *Transport in Porous Media*, 15(2): 183–196, 1994.

[134] M.R. Raupach, J.J. Finnigan, and Y. Brunet. Coherent eddies and turbulence in vegetation canopies: the mixing-layer analogy. In *Boundary-Layer Meteorology 25th Anniversary Volume, 1970–1995*, pages 351–382. Springer, 1996.

[135] A. Revell, J. O'Connor, A. Sarkar, C. Li, J. Favier, L. Kamps, and C. Brücker. The pelskin project: part ii—investigating the physical coupling between flexible filaments in an oscillating flow. *Meccanica*, 52(8):1781–1795, 2017.

[136] P.J. Roache. *Verification and validation in computational science and engineering.* Hermosa Press, Albuquerque, NM., 1998.

[137] M.E. Rosti, L. Kamps, C. Bruecker, M. Omidyeganeh, and A. Pinelli. The pelskin project-part v: towards the control of the flow around aerofoils at high angle of attack using a self-activated deployable flap. *Meccanica*, 52(8):1811–1824, 2017.

[138] J. Sacks, W.J. Welch, T.J. Mitchell, and H.P. Wynn. Design and analysis of computer experiments. *Statistical science*, pages 409–423, 1989.

[139] P.J. Schmid and D.S. Henningson. *Stability and transition in shear flows*, volume 142. Springer Science & Business Media, 2012.

[140] A. Segalini, J.H.M. Fransson, and P.H. Alfredsson. An experimental analysis of canopy flows. In *Journal of Physics: Conference Series*, volume 318, page 072018. IOP Publishing, 2011.

[141] A. Segalini, J.H.M. Fransson, and P.H. Alfredsson. Scaling laws in canopy flows: a wind-tunnel analysis. *Boundary-layer meteorology*, 148(2):269–283, 2013.

[142] A. Sharma, G. Gomez-de Segura, and R. Garcia-Mayoral. Linear stability analysis of turbulent flows over dense filament canopies. In 10th *International Symposium on Turbulence and Shear Flow Phenomena*, 2017.

[143] R. Singh, M.M. Bandi, A. Mahadevan, and S. Mandre. Linear stability analysis for monami in a submerged seagrass bed. *Journal of Fluid Mechanics*, 786, 2016.

[144] R. Sivanesapillai, H. Steeb, and A. Hartmaier. Transition of effective hydraulic properties from low to high reynolds number flow in porous media. *Geophysical Research Letters*, 41(14):4920–4928, 2014.

[145] E. Skjetne and J.L. Auriault. New insights on steady, non-linear flow in porous media. *European Journal of Mechanics-B/Fluids*, 18(1):131–145, 1999.

[146] N. Slegers, M. Heilman, J. Cranford, A. Lang, J. Yoder, and M.L. Habegger. Beneficial aerodynamic effect of wing scales on the climbing flight of butterflies. *Bioinspiration & Biomimetics*, 12(1):016013, 2017.

[147] C. Soulaine and M. Quintard. On the use of a Darcy–Forchheimer like model for a macro-scale description of turbulence in porous media and its application to structured packings. *International Journal of Heat and Mass Transfer*, 74:88–100, 2014.

[148] R.B. Srygley and A.L.R. Thomas. Unconventional lift-generating mechanisms in free-flying butterflies. *Nature*, 420(6916):660, 2002.

[149] E. Stratakis, V. Zorba, M. Barberoglou, E. Spanakis, S. Rhizopoulou, P. Tzanetakis, S. Anastasiadis, and C. Fotakis. Laser structuring of water-repellent biomimetic surfaces. *SPIE Newsroom*, 10(2.1200901):1441, 2009.

[150] L. Temmerman and M.A. Leschziner. Large eddy simulation of separated flow in a streamwise periodic channel constriction. Begel House Inc., 2001.

[151] N. Tilton and L. Cortelezzi. Linear stability analysis of pressure-driven flows in channels with porous walls. *Journal of Fluid Mechanics*, 604:411–445, 2008.

[152] C. Tropea and H. Bleckmann. *Nature-Inspired Fluid Mechanics: Results of the DFG Priority Programme 1207" Nature-inspired Fluid Mechanics" 2006-2012*, volume 119. Springer Science & Business Media, 2012.

[153] F.J. Valdés-Parada, C.G. Aguilar-Madera, J.A. Ochoa-Tapia, and B. Goyeau. Velocity and stress jump conditions between a porous medium and a fluid. *Advances in water resources*, 62:327–339, 2013.

[154] F.J. Valdés-Parada, D. Lasseux, and F. Bellet. A new formulation of the dispersion tensor in homogeneous porous media. *Advances in Water Resources*, 90:70–82, 2016.

[155] D. Venkataraman and A. Bottaro. Numerical modeling of flow control on a symmetric aerofoil via a porous, compliant coating. *Physics of Fluids*, 24(9):093601, 2012.

[156] G.G. Wang and S. Shan. Review of metamodeling techniques in support of engineering design optimization. *Journal of Mechanical design*, 129(4):370–380, 2007.

[157] H.G. Weller, G. Tabor, H. Jasak, and C. Fureby. A tensorial approach to computational continuum mechanics using object-oriented techniques. *Computers in Physics*, 12(6):620–631, 1998.

[158] S. Whitaker. The transport equations for multi-phase systems. *Chemical Engineering Science*, 28(1):139–147, 1973.

[159] S. Whitaker. Flow in porous media i: A theoretical derivation of darcy's law. *Transport in porous media*, 1(1):3–25, 1986.

[160] S. Whitaker. Flow in porous media iii: deformable media. *Transport in Porous Media*, 1(2):127–154, 1986.

[161] S. Whitaker. The Forchheimer equation: a theoretical development. *Transport in Porous Media*, 25(1):27–61, 1996.

[162] S. Whitaker. *The Method of Volume Averaging*, volume 13. Springer Science & Business Media, 2013.

[163] B.D. Wood and F.J. Valdés-Parada. Volume averaging: Local and nonlocal closures using a green's function approach. *Advances in water resources*, 51:139–167, 2013.

[164] K. Yazdchi and S. Luding. Towards unified drag laws for inertial flow through fibrous materials. *Chemical engineering journal*, 207:35–48, 2012.

[165] K. Yazdchi, S. Srivastava, and S. Luding. Microstructural effects on the permeability of periodic fibrous porous media. *International Journal of Multiphase Flow*, 37(8): 956–966, 2011.

[166] P. Yih-Ferng, S. Yuo-Hsien, and H. Robert. Transition in a 2-d lid-driven cavity flow. *Computers & Fluids*, 32(1):337–352, 2003.

[167] G.A. Zampogna and A. Bottaro. Fluid flow over and through a regular bundle of rigid fibres. *Journal of Fluid Mechanics*, 792:5–35, 2016.

[168] G.A. Zampogna and A. Bottaro. private communication. *The values of $\mathcal{K}_{11}$ and $\mathcal{K}_{22}$ arise from the solution of a local, microscopic problem which accounts for inertia through the porous medium [167]. It is not unexpected that $\mathcal{K}_{11}$ approaches $\mathcal{K}_{22}$ as we leave the Stokes regime.*, 2016.

[169] G.A. Zampogna and A. Bottaro. The pelskin project—part iii: a homogenized model of flows over and through dense poroelastic media. *Meccanica*, 52(8):1797–1808, 2017.

[170] G.A. Zampogna, F. Pluvinage, A. Kourta, and A. Bottaro. Instability of canopy flows. *Water Resources Research*, 52(7):5421–5432, 2016.

[171] G.A. Zampogna, J. Magnaudet, and A. Bottaro. Generalized slip condition over rough surfaces. *Journal of Fluid Mechanics*, submitted.

[172] X. Zhang and H. Nepf. Exchange flow between open water and floating vegetation. *Environmental Fluid Mechanics*, 11(5):531–546, 2011.

[173] T. Zhu, C. Waluga, B. Wohlmuth, and M. Manhart. A study of the time constant in unsteady porous media flow using direct numerical simulation. *Transport in Porous Media*, 104(1):161–179, 2014.